UNIVERSITY OF WEST BOHEMIA

FACULTY OF APPLIED SCIENCES

Reactive High-Power Impulse Magnetron Sputtering of Oxides and Oxynitrides Thin Films

Ing. Alexandr Belosludtsev

A thesis submitted for the degree of Doctor of Philosophy

in the field of Plasma Physics and Physics of Thin Films

Supervisor: prof. RNDr. Jaroslav Vlček, CSc.

Department of Physics

Pilsen 2017

ZÁPADOČESKÁ UNIVERZITA V PLZNI

FAKULTA APLIKOVANÝCH VĚD

Výsokovýkonové pulzní reaktivní magnetronové naprašování oxidových a oxynitridových vrstev

Ing. Alexandr Belosludtsev

Disertační práce

k získání akademického titulu doktor

v oboru Fyzika plazmatu a tenkých vrstev

Školitel: prof. RNDr. Jaroslav Vlček, CSc.

Katedra fyziky

Plzeň 2017

Preface

I submit this Ph.D. thesis, worked out at the Faculty of Applied Sciences, University of West Bohemia, for criticism and defense. I hereby certify that for writting the thesis I was using duly cited literature and scientific articles published or submitted for publication during my Ph.D. studies. The thesis is submitted in a form of five scientific publications.

The thesis includes the results obtained during my Ph.D. study at the Department of Physics and NTIS, European Centre of Excellence, University of West Bohemia, since September 2012. This research was financially supported by the projects SGS–2010–070 (2010–2012): Advanced thin-film materials and new plasma sources, SGS–2013–045 (2013–2015): New thin-film materials and plasma deposition systems, and SGS–2016–056 (2016-2018): New nanostructured thin-film materials formed by plasma technologies.

Pilsen 18. 12. 2016 …………………… Ing. Alexandr Belosludtsev

Acknowledgments

There are many people whom I would like to thank at this point. I wish to start with Prof. Jaroslav Vlček, who as the head of the Department of Physics at the University of West Bohemia, has given me the opportunity to study the doctoral program «Plasma Physics and Physics of Thin Film». Moreover, I would like to express my sincere gratitude to him as my supervisor for guidance, never-ending optimism, valuable comments and scientific advice. I would like to thank Assoc. Profs. Pavel Baroch and Petr Zeman. Many thanks go to people who are providing technical support in laboratories. I am very grateful to all my colleagues who created an inspiring and friendly environment. It was great to have with you intresting discussions of various subject matters related not just to our scientific work. Particular thanks for valuable discussions go to all great people I have met at the conferences. Special thanks belong to the people who collaborated with me on particular research projects and whose names are mentioned at the beginning of the corresponding parts in Chapter II. Additionally, I would like to thank Dr. Nikolay Britun for kindness, sharing expertise and guidance during my summer traineeship at the University of Mons in August 2016. Unfortunately, the traineeship was close to the defence and therefore the results are not included here.

There are special people whose support and encouragement was worth more than I can express on paper. I wish to express warmest gratitude to my mother, cousin and aunt who believed in me and wanted the best for me. It is necessary to underline great and deep gratitude to my wife Diana for her patience, love and always being there for me. She was encouraging me in my pursuits and inspiring me to follow the dreams.

CONTENTS

I. General introduction 6

II. Aims of the thesis 8

III. Results 9

A. High-rate reactive high-power impulse magnetron sputtering of hard and optically transparent HfO_2 films 10

1. Introduction 11
2. Experimental details
   2.1. Film preparation 12
   2.2. Film characterization 13
3. Results and discussion
   3.1. Discharge and deposition characteristics 14
   3.2. Structure and properties of films 16
4. Conclusions 17
5. References 17

B. Microstructure of hard and optically transparent HfO_2 films prepared by high-power impulse magnetron sputtering with a pulsed oxygen flow control 18

1. Introduction 19
2. Experimental details
   2.1. Film preparation 20
   2.2. Film characterization 20
3. Results and discussion
   3.1. AFM studies 21
   3.2. XRD studies 21
   3.3. HRTEM investigation
      3.4.1. Films T200S54 and T200S18 22
      3.4.2. Films T200S7 and T100S7 23
   3.4 Effect of deposition parameters on the HfO_2 film microstructure and properties 27
4. Conclusions 28
5. References 28

C. Thickness dependent wetting properties and surface free energy of HfO_2 thin films 30

Letter text 31

D. Structure and properties of Hf-O-N films prepared by high-rate reactive HiPIMS with smoothly controlled composition 36

1. Introduction 37
2. Experimental details
   2.1. Hf-O-N preparation 38
   2.2. Hf-O-N characterization 39
3. Results and discussion
   3.1. Elemental composition and deposition rate 41
   3.2. Hf-O-N structure 42
   3.3. Hf-O-N properties 45
4. Conclusions 49
5. References 49

E. Reactive high-power impulse magnetron sputtering of ZrO_2 films with gradient ZrO_x interlayers on pretreated steel substrates 52

1. Introduction 53
2. Experimental details
   2.1. Coating preparation 54
   2.2. Coating characterization 57
3. Results and discussion
   3.1. Discharge characteristics 60
   3.2. Coating structure and properties 62
4. Conclusions 66
5. References 66

IV. Conclusions of the thesis 68

V. Further publications of the candidate 70

1. Papers in international journals 70
2. Oral and poster presentations at international conferences 70

I. General introduction

Thin-film materials are the fundament of many modern technologies. They can improve mechanical, chemical, optical, electrical and hydrophobic properties of underlying materials. Moreover, some of thin film properties can arise in the nanoscale range.

Preparation of new materials requires application of new approaches and methods. Plasma technologies have already proved their potencial in preparation of various functional materials. Magnetron sputtering, since appearance in 1960′s [1], has brought the essential advantages to the thin film science and technology. This technique is based on the generation of a low pressure magnetically enhanced glow discharge – magnetron discharge. An inert gas (usually Ar) is used as a working gas. The electrical discharge is generated by applying an electrical voltage between a cathode and anode. The walls of the deposition chamber usually serve as the anode. Important advantages of magnetron sputter deposition are that almost any metallic target material can be sputtered and that very smooth coatings (without droplets) with various functional properties can be prepared.

Nowadays, direct current (DC) magnetron sputtering is successfully used for thin film depositions. In DC magnetron sputtering, applied power is limited (Wcm^{-2} or less) by the thermal load of the target and does not allow for generation of high density plasma. Neutral depositing species are the major flux onto substrate.

High-power impulse magnetron sputtering (HiPIMS) is a relatively new technology. First papers on this technique were published by Russian research groups in 1990′s [2,3]. The HiPIMS technique utilises extremely high power densities of the order of $kWcm^{-2}$ in short impulses of tens of microseconds at low duty cycle (ussually less than 10 %) to avoid thermal load of the target. The high target power density leads to generation of very dense discharge plasma with high degree of ionization of sputtered atoms. HiPIMS is establishing itself in fields where conventional methods fails.

In spite of several successful applications of the HiPIMS systems to reactive sputter depositions of dielectric films, there are still substantial problems with arcing on target surfaces during the reactive deposition processes at high target power densities, particularly for voltage pulses longer than 40 μs, and with low deposition rates achieved.

To avoid these problems, a feed-back pulsed reactive gas flow control (RGFC) was proposed by team of Prof. Jaroslav Vlček from the Department of Physics at the University of West Bohemia in the frame of collaboration with the TRUMPF Hüttinger Company [4]. In recent papers, they reported on high-rate reactive depositions of densified, highly optically transparent, stoichiometric ZrO_2 and Ta_2O_5 films [5] and Ta-O-N films with tunable composition and properties [6]. It was shown that placing the reactive gas inlet into the most intense zone of a HiPIMS discharge leads to a high degree of dissociation of both O_2 and N_2, and consequently to a replacement of the aforementioned different reactivities of O_2 and N_2 by similar (high) reactivities of atomic O and N. In parallel, this feed-back process control is able to maintain a reactive

sputter deposition of films in the region between a more and less metallic mode, and to utilize the following exclusive benefits of the HiPIMS discharges in preparation of films: (i) intense sputtering of atoms from the target resulting in a substantially increased deposition rate, (ii) a strong "sputtering wind" of the sputtered atoms resulting in a reduced flux of the RG particles onto the target and their enlarged flux onto the substrate, and (iii) highly ionized fluxes of particles with enlarged fractions of ionized sputtered metal atoms onto the substrate and enhanced energies of the ions bombarding the growing films resulting in their structural changes and densification without a substrate bias. The advantage of the proposed pulsed RGFC method is that it does not require any additional measurement or monitoring devices, such as a plasma emission monitoring system, mass spectrometer or Lambda sensor, and that it is applicable to all magnetron sputtering discharges.

The Ph.D. thesis deals with preparation and characterization of multifunctional HfO_2 and Hf-O-N films, and ZrO_2 films with gradient ZrO_x interlayers. They were deposited using reactive high-power impulse magnetron sputtering with a pulsed reactive gas flow control onto floating substrates at low substrate temperatures (no external heating).

[1] W. D. Gill, E. Kay, Efficient low pressure sputtering in a large inverted magnetron suitable for film synthesis, Rev. Sci. Instrum. 36 (1965) 277–282.

[2] D. V. Mozgrin, I. K. Fetisov, G. V. Khodachenko, High-Current Low-Pressure Quasistationary Discharge in a Magnetic Field: Experimental Research, Plasma Phys. Rep. 51(1995) 400–409.

[3] I. K. Fetisov, A. A. Filippov, G. V. Khodachenko, D.V. Mozgrin, A. A. Pisarev, Impulse irradiation plasma technology for film deposition, Vacuum 53 (1999) 133–136.

[4] R. Bugyi, J. Vlček, J. Rezek, J. Lazar, High-rate reactive sputtering of dielectric stoichiometric films, European patent EP 2 770 083 B1, date of publication: 18.11.2015.

[5] J. Vlček, J. Rezek, J. Houška, R. Čerstvý, R. Bugyi, Process stabilization and a significant enhancement of the deposition rate in reactive high-power impulse magnetron sputtering of ZrO_2 and Ta_2O_5 films, Surf. Coat. Technol. 236 (2013) 550–556.

[6] J. Rezek, J. Vlček, J. Houška, R. Čerstvý, High-rate reactive high-power impulse magnetron sputtering of Ta-O-N films with tunable composition and properties, Thin Solid Films 566 (2014) 70–77.

II. Aims of the thesis

This Ph.D. thesis deals with preparation and characterization of multifunctional oxide and oxynitride films. They were deposited using reactive high-power impulse magnetron sputtering with a pulsed reactive gas flow control onto floating substrates at low substrate temperatures (no external heating). Particular aims of the thesis were formulated as follows:

A. To use reactive HiPIMS with a pulsed RGFC for high-rate depositions of hard, densified, highly optically transparent, stoichiometric HfO_2 films. To investigate the effect of the deposition-averaged target power density and the voltage pulse duration on discharge behavior, deposition characteristics and film properties. To propose an explanation of high values of the deposition rate of films.

B. To investigate the effect of the deposition-averaged target power density and the voltage pulse duration on the microstructure, and mechanical and optical properties of the HfO_2 films.

C. To master the deposition of hard and optically transparent, stoichiometric HfO_2 films with a very accurate pre-selected thickness ranged from 50 nm to 2500 nm. To explain the effect of the film thickness on wetting properties and surface free energy of HfO_2 thin films.

D. To master a high-rate deposition of Hf-O-N films with tunable composition and properties. To investigate the relationships between the elemental composition of films and their phase structure, and optical, electrical, mechanical and hydrophobic properties.

E. To propose a simple (no substrate bias voltage during reactive sputter depositions and no external heating during the whole process) HiPIMS technique for a fast deposition of densified stoichiometric ZrO_2 films with enhanced adhesion to steel substrates.

III. Results

The thesis is submitted in a form of five scientific papers published (A-C) or submitted for publication (D, E) in prestigious international journals. These papers include the most important results obtained during my Ph.D. study at the Faculty of Applied Science, University of West Bohemia in Pilsen since September 2012.

I carried out all depositions of the HfO_2 (A-C) and Hf-O-N (D) films and of the ZrO_2 films with gradient ZrO_x interlayers (E) presented, together with all discharge and deposition characteristics and the corresponding measurements of the film thickness and mechanical, electrical and hydrophobic properties of the films (A-E). In addition, I actively participated in interpretation of the results obtained for the elemental composition, phase composition, surface free energy and optical properties of the films by my colleagues (A, C-E) and for microstructure of the HfO_2 flims by our collaborators at the University of Texas at Arlington (B). I wrote the first versions of the papers A, D and E, and I actively participated in writing the papers B and C.

A. High-rate reactive high-power impulse magnetron sputtering of hard and optically transparent HfO_2 films

J. Vlček, A. Belosludtsev, J. Rezek , J. Houška, J. Čapek, R. Čerstvý, S. Haviar

Surf. Coat. Technol. 290 (2016) 58–64

Selected paper from the Society of Vacuum Coaters
58th Annual Technical Conference, Santa Clara, USA, 2015

Surface & Coatings Technology 290 (2016) 58–64

Contents lists available at ScienceDirect

Surface & Coatings Technology

journal homepage: www.elsevier.com/locate/surfcoat

High-rate reactive high-power impulse magnetron sputtering of hard and optically transparent HfO_2 films

J. Vlček, A. Belosludtsev, J. Rezek *, J. Houška, J. Čapek, R. Čerstvý, S. Haviar

Department of Physics and NTIS, European Centre of Excellence, University of West Bohemia, Univerzitní 8, 306 14 Plzeň, Czech Republic

ARTICLE INFO

Article history:
Received 15 June 2015
Revised 10 August 2015
Accepted in revised form 12 August 2015
Available online 15 August 2015

Keywords:
Nanocrystalline HfO_2 films
High optical transparency
Near ultraviolet region
High deposition rates
Controlled reactive HiPIMS

ABSTRACT

High-power impulse magnetron sputtering (HiPIMS) with a pulsed reactive gas (oxygen) flow control was used for high-rate reactive depositions of densified, highly optically transparent, stoichiometric HfO_2 films onto floating substrates. The depositions were performed using a strongly unbalanced magnetron with a directly water-cooled planar Hf target of 100 mm diameter in argon–oxygen gas mixtures at the argon pressure of 2 Pa. The repetition frequency was 500 Hz at the deposition-averaged target power density from 29 W cm^{-2} to 54 W cm^{-2}. The voltage pulse durations ranged from 50 μs to 200 μs. The target-to-substrate distance was 100 mm and the substrate temperatures were less than 165 °C. We showed that the HfO_2 films can be prepared with very high deposition rates (up to 200 nm/min) at a deposition-averaged target power density of approximately 30 W cm^{-2}, which is relatively close to a target power density applicable in industrial HiPIMS systems. The films were nanocrystalline with a dominant monoclinic phase. They exhibited a hardness of 15–18 GPa, a refractive index of 2.07–2.12 and an extinction coefficient between ≤0.1×10^{-3} and 0.6×10^{-3} (both quantities at the wavelength of 550 nm). At 300 nm, the extinction coefficient was between 1.5×10^{-3} and 7.0×10^{-3}. A simplified relation for the deposition rate of films prepared using a reactive HiPIMS was presented.

© 2015 Elsevier B.V. All rights reserved.

1. Introduction

Hafnium dioxide (HfO_2) is an important optical coating material with a high refractive index and a broad region of low absorption from the near-UV (about 250 nm) to the mid-IR (beyond 12 μm). Various optical applications of HfO_2 films have been pursued such as visible, near-IR and mid-IR antireflection coatings [1–3], chirped mirrors and band pass filters [4], UV mirrors with a high damage threshold [5], and heat mirrors for energy-efficient windows [6]. Having a high dielectric constant (around 25) and being thermodynamically stable when grown on Si, HfO_2 is considered to be one of the most promising candidates to replace SiO_2 in gated electronic devices [7]. Moreover, because of its high melting point (around 2800 °C) and excellent thermal stability [8], HfO_2-based materials have been explored as thermal barrier coatings for turbine blades operating in harsh and high-temperature environments [9,10]. HfO_2 and HfO_2-based materials are traditionally regarded as a class of valuable materials in nuclear industries, as they have an exceptionally high neutron absorption coefficient [8]. Recently, hydrophobic properties of HfO_2 coatings have been reported [11].

Reactive dc magnetron sputtering is a suitable method to deposit HfO_2 films [4,11–15]; however, an active feed-back process control is needed to produce high-quality films with a high deposition rate [16]. Various pulsed magnetron sputtering techniques and methods to control the processes have been proposed to avoid problems with arcing on target surfaces during reactive sputter depositions of dielectric films and with low deposition rates achieved [17–19].

In our recent paper [20], we reported on high-rate reactive depositions of densified, highly optically transparent, stoichiometric ZrO_2 and Ta_2O_5 films using high-power impulse magnetron sputtering (HiPIMS) with a pulsed reactive gas flow control (RGFC). This feedback process control is able to maintain a sputter deposition of stoichiometric films in the region between a more and less metallic mode, and to utilize the following exclusive benefits of the HiPIMS discharges in preparation of films [21]: (i) intense sputtering of atoms from the target resulting in a substantially increased deposition rate, (ii) very high degrees of dissociation of RG molecules in the flux onto the substrate resulting in a higher incorporation of RG atoms into materials, (iii) a strong "sputtering wind" of the sputtered atoms resulting in a reduced flux of the RG particles onto the target and their enlarged flux onto the substrate, and (iv) highly ionized fluxes of particles with enlarged fractions of ionized sputtered metal atoms onto the substrate and enhanced energies of the ions bombarding the growing films resulting in their structural changes and densification without a substrate bias. The advantage of the proposed pulsed RGFC method is that it does not require any additional measurement or monitoring devices, such as a plasma emission monitoring system, mass spectrometer or Lambda sensor [17,19], and that it is applicable to all magnetron sputtering discharges.

* Corresponding author.
E-mail address: jrezek@ntiszcu.cz (J. Rezek).

http://dx.doi.org/10.1016/j.surfcoat.2015.08.024
0257-8972/© 2015 Elsevier B.V. All rights reserved.

In the present paper, we report on high-rate reactive depositions of densified, highly optically transparent, stoichiometric HfO_2 films using HiPIMS with the pulsed RGFC. The main aim of this study is to show that hard HfO_2 films, exhibiting a high optical transparency also in the near-UV region (at 300 nm in our work), can be prepared with very high deposition rates (up to 200 nm/min for the target-to-substrate distance of 100 mm) at a deposition-averaged target power density of approximately 30 W cm^{-2}, which is relatively close to a target power density applicable in industrial HiPIMS systems.

2. Experimental details

2.1. Film preparation

The films were deposited using a strongly unbalanced magnetron source with a directly water-cooled planar hafnium target (99.9% Hf purity, diameter of 100 mm and thickness of 6 mm) in a standard stainless-steel vacuum chamber (diameter of 507 mm and length of 520 mm), which was evacuated by a diffusion pump (2 $m^3 s^{-1}$) backed up with a rotary pump (30 $m^3 h^{-1}$). The base pressure before deposition was 10^{-3} Pa. A detailed characterization of the magnetic field and the degree of its unbalance is given in Ref. [22]. The water cooling of the target, keeping its surface temperature under 350 °C during the depositions, is described in Ref. [20].

The magnetron was driven by a high-power pulsed dc power supply (HMP 2/1, Hüttinger Elektronik). In this work, the repetition frequency, f_r, was 500 Hz and the voltage pulse duration, t_1, ranged from 50 to 200 μs with the corresponding duty cycle $t_1/T = 2.5\%–10\%$, where the pulse period $T = 1/f_r$.

A reactive gas (oxygen) was admitted into the vacuum chamber from a source via mass flow controllers and two corundum conduits (Fig. 1). Two O_2 inlets with a diameter of 1 mm were placed symmetrically above the target racetrack at the same distance of 20 mm from the target surface and oriented to the substrate. Such an inlet configuration is a result of optimization based on our extensive experiments [21].

Prior to the admission of O_2 into the system, the Ar flow rate was set to 30 sccm and the pumping speed of the diffusion pump was adjusted to attain the argon partial pressure, p_{ar}, at the same value of 2 Pa for all the depositions. The settings of the Ar flow rate and the pumping speed were not changed during the experiments. The values of p_{ar} and of $p_{ar} + p_{ox}$, where p_{ox} is the partial pressure of oxygen in the chamber, were measured using a high-stability capacitance manometer (Baratron, type 627, MKS Instruments) with the accuracy of approximately 1%.

Waveforms of the magnetron voltage, $U_d(t)$, and the discharge current, $I_d(t)$, were monitored [21] and our own software evaluated the time-varying average target power density in a discharge pulse, S_{da}, given by

$$S_{da} = \frac{1}{t_1}\int_0^{t_1} U_d(t)J_t(t)dt. \quad (1)$$

Here, the target current density $J_t(t) = I_d(t) / A_t$, where A_t is the total area of the target (78.54 cm^2 in our case). The deposition-averaged target power density, $\langle S_d \rangle$, was evaluated with the use of the formula

$$\langle S_d \rangle = \frac{1}{t_e - t_s}\int_{t_s}^{t_e} U_d(t)J_t(t)dt, \quad (2)$$

where t_s and t_e are the start and end times of the deposition. An analogous integral expression was used to calculate the deposition-averaged oxygen flow rate, $\langle \Phi_{ox} \rangle$, from the monitored dependences of $\Phi_{ox}(t)$, which is the instantaneous total oxygen flow rate into the vacuum chamber. During the deposition, $\Phi_{ox}(t)$ = const or 0, see the dashed line in Fig. 2. The time-varying average discharge current in a period of the power supply,$\bar{I}_d$, was evaluated using the formula

$$\bar{I}_d = \frac{1}{T}\int_0^T I_d(t)dt. \quad (3)$$

Prior to a given deposition, we fix the nominal target power at an essentially constant magnetron voltage during discharge pulses, a preset argon partial pressure, total oxygen flow rates in both conduits, the O_2 inlet configuration, and a pre-selected critical value (Fig. 2) of the partial pressure of oxygen in the chamber, $p_{ox}(t)$, which was chosen to be the control process parameter in this work [20]. During the deposition, a process controller used then provides a control feed-back signal to the two O_2 mass flow controllers to adjust the pulsed O_2 flow rate into the vacuum chamber by adjusting the duration of the O_2 flow rate pulses by means of the pre-selected critical value of $p_{ox}(t)$, which is monitored by the process controller.

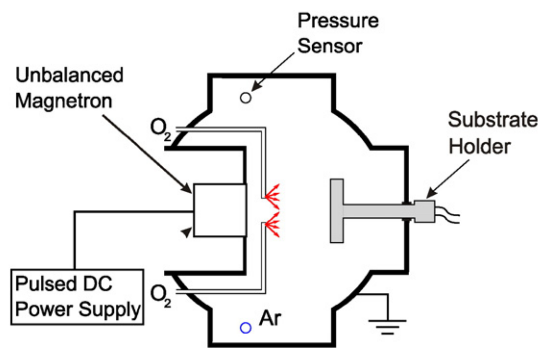

Fig. 1. Schematic diagram of the deposition device with two O_2 inlets in front of the target (20 mm from the target surface). Positions of the pressure sensor and the Ar inlet in the back side of the vacuum chamber are also shown.

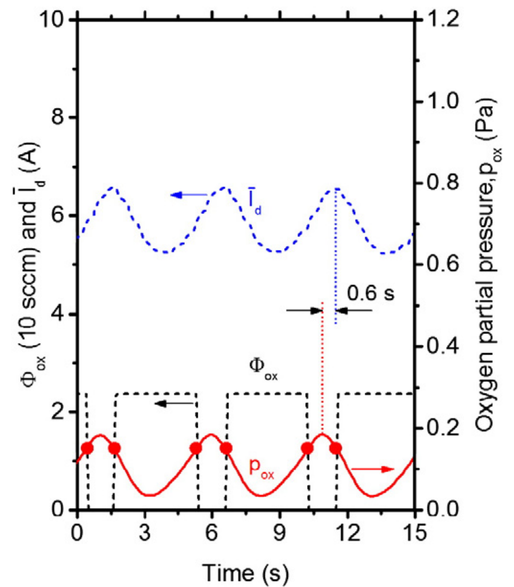

Fig. 2. Time evolution of the average discharge current in a period of the power supply, $\bar{I}_d(t)$, oxygen partial pressure, p_{ox}, and the corresponding oxygen flow rate pulses, Φ_{ox}, during a controlled reactive sputter deposition of the stoichiometric HfO_2 film at $\langle S_d \rangle$ = 54 W cm^{-2} and t_1 = 200 μs (Table 1). A pre-selected critical value of p_{ox} = 0.15 Pa determining the switching-on and switching-off of the oxygen flow rate Φ_{ox} = 23.8 sccm is marked by dots.

In the present experiments, we used the preset deposition-averaged target power densities $<S_d> = 29–54$ W cm^{-2} for depositions of HfO_2 films, and $<S_d> = 28$ W cm^{-2} and 49 W cm^{-2} for reference depositions of Hf films at a fixed argon partial pressure $p_{ar} = 2$ Pa (Table 1). For depositions of the HfO_2 films, we applied constant values of the total oxygen flow rate $\Phi_{ox} = 12$, 12, 14 and 16 sccm in an oxygen flow pulse at $t_1 = 50$, 100, 150 and 200 μs, respectively, and $<S_d> = 29–33$ W cm^{-2} (Table 1), and $\Phi_{ox} = 23.8$ sccm at $t_1 = 200$ μs and $<S_d> = 54$ W cm^{-2} (Table 1 and Fig. 2). The values of $\Phi_{ox}(t)$ were measured with the accuracy of approximately 1%.

A basic principle of the pulsed RGFC is illustrated in Fig. 2. As can be seen, a pre-selected critical value of $p_{ox} = 0.15$ Pa determines the switching-on and switching-off of the oxygen flow at the rate $\Phi_{ox} = 23.8$ sccm used in a controlled reactive sputter deposition of the stoichiometric HfO_2 film at $<S_d> = 54$ W cm^{-2} and $t_1 = 200$ μs. Under these conditions, the amount of oxygen injected into the discharge is sufficiently low to minimize arcing on the compound part of the metal target and to avoid a substantial reduction in the deposition rate of films, but it is sufficiently high to achieve a sufficient incorporation of the oxygen atoms into the films (stoichiometric HfO_2 composition). A detailed description of the control loop is given in Ref. [20]. In contrast with depositions of ZrO_2 films, for which we used $\bar{I}_d(t)$ as a control process parameter [20,21], the control process parameter for depositions of HfO_2 films is $p_{ox}(t)$. The main reason is a too fast decrease of $p_{ox}(t)$ from its maximum value down to $p_{ox}(t) \approx 0$ due to a delayed switching-on (by 0.6 s as shown in Fig. 2) of Φ_{ox} pulses, leading to problems with a film stoichiometry, should we use $\bar{I}_d(t)$ as a control process parameter. Let us recall different affinities of target materials (Hf or Zr) for chemical reactions with oxygen (a standard molar Gibbs energy is −1088 kJ/mol for HfO_2 and −1042 kJ/mol for ZrO_2 [23]) and their different sputtering yields (1.21 and 0.89 for Hf sputtered by 600 eV Ar^+ and Hf^+ ions, respectively, and 0.93 and 0.65 for Zr sputtered by 600 eV Ar^+ and Zr^+ ions, respectively [24]).

An additional grounded ring-shaped anode, which was periodically cleaned, was mounted into the system around the insulated substrate holder to suppress the "disappearing anode" effect [19].

The HfO_2 and Hf films were deposited onto silicon substrates at a floating potential. The target-to-substrate distance, d, was 100 mm. The substrate temperature, T_s, reached during depositions without an external heater, was in the range from 140 to 165 °C for the HfO_2 films, and 135 and 155 °C for the Hf films (Table 1).

2.2. Film characterization

The film thickness (between 1000 and 1400 nm) was measured at the film edge by profilometry (Dektak 8 Stylus Profiler, Veeco) using a 380 μm thick removable Si step, and at various places of the film by ellipsometry. The maximum measurement error of both of these techniques was well below 1%. The corresponding deposition rate, a_D, was determined as the ratio of the film thickness at the center of the film edge, where the two aforementioned techniques provide almost identical results, to the deposition time. The position of the film edge at the substrate holder was the same in all the depositions with the center of the film edge 10 mm from the axis. The same profilometer was used to measure bending of the substrate after deposition of the film, from which the residual macrostress was determined using the original Stoney's formula (see, for example, Ref. [25]).

The elemental composition of the films was investigated by means of the energy dispersive spectroscopy (EDS) carried out in a scanning electron microscope (SU-70, Hitachi) equipped with EDS detector (UltraDry, Thermo Scientific) using a primary electron energy of 5 keV. The EDS was used for a comparison of the films. The precise value of the Hf:O ratio was determined by the X-ray photoelectron spectroscopy (XPS) using MgKα X-ray source and five-channel hemispherical analyzer (EA 125, Omicron) tuned to a pass energy of 20 eV. In order to eliminate the influence of the surface oxidized layer, films were treated by Ar^+ bombardment (25 min, 1.5 μA, 1 kV, 30°).

X-ray diffraction (XRD) measurements were carried out at room temperature on a PANalytical X'Pert PRO diffractometer working in the Bragg–Brentano geometry using a CuKα (40 kV, 40 mA) radiation. To avoid a strong reflection from the Si (100) substrate, a slightly asymmetrical diffraction geometry with an ω-offset of 1.5° was used. Samples were scanned over the 2θ-range from 8° to 108°.

The refractive index, n, and extinction coefficient, k, were determined by variable angle spectroscopic ellipsometry (VASE) using the J.A. Woollam Co. Inc. instrument. The measurements were performed using angles of incidence of 65°, 70° and 75° in reflection. The optical data were fitted using the WVASE software and an optical model consisting of a c-Si substrate, a HfO_2 layer described by the Cauchy dispersion formula with an Urbach absorption tail and a surface roughness layer. Below we (i) show the dispersion curves of n and k in the 300–1500 nm range and (ii) discuss n and k values at specific wavelengths given in the subscript, e.g. n_{550} and k_{550} for 550 nm. Precision of the lowest k values has been ensured by measuring and fitting the data in an even wider range of 250–2000 nm (approaching the band gap edge of HfO_2 at approximately 5.5 eV corresponding to 225 nm), which includes a larger part of the Urbach tail.

The film hardness, H, and the effective Young's modulus, $E^* = E/(1 - \upsilon^2)$, where E and υ are the Young's modulus and the Poisson's ratio, respectively, were determined using an ultramicroindenter (Fischerscope H-100B) according to the ISO 14577–1:2002 E standard. The measurements were performed with a preset maximum load of 20 mN. The relative measurement errors, determined from 25 measurements at different places of 20 × 20 mm^2 samples, are 6% and 4% for the H and E^* values, respectively.

Table 1
Process parameters and material characteristics of stoichiometric HfO_2 films at preset deposition-averaged target power densities, $<S_d>$, from 29 to 54 W cm^{-2}, voltage pulse durations, t_1, from 50 to 200 μs, and a fixed argon partial pressure $p_{ar} = 2$ Pa. The oxygen partial pressures, p_{ox}, were between 0.01 and 0.19 Pa. Here, S_{da} is the average target power density in a discharge pulse, U_{da} is the corresponding average magnetron voltage in a discharge pulse, k_{550} and n_{550} are the extinction coefficient and refractive index of the films at a wavelength of 550 nm, respectively; H, E^* and σ is the hardness, effective Young's modulus and compressive stress of the films, respectively. For comparison, the data obtained for Hf films prepared at $<S_d> = 28$ and 49 W cm^{-2}, and $t_1 = 200$ μs are also given.

Process parameters						Material characteristics				
t_1 (μs)	$<S_d>$ (W cm^{-2})	p_{ox} (Pa)	S_{da} (W cm^{-2})	U_{da} (V)	T_s (°C)	k_{550} (10^{-3})	n_{550}	H (GPa)	E^* (GPa)	σ (GPa)
200	49	0	495	765	<155	–	–	8	150	–
200	28	0	280	610	<135	–	–	10	153	–
200	54	0.03–0.19	490–630	760–740	<155	1	2.11	18	173	1.4
200	33	0.01–0.13	260–400	630–650	<140	0.5	2.12	18	172	1.2
150	29	0.03–0.11	340–400	655–650	<150	0.6	2.12	18	177	1.3
100	30	0.02–0.10	520–660	700–695	<145	≤0.1	2.07	18	173	0.7
50	29	0.01–0.08	1090–1260	895–900	<165	0.5	2.07	15	174	0.5

3. Results and discussion

In the following, we present the results obtained for high-rate reactive depositions of densified stoichiometric HfO_2 films onto floating substrates using HiPIMS with a pulsed RGFC.

All films exhibited the same elemental composition proved by the identical EDS spectra. One sample was measured by XPS and the Hf:O ratio was determined to be 36:64 by fitting the Hf 4d and O 1 s peaks. Considering this and taking into account the estimated accuracy of 1–2 at.%, all films can be considered stoichiometric HfO_2.

First, we show and explain the discharge characteristics during the controlled reactive HiPIMS of films (Fig. 3 and Table 1). Then, we evaluate the fundamental deposition characteristics, namely, the deposition rate of films, a_D (Figs. 4 and 5), the deposition-averaged oxygen flow rate, $<\Phi_{ox}>$, characterizing the consumption of oxygen during a reactive deposition, and the $a_D/<\Phi_{ox}>$ ratio, characterizing the efficiency of the oxygen utilization in a reactive deposition (Fig. 6). Lastly, we present the structure of the HfO_2 films (Fig. 7), and their optical and mechanical properties (Fig. 8 and Table 1).

3.1. Discharge and deposition characteristics

Fig. 3 shows the time evolution of the magnetron voltage, $U_d(t)$, and the target current density, $J_t(t)$, relating to the minimum (dashed lines) and maximum (solid lines) values of the average discharge current in a period of the power supply, $\bar{I}_d(t)$, see Fig. 2, during a reactive sputter deposition of the stoichiometric HfO_2 film at $<S_d> = 54$ W cm^{-2} and $t_1 = 200$ µs. Thus, Fig. 3 shows the range of the waveforms of $U_d(t)$ and $J_t(t)$ during the controlled deposition of the HfO_2 film with the corresponding average target power density in a discharge pulse, S_{da}, being between 490 and 630 W cm^{-2} (Table 1). For comparison, the waveforms of $U_d(t)$ and $J_t(t)$ for a Hf film deposition at $<S_d> =$ 49 W cm^{-2} and $t_1 = 200$ µs are also given. A more rapid decrease in $U_d(t)$ after the negative voltage pulse for the Hf film deposition is a result of a more rapid discharging of the power supply capacitor due to a higher $J_t(t)$ at the moment of the U_d pulse termination ($t = t_1$).

Fig. 4 shows high deposition rates of the stoichiometric HfO_2 films $a_D = 110$–195 nm/min achieved at $<S_d> = 29$–33 W cm^{-2} and even $a_D = 345$ nm/min achieved at $<S_d> = 54$ W cm^{-2}. The values of $a_D = 195$ and 345 nm/min for the HfO_2 films at $t_1 = 200$ µs, and $<S_d> = 33$ and 54 W cm^{-2}, respectively, are relatively close (around 75%) to the respective values of $a_D = 250$ and 460 nm/min achieved for the Hf films at $t_1 = 200$ µs, and $<S_d> = 28$ and 49 W cm^{-2}. In spite of significantly lower $<S_d> = 29$–33 W cm^{-2}, the deposition rates of the HfO_2 films are much higher (1.30–1.63 times) than those (80–120 nm/min) achieved using the same device for densified stoichiometric ZrO_2 films at the same voltage pulse durations and $<S_d> = 51$–53 W cm^{-2} [21]. Here, it should be mentioned that

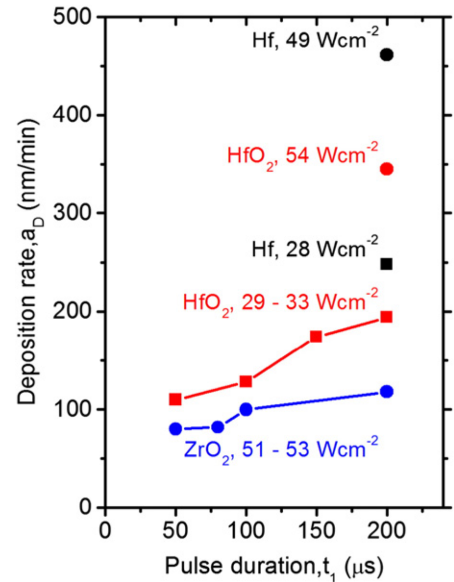

Fig. 4. Deposition rates, a_D, of stoichiometric HfO_2 films at deposition-averaged target power densities $<S_d> = 29$–33 W cm^{-2} and various voltage pulse durations, t_1, ranging from 50 to 200 µs, and at $<S_d> = 54$ W cm^{-2} and $t_1 = 200$ µs (Table 1). For comparison, the deposition rates achieved using the same deposition device for stoichiometric ZrO_2 films at $<S_d> = 51$–53 W cm^{-2} and t_1 from 50 to 200 µs (adapted from Ref. [21]), and for Hf films prepared at $<S_d> = 28$ and 49 W cm^{-2}, and $t_1 = 200$ µs (Table 1) are also presented.

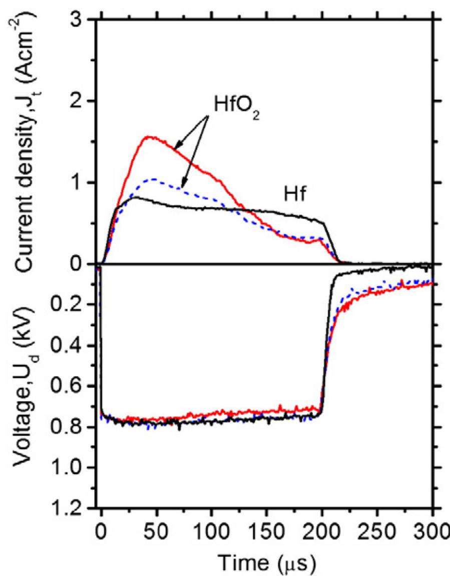

Fig. 3. Waveforms of the magnetron voltage, U_d, and the target current density, J_t, relating to the minimum (dashed lines) and maximum (solid lines) values of the average discharge current in a period of the power supply, $\bar{I}_d(t)$, during a reactive sputter deposition of the stoichiometric HfO_2 film at $<S_d> = 54$ W cm^{-2} and $t_1 = 200$ µs (Fig. 2). For comparison, the waveforms of U_d and J_t for a Hf film deposition at $<S_d> = 49$ W cm^{-2} and $t_1 =$ 200 µs are also shown.

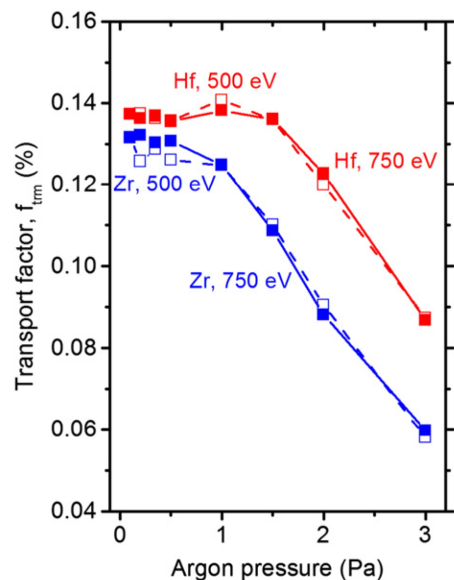

Fig. 5. Transport factors, f_{trm}, calculated for Hf and Zr atoms sputtered from the metal target (diameter of 100 mm) and striking a detector (diameter of 8 mm) at the axis of the substrate (d = 100 mm) in a pure argon gas under various pressures. The incident energy of Ar^+ ions was 500 eV (dashed lines) and 750 eV (solid lines).

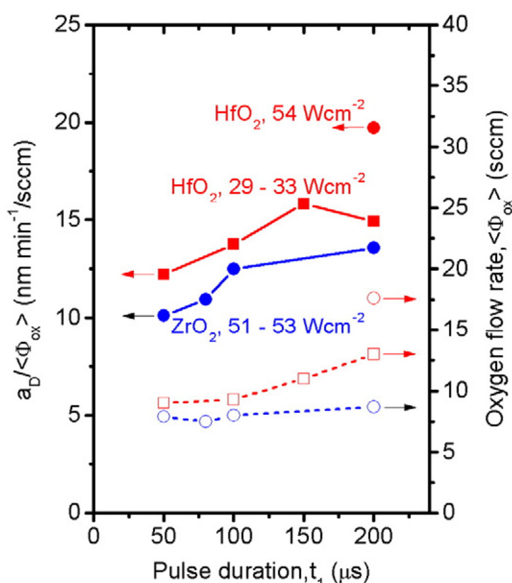

Fig. 6. Deposition-averaged oxygen flow rates, $<\Phi_{ox}>$, and the $a_D/<\Phi_{ox}>$ ratios for stoichiometric HfO_2 films at deposition-averaged target power densities $<S_d> = 29–33\ W\ cm^{-2}$ and various voltage pulse durations, t_1, ranging from 50 to 200 µs (squares), and at $<S_d> = 54\ W\ cm^{-2}$ and $t_1 = 200$ µs (Table 1). For comparison, the corresponding values of $<\Phi_{ox}>$ and $a_D/<\Phi_{ox}>$ obtained using the same deposition device for stoichiometric ZrO_2 films at $<S_d> = 51–53\ W\ cm^{-2}$ and t_1 from 50 to 200 µs (circles, adapted from Ref. [21]) are also presented.

the deposition-averaged target power density of approximately 30 W cm^{-2} is relatively close to a target power density applicable in industrial HiPIMS systems.

To understand the very high deposition rates achieved for the HfO_2 films, we use a simplified relation for the deposition rate assuming that the sputtering of Hf atoms from the metallic fraction of the target is the dominant process determining the deposition rate of the HfO_2

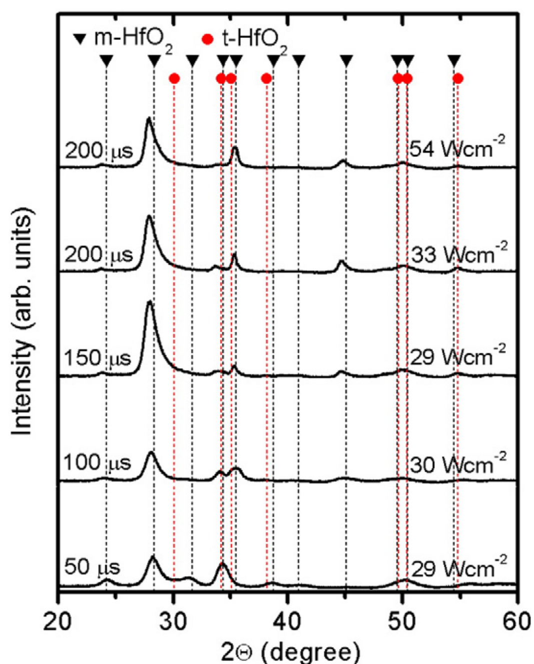

Fig. 7. X-ray diffraction patterns taken from stoichiometric HfO_2 films prepared at deposition-averaged target power densities $<S_d> = 29–54\ W\ cm^{-2}$ and voltage pulse durations, t_1, ranging from 50 to 200 µs (Table 1). The main diffraction peaks of monoclinic (m-HfO_2, Card No. 34-0104 in Ref. [34]) and tetragonal (t-HfO_2, Card No. 8-0342 in Ref. [34]) phase are marked. The m-HfO_2 (−111) diffraction peak is at the position 2Θ = 27.90°.

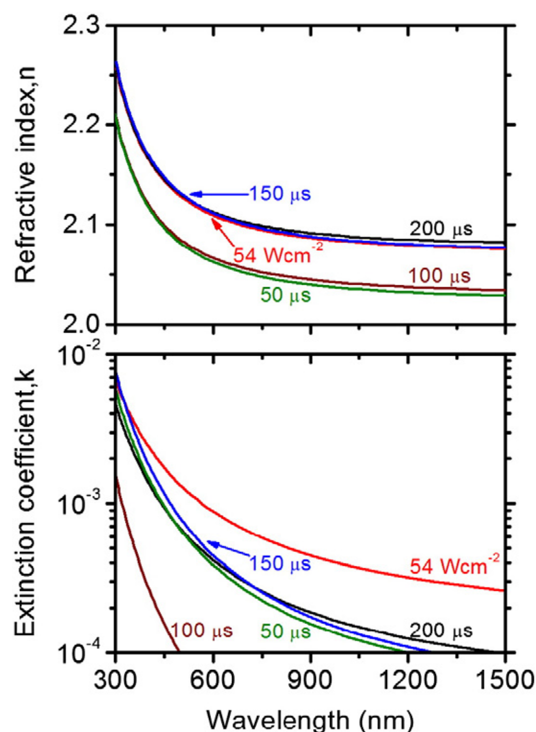

Fig. 8. Refractive index, n, and extinction coefficient, k, (both quantities are dimensionless) as functions of wavelength for stoichiometric HfO_2 films prepared at deposition-averaged target power densities $<S_d> = 29–54\ W\ cm^{-2}$ and voltage pulse durations, t_1, ranging from 50 to 200 µs (Table 1).

films, that the flux of negative oxygen ions from the sputtered target is negligible in comparison with the flux of secondary electrons, and that the sputtering yield of metal atoms from the metallic fraction of the target, Y_{mm}, is the same for all incident ions, including the ionized sputtered metal atoms directed back to the target, and can be written [26,27] as $Y_{mm} = k_{sp}U_{da}^{0.5}$, where k_{sp} is a constant for a given metal and U_{da} is the pulse-averaged magnetron voltage. Then, the relation applicable to a non-reactive HiPIMS of metals [28,29] can be modified into the form

$$a_D \propto (1-\Theta_{tsa})(1-B_{ma})f_{trm}\frac{k_{sp}U_{da}^{-0.5}}{1+\gamma}<S_d>. \quad (4)$$

Here, Θ_{tsa} is the pulse-averaged compound fraction in the target surface layer, B_{ma} is the pulse-averaged probability of ionization and subsequent return of sputtered metal atoms onto the target, f_{trm} is the transport factor determining the fraction of the metal atoms sputtered from the target erosion area and not directed back to the target if ionized that strike the substrate area, and γ is the effective ion-induced secondary electron emission yield.

Let us recall that the flux of negative oxygen ions from the sputtered Zr target was low during ZrO_2 depositions with the to-substrate O_2 inlet at $t_1 = 50–200$ µs and $<S_d> = 51–53\ W\ cm^{-2}$ [21], and that the values of Θ_{tsa} were approximately 0.10 and 0.15 during these depositions at $t_1 = 200$ and 50 µs, respectively, and $<S_d> = 50\ W\ cm^{-2}$ according to our model predictions (unpublished).

Fig. 5 shows the transport factors, f_{trm}, appearing in relation (4), for Hf and Zr atoms sputtered from the metal target (diameter of 100 mm) and striking a detector (diameter of 8 mm) at the axis of the substrate (d = 100 mm) in an Ar atmosphere under various pressures. They were calculated using Monte-Carlo simulations. First, the initial angular and energy distribution of sputtered atoms at the target surface was determined using the SRIM code [24] which is a sputter simulation package with the binary collision approximation. The incident energy of

Ar^+ ions was assumed to be $\varepsilon = eU_{da}$, where $U_{da} = 500$ and 750 V are the pulse-averaged magnetron voltages during the ZrO_2 depositions at $<S_d> = 52$ W cm^{-2} and $t_1 = 200$ μs [21], and during the HfO_2 depositions at $<S_d> = 54$ W cm^{-2} and $t_1 = 200$ μs (Table 1), respectively. In the second step, the transport of the sputtered Hf and Zr atoms onto the substrate was simulated by the SIMTRA code [30], a Monte Carlo transport code for sputtered neutral atoms in a pure argon gas, i.e. without a reactive gas. In spite of the fact that the current version of the SIMTRA code, used in our simulations, can provide only very simplified description of the transport of sputtered metal atoms during reactive HiPIMS depositions, these results for f_{trm} contribute to qualitative explanation of the big differences in the deposition rates measured for the HfO_2 and ZrO_2 films (Fig. 4) at a total pressure close to 2 Pa (Table 1). Here, it should be mentioned that high degrees of ionization of sputtered metal atoms and process gas atoms and molecules, together with a gas rarefaction in front of the sputtered target, should be considered in simulations of the transport of sputtered metal atoms and their ions onto the substrate in HiPIMS discharges. Note that losses of the ionized sputtered metal atoms to chamber walls during this transport are usually higher than those of sputtered neutrals in HiPIMS discharges [31–33]. These additional effects are likely to further increase the difference in f_{trm} for deposition of HfO_2 and ZrO_2 films due to a significantly higher relative atomic mass of Hf ($m_{Hf} = 178.50$) than of Zr ($m_{Zr} = 91.22$).

A shortening of the voltage pulses from 200 to 50 μs during the HfO_2 depositions at approximately constant values of $<S_d> = 29–33$ W cm^{-2} (Table 1) resulted in rising values of the target power density in a discharge pulse from $S_{da} = 260–400$ W cm^{-2} at $U_{da} = 630–650$ V to $S_{da} = 1090–1260$ W cm^{-2} at $U_{da} = 895–900$ V. The rise in S_{da} leads to rapidly increasing probabilities of ionization of sputtered atoms in front of the target. As a consequence, the deposition rate, a_D, given by relation (4) and shown in Fig. 4, decreases mainly due to a higher backward flux of ionized sputtered metal atoms to the target (B_{ma}) which may be combined with higher losses of the metal ions, compared with neutrals, to chamber walls (lower f_{trm}). Moreover, the values of $U_{da}^{-0.5}$ in relation (4) also decrease and Θ_{tsa} may be slightly higher for shorter pulses according to our model predictions (unpublished).

Taking into account a probable small increase in B_{ma} and decrease in Θ_{tsa} in relation (4) with the increase in S_{da} from 260–400 W cm^{-2} at $U_{da} = 630–650$ V to 490–630 W cm^{-2} at $U_{da} = 740–760$ V during the HfO_2 depositions (Table 1), we can explain the rise in a_D from 195 to 345 nm/min (Fig. 4) predominantly as a result of the increase in $<S_d>$ from 33 to 54 W cm^{-2} at the same $t_1 = 200$ μs. The relatively high deposition rates (around 75%), compared with the Hf films, which were achieved for the densified stoichiometric HfO_2 films at $<S_d> \approx 30$ and 50 W cm^{-2}, and $t_1 = 200$ μs, are mainly due to a low Θ_{tsa} and a slightly increased γ (Fig. 3) during the HfO_2 depositions.

Taking into account a much smaller collisional scattering of the heavier Hf atoms, compared with the Zr atoms, during their transport onto the substrate at the total pressure close to 2 Pa used ($f_{trm} = 1.23 \times 10^{-3}$ for Hf at 750 eV Ar^+ ions and $f_{trm} = 9.05 \times 10^{-4}$ for Zr at 500 eV Ar^+ ions in Fig. 5), a higher sputtering yield of Hf than of Zr (1.30 times higher k_{sp} evaluated from the aforementioned sputtering yields for 600 eV Ar^+ ions) and a probably lower γ during HfO_2 depositions, compared with ZrO_2 depositions, under similar conditions (see $U_{da} = 740–760$ V for the HfO_2 deposition at $<S_d> = 54$ W cm^{-2} and $t_1 = 200$ μs, and $U_{da} = 485–515$ V for the ZrO_2 deposition at $<S_d> = 52$ W cm^{-2} and $t_1 = 200$ μs [21]), we can qualitatively explain using relation (4) the higher deposition rates achieved for the densified HfO_2 films, compared with the ZrO_2 films (Fig. 4).

Fig. 6 shows the deposition-averaged oxygen flow rate, $<\Phi_{ox}>$, characterizing the consumption of oxygen during a reactive deposition, and the $a_D/<\Phi_{ox}>$ ratio, characterizing the efficiency of the oxygen utilization in a reactive deposition. As seen in Fig. 6, we achieved a higher efficiency of the oxygen utilization at systematically higher values of $<\Phi_{ox}>$ for the HfO_2 deposition at $<S_d> = 54$ W cm^{-2} and $t_1 = 200$ μs than for the ZrO_2 deposition at $<S_d> = 52$ W cm^{-2} and $t_1 = 200$ μs, and even for the HfO_2 depositions at $<S_d> = 29–33$ W cm^{-2} than for the ZrO_2 depositions at $<S_d> = 51–53$ W cm^{-2}.

3.2. Structure and properties of films

Fig. 7 shows the film structure as studied by XRD. It can be seen that the HfO_2 films deposited exhibit a nanocrystalline structure with a dominant monoclinic phase (m-HfO_2, Card No. 34-0104 in Ref. [34]) and a preferred orientation of the m-HfO_2 (−111) planes parallel to the film surface. Asymmetry of the m-HfO_2 (−111) diffraction peak at $2\theta = 27.90°$ indicates a possible existence of a small amount of the tetragonal phase (t-HfO_2, Card No. 8-0342 in Ref. [34]) in the films. A shift of all m-HfO_2 diffraction peaks toward lower values of 2θ, compared with the standard values, for the films prepared at longer voltage pulses with $t_1 \geq 150$ μs is mainly due to a higher compressive stress $\sigma = 1.2–1.4$ GPa in these films (Table 1). At $t_1 = 50$ and 100 μs, the preferred orientation of the HfO_2 films is weakened and the diffraction peaks are broadened, mainly as a consequence of a decreasing grain size in the films. At present, a detailed analysis of the nanostructure of these films is carried out by means of high-resolution transmission electron microscopy and selected-area electron diffraction. The results will be given in a separate paper.

Optical properties of the HfO_2 films are presented in Fig. 8 and Table 1. The high values of n_{550} prove that all films are highly densified ($n_{550} = 2.07–2.12$) and that at least the films prepared at long $t_1 \geq 150$ μs are fully densified ($n_{550} = 2.11–2.12$). The densification is confirmed by the fact that refractive indices reported for HfO_2 previously are either similar ($n_{550} \leq 2.09$ [35], $n_{1000} = 2.05$ [16], $n_{550} \leq 2.02$ [results in Ref. [14]], $n_{550} \leq 2.1$ [overview in Ref. [14]]) or even significantly lower ($n_{550} \leq 1.94$ [3], $n_{550} \leq 1.94$ [36], $n_{550} = 1.90$ [6], $n_{550} \leq 1.89$ [37]). Even the refractive indices reported for cubic HfO_2 (which is known to have a higher bulk density than the more common monoclinic or tetragonal HfO_2) are comparable with the aforementioned values ($n_{600} = 2.08$ for bulk material [38] or $n = 2.125$ [39]).

In parallel, the very low values of $k_{550} \leq 1 \times 10^{-3}$ prove that the films are stoichiometric (i.e., the high n values are indeed due to the densification). Even at 300 nm instead of 550 nm (at 4.12 eV instead of 2.25 eV; i.e., much closer to the band gap edge), the extinction coefficient remains low: $k_{300} \leq 7 \times 10^{-3}$. This makes the films highly optically transparent in a wide wavelength range. For example, for a 1 μm thick slab the transmittance of a normal beam with a wavelength of 550 nm (assuming $n_{550} = 2.12$) would be 77% at $k_{550} = 0$ and 75% at $k_{550} = 1 \times 10^{-3}$, and the transmittance of a normal beam with a wavelength of 300 nm (assuming $n_{300} = 2.26$) would be 74% at $k_{300} = 0$ and 55% at $k_{300} = 7 \times 10^{-3}$ (without considering the interference). It means that even for the highest k observed and for all wavelengths considered, the absorption would still be lower (for most wavelengths significantly lower) than the reflection (which takes place at any k). Moreover, the highest observed $k_{550} = 1 \times 10^{-3}$ (at $k_{300} = 7 \times 10^{-3}$) is exhibited only by the single film prepared at the highest $<S_d> = 54$ W cm^{-2}, while at $<S_d>$ around 30 W cm^{-2} the optical quality of the films is even higher: k_{550} between $\leq 0.1 \times 10^{-3}$ and 0.6×10^{-3} (at k_{300} between 1.5×10^{-3} and 7.0×10^{-3}).

Note that despite the very high deposition rates, the values of $k_{550} \leq 1 \times 10^{-3}$ achieved for the HfO_2 films are even lower than $k_{550} \leq 6 \times 10^{-3}$ achieved for isostructural ZrO_2 films prepared by the same technique [20]. The same trend resulting from the transition from ZrO_2 to HfO_2 was reported for k_{350} in Ref. [16].

Furthermore, Table 1 shows that the film densification (expressed in terms of n) is related to and further confirmed by the high film hardness: $H = 15$ GPa for the film prepared at the shortest $t_1 = 50$ μs (and exhibiting the lowest observed $n_{550} = 2.07$) and even $H = 18$ GPa at $t_1 \geq 100$ μs. Also the H values are fully comparable with or even higher than those reported in the literature, see e.g. 12–15 GPa or 9–13 GPa in the overview in Refs. [8] and [40], respectively. The compressive

stress in the films is consistent with their densification as well: $\sigma = 0.5$–0.7 GPa for both samples which exhibit the relatively lowest $n_{550} = 2.07$, and $\sigma = 1.2$–1.4 GPa for the samples which exhibit $n_{550} = 2.11$–2.12.

In spite of the p_{ox} oscillations during film depositions (Table 1 and Fig. 2), no multilayer structures of the films or periodic changes in their compositions and properties were observed.

4. Conclusions

High-power impulse magnetron sputtering (HiPIMS) with a pulsed reactive gas (oxygen) flow control was used for high-rate reactive depositions of densified, highly optically transparent, stoichiometric HfO_2 films onto floating substrates at the distance of 100 mm from the target.

We showed that the HfO_2 films can be prepared with very high deposition rates (up to 200 nm/min) at a deposition-averaged target power density of approximately 30 W cm^{-2}, which is relatively close to a target power density applicable in industrial HiPIMS systems. The films were nanocrystalline with a dominant monoclinic phase. They exhibited a hardness of 15–18 GPa, a refractive index of 2.07–2.12 and an extinction coefficient between $\leq 0.1 \times 10^{-3}$ and 0.6×10^{-3} (both quantities at the wavelength of 550 nm). At 300 nm, the extinction coefficient was between 1.5×10^{-3} and 7.0×10^{-3}.

A simplified relation for the deposition rate of films prepared by a reactive HiPIMS was presented and used to qualitatively explain the dependences and very high values measured for the deposition rate of the HfO_2 films.

Acknowledgment

This work was supported by the Grant Agency of the Czech Republic under Project No. GA14-03875S.

References

[1] A.J. Waldorf, J.A. Dobrowolski, B.T. Sullivan, L.M. Plante, Optical coatings deposited by reactive ion plating, Appl. Opt. 32 (1993) 5583–5593.
[2] M. Fadel, O.A. Azim M., O.A. Omer, R.R. Basily, A study of some optical properties of hafnium dioxide (HfO_2) thin films and their applications, Appl. Phys. A Mater. Sci. Process. 66 (1998) 335–343.
[3] J. Ni, Y. Zhu, S. Wang, Z. Li, Z. Zhang, B. Wei, Nanostructuring HfO_2 thin films as antireflection coatings, J. Am. Ceram. Soc. 92 (2009) 3077–3080.
[4] V. Pervak, F. Krausz, A. Apolonski, Hafnium oxide thin films deposited by reactive middle-frequency dual-magnetron sputtering, Thin Solid Films 515 (2007) 7984–7989.
[5] P. Torchio, A. Gatto, M. Alvisi, G. Albrand, N. Kaiser, C. Amra, High-reflectivity HfO_2/SiO_2 ultraviolet mirrors, Appl. Opt. 41 (2002) 3256–3261.
[6] M.F. Al-Kuhaili, Optical properties of hafnium oxide thin films and their application in energy-efficient windows, Opt. Mater. 27 (2004) 383–387.
[7] J.H. Choi, Y. Mao, J.P. Chang, Development of hafnium based high-k materials — a review, Mater. Sci. Eng. R. Rep. 72 (2011) 97–136.
[8] J. Wang, H.P. Li, R. Stevens, Hafnia and hafnia-toughened ceramics, J. Mater. Sci. 27 (1992) 5397–5430.
[9] K. Matsumoto, Y. Itoh, T. Kameda, EB-PVD process and thermal properties of hafnia-based thermal barrier coating, Sci. Technol. Adv. Mater. 4 (2003) 153–158.
[10] J. Singh, D.E. Wolfe, R.A. Miller, J.I. Eldridge, D.M. Zhu, Tailored microstructure of zirconia and hafnia-based thermal barrier coatings with low thermal conductivity and high hemispherical reflectance by EB-PVD, J. Mater. Sci. 39 (2004) 1975–1985.
[11] R.K. Jain, Y.K. Gautam, V. Dave, A.K. Chawla, R. Chandra, A study on structural, optical and hydrophobic properties of oblique angle sputter deposited HfO_2 films, Appl. Surf. Sci. 283 (2013) 332–338.
[12] K. Sarakinos, D. Music, S. Mráz, M. To Baben, K. Jiang, F. Nahif, et al., On the phase formation of sputtered hafnium oxide and oxynitride films, J. Appl. Phys. 108 (2010) 014904.
[13] G. Aygun, A. Cantas, Y. Simsek, R. Turan, Effects of physical growth conditions on the structural and optical properties of sputtered grown thin HfO_2 films, Thin Solid Films 519 (2011) 5820–5825.
[14] T.J. Bright, J.I. Watjen, Z.M. Zhang, C. Muratore, A.A. Voevodin, Optical properties of HfO_2 thin films deposited by magnetron sputtering: From the visible to the far-infrared, Thin Solid Films 520 (2012) 6793–6802.
[15] M. Szymanska, S. Gieraltowska, L. Wachnicki, M. Grobelny, K. Makowska, R. Mroczynski, Effect of reactive magnetron sputtering parameters on structural and electrical properties of hafnium oxide thin films, Appl. Surf. Sci. 301 (2014) 28–33.
[16] M. Audronis, A. Matthews, K. Juškevičius, R. Drazdys, Unlocking the potential of voltage control for high rate zirconium and hafnium oxide deposition by reactive magnetron sputtering, Vacuum 107 (2014) 159–163.
[17] I. Safi, Recent aspects concerning DC reactive magnetron sputtering of thin films: a review, Surf. Coat. Technol. 127 (2000) 203–218.
[18] J. Musil, P. Baroch, J. Vlček, K.H. Nam, J.G. Han, Reactive magnetron sputtering of thin films: present status and trends, Thin Solid Films 475 (2005) 208–218.
[19] W.D. Sproul, D.J. Christie, D.C. Carter, Control of reactive sputtering processes, Thin Solid Films 491 (2005) 1–17.
[20] J. Vlček, J. Rezek, J. Houška, R. Čerstvý, R. Bugyi, Process stabilization and a significant enhancement of the deposition rate in reactive high-power impulse magnetron sputtering of ZrO_2 and Ta_2O_5 films, Surf. Coat. Technol. 236 (2013) 550–556.
[21] J. Vlček, J. Rezek, J. Houška, T. Kozák, J. Kohout, Benefits of the controlled reactive high-power impulse magnetron sputtering of stoichiometric ZrO_2 films, Vacuum 114 (2015) 131–141.
[22] P. Kudláček, J. Vlček, K. Burcalová, J. Lukáš, Highly ionized fluxes of sputtered titanium atoms in high-power pulsed magnetron discharges, Plasma Sources Sci. Technol. 17 (2008) 025010.
[23] J.D. Cox, D.D. Wagman, V.A. Medvedev, CODATA Key Values for Thermodynamics, Hemisphere Publishing Corp., New York, 1989.
[24] J.F. Ziegler, M.D. Ziegler, J.P. Biersack, SRIM 2008 — stopping and range of ions in matter (software package)available at http://www.srim.org.
[25] J. Gunnars, U. Wiklund, Determination of growth-induced strain and thermo-elastic properties of coatings by curvature measurements, Mater. Sci. Eng. A 336 (2002) 7–21.
[26] A. Anders, Self-sputtering runaway in high power impulse magnetron sputtering: the role of secondary electrons and multiply charged metal ions, Appl. Phys. Lett. 92 (2008) 1–3.
[27] M.A. Lieberman, A. Lichtenberg, Principles of plasma discharges and materials processing, 2nd edn, Wiley-Interscience, New York, 2005.
[28] J. Vlček, K. Burcalová, A phenomenological equilibrium model applicable to high-power pulsed magnetron sputtering, Plasma Sources Sci. Technol. 19 (2010) 065010.
[29] T. Kozák, J. Vlček, Š. Kos, Transport and ionization of sputtered atoms in high-power impulse magnetron sputtering discharges, J. Phys. D. Appl. Phys. 46 (2013) 105203.
[30] K. Van Aeken, S. Mahieu, D. Depla, The metal flux from a rotating cylindrical magnetron: a Monte Carlo simulation, J. Phys. D. Appl. Phys. 41 (2008) 205307.
[31] K. Sarakinos, J. Alami, S. Konstantinidis, High power pulsed magnetron sputtering: a review on scientific and engineering state of the art, Surf. Coat. Technol. 204 (2010) 1661–1684.
[32] D. Lundin, K. Sarakinos, An introduction to thin film processing using high-power impulse magnetron sputtering, J. Mater. Res. 27 (2012) 780–792.
[33] J.T. Gudmundsson, N. Brenning, D. Lundin, U. Helmersson, High power impulse magnetron sputtering discharge, J. Vac. Sci. Technol. A 30 (2012) 030801.
[34] JCPDS-ICDD, PDF-2 Database Sets 1-47, International Centre for Diffraction Data, Newton Square, PA, USA, 1997.
[35] M. Vargas, N.R. Murphy, C.V. Ramana, Structure and optical properties of nanocrystalline hafnium oxide thin films, Opt. Mater. 37 (2014) 621–628.
[36] V. Dave, H.O. Gupta, R. Chandra, Nanostructured hydrophobic DC sputtered inorganic oxide coating for outdoor glass insulators, Appl. Surf. Sci. 295 (2014) 231–239.
[37] J.M. Khoshman, M.E. Kordesch, Optical properties of a-HfO_2 thin films, Surf. Coat. Technol. 201 (2006) 3530–3535.
[38] D.L. Wood, K. Nassau, T.Y. Kometani, D.L. Nash, Optical properties of cubic hafnia stabilized with yttria, Appl. Opt. 29 (1990) 604–607.
[39] D. Mergel, M. Jerman, Density and refractive index of thin evaporated films, Chin. Opt. Lett. 8 (2012) 67–72.
[40] Y. Al-Khatatbeh, K.K.M. Lee, B. Kiefer, Phase diagram up to 105 GPa and mechanical strength of HfO_2, Phys. Rev. B 82 (2010) 144106.

B. Microstructure of hard and optically transparent HfO_2 films prepared by high-power impulse magnetron sputtering with a pulsed oxygen flow control

N. W. Pi, M. Zhang, J. Jiang, A. Belosludtsev, J. Vlček, J. Houška, E. I. Meletis

Thin Solid Films 619 (2016) 239-249

Thin Solid Films 619 (2016) 239–249

Contents lists available at ScienceDirect

Thin Solid Films

journal homepage: www.elsevier.com/locate/tsf

Microstructure of hard and optically transparent HfO_2 films prepared by high-power impulse magnetron sputtering with a pulsed oxygen flow control

Nai-Wen Pi [a], Minghui Zhang [a], Jiechao Jiang [a], Alexandr Belosludtsev [b], Jaroslav Vlček [b], Jiří Houška [b], Efstathios I. Meletis [a,*]

[a] Department of Materials Science and Engineering, The University of Texas at Arlington, Arlington, TX 76019, USA
[b] Department of Physics and NTIS, European Centre of Excellence, University of West Bohemia, Univerzitní 8, 306 14 Plzeň, Czech Republic

ARTICLE INFO

Article history:
Received 31 May 2016
Received in revised form 12 September 2016
Accepted 30 October 2016
Available online 3 November 2016

Keywords:
HfO_2 films
Reactive HiPIMS
High-resolution transmission electron microscopy
Electron diffraction
Dense nano-columnar structure

ABSTRACT

Reactive high-power impulse magnetron sputtering was used to deposit HfO_2 films on Si substrates using a voltage pulse duration, t_1, from 100 to 200 μs and an deposition-averaged target power density, $<S_d>$, from 7.2 to 54 Wcm^{-2}. The effects of these processing parameters on the microstructure and properties of the films were studied by atomic force microscopy, nano-indentation, X-ray diffraction, electron diffraction and high-resolution transmission electron microscopy. Four HfO_2 films were prepared with (1) $t_1 = 100$ μs, $<S_d> = 7.2$ Wcm^{-2} (T100S7), (2) $t_1 = 200$ μs, $<S_d> = 7.3$ Wcm^{-2} (T200S7), (3) $t_1 = 200$ μs, $<S_d> = 18$ Wcm^{-2} (T200S18) and (4) $t_1 = 200$ μs, $<S_d> = 54$ Wcm^{-2} (T200S54). All films were found to be composed of an interlayer next to the Si interface followed by a nano-columnar structure layer. The interlayer structure of the films was found to contain a population of lower density nanoscale regions. A reduction in $<S_d>$ in films T200S54, T200S18, T200S7 and T100S7 caused an increase in the interlayer thickness and a decrease in the width of the nano-columnar structures from ~46 nm to ~21 nm. This microstructural change was accompanied by a concomitant change of the grain boundary structure from tight and interlocking in films T200S54 and T200S18, to rough and thicker (~1 nm) boundaries in films T200S7 and T100S7. Films prepared with larger $t_1 = 200$ μs have a monoclinic HfO_2 structure and that with smaller $t_1 = 100$ μs exhibits a mixture of monoclinic and orthorhombic HfO_2. A high hardness of 17.0–17.6 GPa was shown for films with a monoclinic HfO_2 structure. The films exhibited a refractive index of 2.02–2.11 and an extinction coefficient between 0.1×10^{-3} and 1×10^{-3} (both at a wavelength of 550 nm). High refractive index was achieved for films T200S54 and T200S18 owing to the presence of a dense microstructure with sharp and interlocking grain boundaries.

© 2016 Elsevier B.V. All rights reserved.

1. Introduction

Hafnium dioxide (HfO_2) has become an important coating material due to its attractive properties. They include high melting point (~2800 °C) and excellent thermal stability, high refractive index and low absorption over a broad region (from the near-UV, ~250 nm to the mid-IR, >12 μm), high dielectric constant and high neutron absorption cross section [1]. HfO_2 can find a wide range of applications (semiconductors, optical devices, nuclear industries and coating technologies). For example, HfO_2-based materials have been explored as thermal barrier coatings for turbine blades operating in harsh and high-temperature environments [2,3]. HfO_2 films can be used as visible, near-IR and mid-IR antireflection coatings [4–6], UV mirrors with a high damage threshold [7], heat mirrors for energy-efficient windows [8] and chirped mirrors and band pass filters [9]. HfO_2 is also considered to be one of the most promising candidates to replace SiO_2 on Si in gated electronic devices [10].

Reactive dc magnetron sputtering is a suitable technique to deposit HfO_2 films [9,11–17]. High-power impulse magnetron sputtering (HiPIMS) with a pulsed reactive gas (oxygen) flow control was recently used for high-rate reactive depositions of densified, highly optically transparent, stoichiometric HfO_2 films onto floating substrates [18]. The depositions were performed using a strongly unbalanced magnetron with a directly water-cooled planar Hf target in argon-oxygen gas mixtures. With this method, the HfO_2 films can be fabricated with very high deposition rates (up to 200 nm/min) at an averaged target power density of approximately 30 Wcm^{-2}. The latter is relatively close to a target power density applicable in industrial HiPIMS systems. The HfO_2 films prepared using this technique were hard and exhibited a hardness up to 18 GPa, a refractive index of 2.07–2.12 and an extinction coefficient between ≤0.1×10^{-3} and 0.6×10^{-3} at the wavelength of

* Corresponding author.
E-mail address: meletis@utaedu (E.I. Meletis).

http://dx.doi.org/10.1016/j.tsf.2016.10.059
0040-6090/© 2016 Elsevier B.V. All rights reserved.

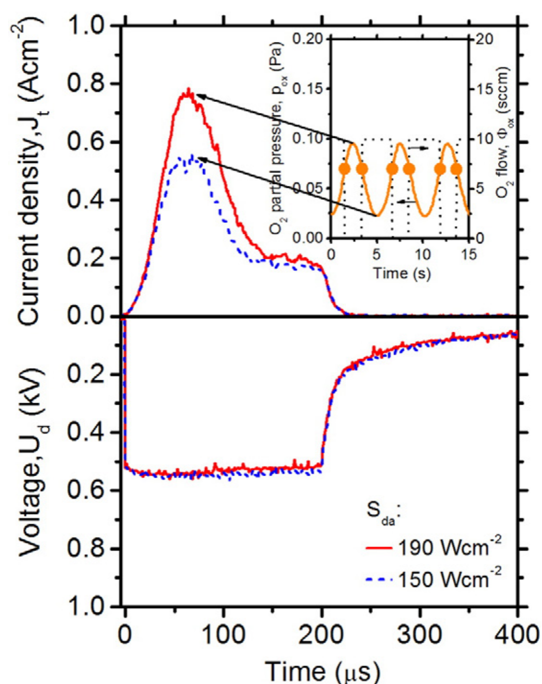

Fig. 1. Waveforms of the magnetron voltage, U_d, and the target current density (over total area of the target), J_t, for $<S_d> = 18$ Wcm^{-2} and $t_1 = 200$ μs with the pulse-averaged target power densities $S_{da} = 150$ Wcm^{-2} and 190 Wcm^{-2} relating to the minimum and maximum values of the oxygen partial pressure, p_{ox}, respectively, during preparation of the T200S18 film (Table 1). The pre-selected critical value of $p_{ox} = 0.07$ Pa determining the switching-on and switching-off of the oxygen flow rate $\Phi_{ox} = 10$ sccm in this case is marked by dots.

550 nm. In spite of the oscillating oxygen partial pressure during film depositions, no periodic changes in their compositions were observed [18].

In this work, we have employed high-resolution transmission electron microscopy (HRTEM) and electron diffraction to study the microstructure of four selected representative hard and optically transparent HfO_2 films prepared by high-rate HiPIMS [18]. The motivation for this work was to develop an understanding of the processing-microstructure-property relationship of these films as a function of the deposition parameters, namely deposition-averaged target power density, $<S_d>$, and voltage pulse duration, t_1. As an important part of these efforts, we examine (by techniques complementary to those employed in Ref. [18]) whether the feed-back pulsed oxygen flow control (oscillating oxygen partial pressure, and consequently oscillating discharge current and power, on a scale of seconds, see Fig. 1) does or does not lead to a layered structure of the films.

2. Experimental details

2.1. Film preparation

The HfO_2 films were deposited onto Si substrates at a floating potential using a strongly unbalanced magnetron sputter source with a directly water-cooled planar hafnium target (99.9% Hf purity, diameter of 100 mm and thickness of 6 mm) in a standard stainless-steel vacuum chamber. The target-to-substrate distance was 100 mm. The target surface temperature was kept under 350 °C by using water cooling [19]. The substrate temperature, T_s, reached during depositions without an external heater, was in the range from 80 to 155 °C (see Table 1). The base pressure before deposition was 10^{-3} Pa and a reactive gas (oxygen) was admitted into the vacuum chamber from a source via mass flow controllers and two corundum conduits for deposition. Two O_2 inlets with a diameter of 1 mm were placed symmetrically above the target racetrack at the same distance of 20 mm from the target surface and oriented to the substrate [18]. The total pressure of the argon–oxygen gas mixtures was kept close to 2 Pa with the same argon partial pressure of 2 Pa for all depositions. The magnetron was driven by a high-power pulsed dc power supply (HMP 2/1, Hüttinger Elektronik). The repetition frequency, f_r, was 500 Hz. The range for t_1 was from 100 to 200 μs and that for $<S_d>$ was from 7.2 to 54 Wcm^{-2}. Prior to a given deposition, we fix the nominal target power at an essentially constant magnetron voltage during discharge pulses, a preset argon partial pressure, a total oxygen flow rate in both conduits, Φ_{ox}, the O_2 inlet configuration, and a pre-selected critical value (Fig. 1) of the partial pressure of oxygen in the chamber, $p_{ox}(t)$, which was chosen to be the control process parameter in this case. During the deposition, a process controller used then provides a control feed-back signal to the two O_2 mass flow controllers to adjust the pulsed Φ_{ox} into the vacuum chamber (Φ_{ox} = const or 0) by adjusting the duration of the Φ_{ox} pulses by means of the pre-selected critical value of $p_{ox}(t)$, which is monitored by the process controller. This feed-back process control is able to maintain a sputter deposition of stoichiometric films in the region between a more and less metallic mode, and to utilize exclusive benefits of the HiPIMS discharges in preparation of films [20]. Fig. 1 shows the basic principle of the pulsed oxygen flow control and discharge characteristics during a controlled reactive sputter deposition of the stoichiometric HfO_2 film at $<S_d> =$ 18 Wcm^{-2} and $t_1 = 200$ μs (T200S18 film in Table 1). A detailed description of the film deposition parameters is given in Ref. [18]. Four films were prepared in this work (Table 1) for detailed microstructure characterization with (1) $t_1 = 100$ μs, $<S_d> = 7.2$ Wcm^{-2} (T100S7); (2) $t_1 = 200$ μs, $<S_d> = 7.3$ Wcm^{-2} (T200S7); (3) $t_1 = 200$ μs, $<S_d> = 18$ Wcm^{-2} (T200S18) and (4) $t_1 = 200$ μs, $<S_d> =$ 54 Wcm^{-2} (T200S54). All these films exhibited a stoichiometric HfO_2 composition [18].

2.2. Film characterization

The surface morphology of the HfO_2 films was investigated using atomic force microscopy (AFM) in a Park XE 70 AFM system using a tapping mode. The crystallographic structure of the films was studied by X-ray diffraction (XRD) in a Bruker D8 Advance Diffractometer using Cu K_α radiation at room temperature. The microstructure of the films was studied by TEM. Cross-section and plan-view TEM specimens were prepared by the procedure of mechanical grinding, polishing, dimpling and Ar-ion milling. Selected-area electron diffraction (SAED) patterns and HRTEM images were recorded in a Hitachi H-9500 electron microscope (300 keV). Nano-indentation measurements were performed in a Hysitron Ubi 1 Nanomechanical Test Instrument to

Table 1
Deposition parameters and material characteristics of HfO_2 films: voltage pulse duration, t_1, deposition-averaged target power density, $<S_d>$, pulse-averaged target power density, S_{da}, pulse-averaged magnetron voltage, U_{da}, deposition rate, a_D, substrate temperature, T_s, texture structure, crystal structure, column width, interlayer thickness, hardness, H, effective Young's modulus, E^*, and extinction coefficient, k_{550}, and refractive index, n_{550}, of the films at a wavelength of 550 nm.

Film No.	t_1 (μs)	$<S_d>$ (Wcm^{-2})	S_{da} (Wcm^{-2})	U_{da} (V)	a_D (nm/min)	T_s (°C)	Texture structure	Crystal structure	Column width (nm)	Interlayer thickness (nm)	H (GPa)	E^* (GPa)	k_{550} (10^{-3})	n_{550}
T200S54	200	54	490–630	750	345	≤155	No	m-HfO_2	46	10	17.6	176.8	1.0	2.11
T200S18	200	18	150–190	535	95	≤130	Yes	m-HfO_2	38	55	17.5	176.5	0.3	2.07
T200S7	200	7.3	45–80	430	30	≤90	Yes	m-HfO_2	24	60	17.0	176.0	0.2	2.02
T100S7	100	7.2	90–150	510	25	≤80	Yes	m + o-HfO_2	21	60	13.4	162.0	0.1	2.02

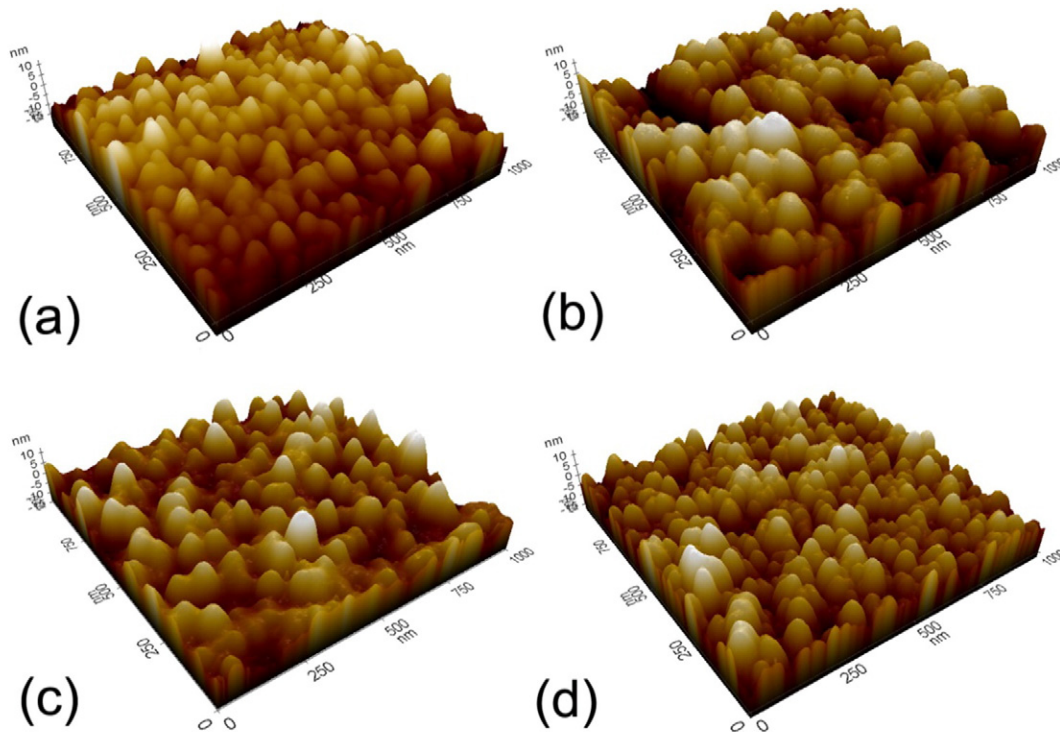

Fig. 2. Non-contact AFM 3D images of HfO_2 films (a) T200S54, (b) T200S18, (c) T200S7 and (d) T100S7.

determine film hardness, H, and the effective Young's modulus, $E^* = E / (1 - \nu^2)$, where E and ν are the Young's modulus and Poisson's ratio, respectively. A cube corner diamond tip was used for the measurements.

The refractive index, n, and extinction coefficient, k, were determined by variable angle spectroscopic ellipsometry (VASE) using a J.A. Woollam Co. Inc. instrument. The measurements were performed using angles of incidence of 65°, 70° and 75° in reflection and the optical data were fitted using the WVASE software. The optical constants averaged over the film thickness (Table 1) were obtained using an optical model consisting of a c-Si substrate, a homogeneous HfO_2 layer described by the Cauchy dispersion formula with an Urbach absorption tail and a surface roughness layer. In addition, the thin interlayer observed by TEM (see below) was characterized using an alternative optical model in which the interlayer was represented by an additional layer (with the thickness given by TEM) described by the Cauchy dispersion formula, inserted just above the Si substrate. The n_{550} and k_{550} values were obtained at the specific wavelength of 550 nm.

3. Results and discussion

3.1. AFM studies

The surface morphology and roughness of four HfO_2 films were investigated using AFM in the non-contact mode with a scanning size of $1 \times 1\ \mu m^2$. Fig. 2(a), (b) and (c) show 3D AFM images of films T200S54, T200S18 and T200S7, respectively, exhibiting a coarser granular structure. The structures in the three films have a similar grain size varying from 25 nm to 120 nm in diameter with an average size of ~70 nm. Fig. 2(d) shows 3D AFM image of the film T100S7, exhibiting smaller granular structures compared to the former three films. These granular structures have a size varying from 20 nm to 80 nm with an average size of ~45 nm. All films were smooth and the average mean roughness, R_a, was ~0.66 nm, 1.07 nm, 0.60 nm and 0.85 nm for films T200S54, T200S18, T200S7 and T100S7, respectively.

3.2. XRD studies

We examined the crystal structure of the films using θ-2θ XRD prior to conducting systematic TEM analysis (Fig. 3). It should be noted that HfO_2 has been reported to have four possible crystal structures: monoclinic (m-HfO_2, PDF#: 01-075-6426, $\boldsymbol{a} = 5.1187$ Å, $\boldsymbol{b} = 5.1693$ Å, $\boldsymbol{c} = 5.297$ Å, $\boldsymbol{\beta} = 99.18°$, $P2_1/c$) [21], orthorhombic (o-HfO_2, PDF#: 01-070-2832, $\boldsymbol{a} = 5.0073$ Å, $\boldsymbol{b} = 5.2276$ Å, $\boldsymbol{c} = 5.058$ Å, *Pbcm*) [21], tetragonal (t-HfO_2, PDF#: 08-0342: $\boldsymbol{a} = 5.14$ Å, $\boldsymbol{c} = 5.25$ Å, *P42/nmc*) [21] and cubic (fcc, a = 5.11 Å) [22]. Formation of orthorhombic HfO_2 phase has been reported in Ref. [12]. Selected peaks of the monoclinic and orthorhombic HfO_2 phase are marked in Fig. 3.

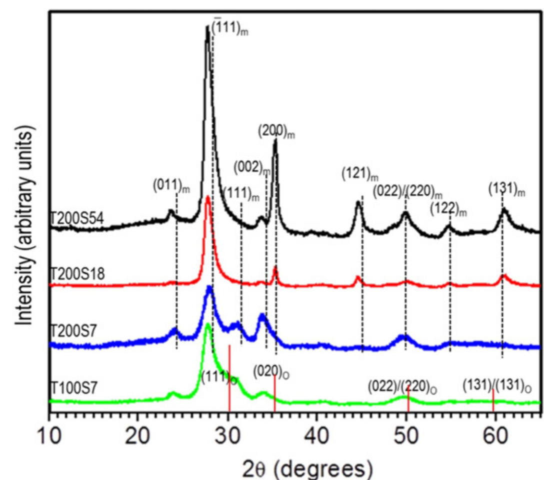

Fig. 3. XRD patterns of the T200S54, T200S18, T200S7 and T100S7 film. The dotted and solid lines indicate the 2θ positions of the monoclinic HfO_2 and orthorhombic HfO_2 phase, respectively.

As can be seen in Fig. 3, the XRD patterns from the T200S54 and T200S18 films exhibit peaks at 2θ positions of 23.62°, 27.76°, 33.74°, 35.34°, 44.66°, 49.94°, 54.76° and 60.92° corresponding to lattice spacing of 3.76 Å, 3.21 Å, 2.65 Å, 2.54 Å, 2.03 Å, 1.82 Å, 1.67 Å, 1.52 Å, respectively. Those peaks can be identified as the (011), ($\bar{1}$11), (002), (200), (121), (022)/(220), (122) and (131) of the monoclinic HfO_2 structure. The asymmetry present in the ($\bar{1}$1111) of film T200S18 can be attributed to possible existence of a second phase or to texture in this film.

The XRD patterns of the T200S7 and T100S7 films exhibit *broad* peaks at 2θ positions of 24.08°, 27.9°, 31.03°, 33.9°, 49.7° and 54.76° corresponding to lattice spacing of 3.69 Å, 3.19 Å, 2.88 Å, 2.64 Å, 1.83 Å and 1.67 Å, respectively. Those peaks *are also consistent with* the (011), ($\bar{1}$11), (111), (002), (022) and (122) of the m-HfO_2 structure [21]. However, the latter peaks are broad and the presence of another phase can't be excluded.

3.3. HRTEM investigation

The detail microstructure of the films was studied using cross-section and plan-view TEM. The cross-section TEM images of all four films show a very uniform and smooth film surface and a sharp interface with the Si substrate. The T200S54, T200S18, T200S7 and T100S7 film thickness obtained from the cross-section TEM measurements was about 1000 nm, 1100 nm, 1000 nm and 960 nm, respectively.

3.3.1. Films T200S54 and T200S18

Films T200S54 and T200S18 exhibited a grain structure separated by thin boundaries as shown by the plan-view TEM images in Fig. 4(a) and (b). The grain boundaries possess a uniform thickness. The HfO_2 grains in T200S54 film have an average size of ~46 nm, larger than those in T200S18 (~38 nm). Fig. 4(c) and (d) are SAED patterns taken from film T200S54 and T200S18, respectively. The diffraction rings 1, 2, 3, 4, 5, 6, 7 and 8 in Fig. 4(c) have a lattice spacing of 5.02 Å, 3.71 Å, 3.15 Å, 2.83 Å, 2.59 Å, 2.33 Å, 2.18 Å and 2.03 Å which can be determined to be the (100), (011), ($\bar{1}$11), (111), (200), (012), ($\bar{1}$21) and (121) or (112) of the m-HfO_2 (PDF#: 01-075-6426) [23], respectively. The diffraction rings 1, 2, 3, 4, 5 and 6 in Fig. 4(d) have the same lattice spacing as those in Fig. 4(c) indicating that the T200S18 film has also a m-HfO_2 structure. The intensity of the diffractions in Fig. 4(c) doesn't exhibit clear inhomogeneity over the rings indicating that there is no texture in film T200S54. However, the diffraction rings 3 and 5 in Fig. 4(d) exhibit clear and strong inhomogeneity in intensity. Roughly, half of the symmetric quarter of the rings 3 and 5 in Fig. 4(d) show diffractions attesting to the presence of texture in the T200S18 film.

Fig. 5(a) is a typical cross-section TEM image of the T200S54 film taken from an area away from the Si substrate presenting columnar structures with a column width of ~46 nm. Fig. 5(b) is a SAED pattern taken from the latter HfO_2 columnar structures. Similar to Fig. 4(c), no strong inhomogeneous distribution of diffraction intensity along the rings was observed further confirming the absence of texture in this film. Observations revealed the presence of a HfO_2 interlayer just above the interface with the Si substrate before the formation of the columnar structure, Fig. 5(c). The interlayer has a continuous homogenous structure and a hilly interface with respect to the columnar structure with a thickness of ~10 nm.

Fig. 5(d) and (f) are typical cross-section TEM images of film T200S18 taken from an area away and close to the Si substrate, respectively. The T200S18 film possesses also a columnar structure, similar to T200S54. The interlayer in the T200S18 film is, however, much thicker than that in T200S54 with a thickness of ~55 nm. Fig. 5(e) is a SAED pattern taken from the HfO_2 columnar structures in the T200S18 film showing strong inhomogeneous distribution of diffraction intensity along the rings further indicating formation of texture in the HfO_2 columnar structures.

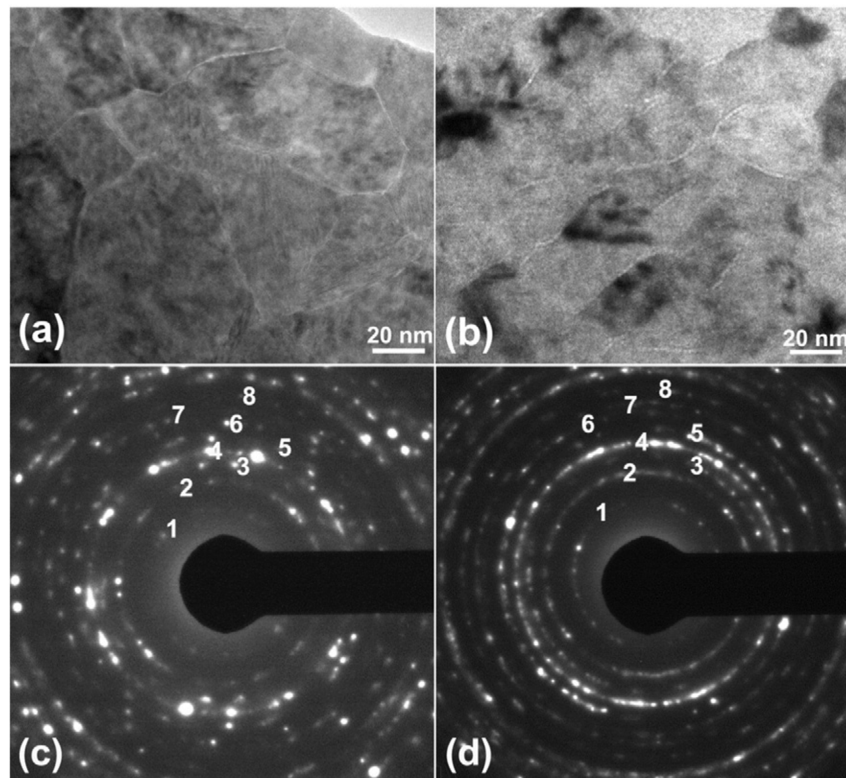

Fig. 4. (a), (b) Plan-view TEM image, (c), (d) SAED pattern of the T200S54 and T200S18 film, respectively.

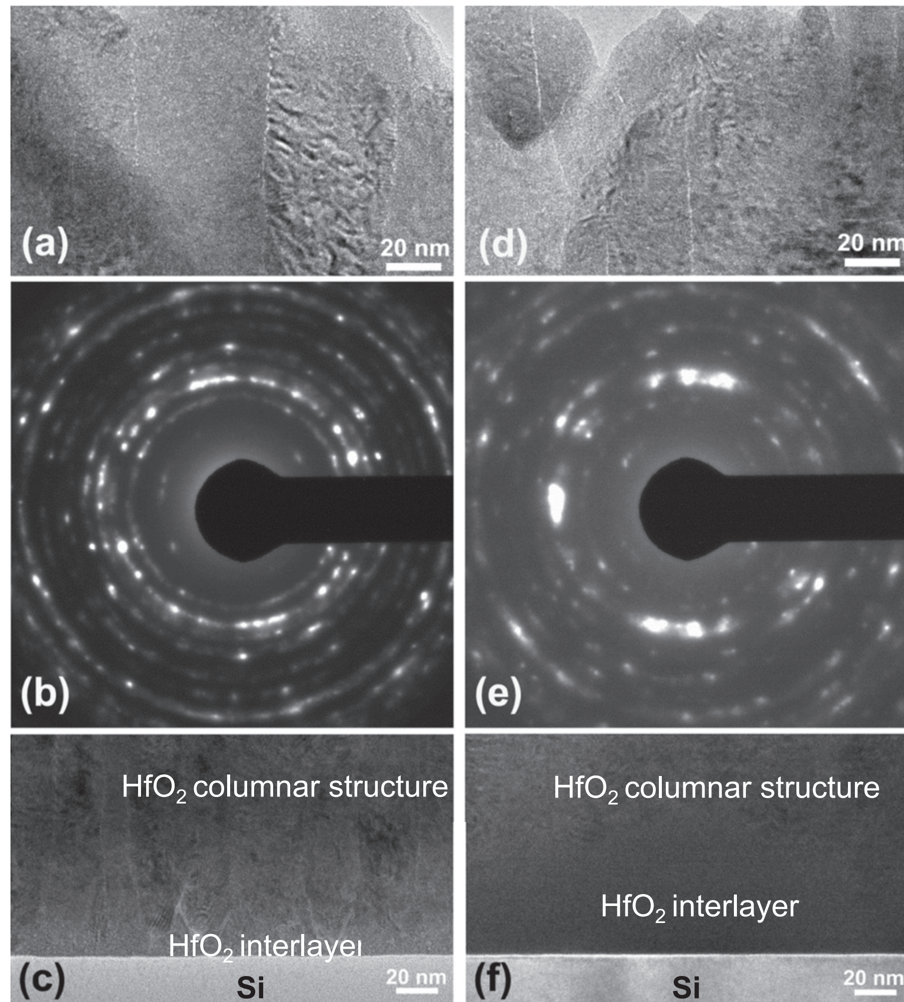

Fig. 5. (a), (d) Cross-section TEM image of the HfO_2 film taken from T200S54 and T200S18, respectively. (b), (e) SAED pattern taken from the HfO_2 film in T200S54 and T200S18, respectively. (c), (f) Cross-section TEM image of the film/Si interface in T200S54 and T200S18, respectively.

Fig. 6(a) and (b) are HRTEM images taken from the film area that contains columnar structures in plan-view TEM foils of T200S54 and T200S18 film, respectively. The grains in both images are directly and tightly attached to each other with uniform thin and atomically sharp boundaries. Nanoscale lower density regions with a size of 2–3 nm were more frequently observed in Fig. 6(b) than in Fig. 6(a) indicating that theT200S18 film may possess larger volume fraction of lower density regions.

Fig. 7(a) is a cross-section HRTEM image of the T200S54 HfO_2 film showing two columnar structures (C_1 and C_2) and a boundary in between. It was observed that each column has a single crystal structure regardless of the formation of lower density nanoscale regions within each grain. The interface between the HfO_2 interlayer and Si substrate in T200S54 is shown by the HRTEM image in Fig. 7(b). The HfO_2 interlayer is composed of a nanocrystalline structure with a size of several nm and is well attached to the Si substrate. Fig. 7(c) is a magnified cross-section TEM image of T200S18 film showing the HfO_2 interlayer, columnar structure layer and their interface. Contrary to the columnar structure area (C_0), a high population of lower density nanoscale regions were observed in the interlayer region (I). However, the interlayer region (I) is a highly crystalline structure despite the high population of the lower density regions, Fig. 7(d). The crystal size in region (I) in T200S18 is in the 10s of nm, much larger than that in T200S54, Fig. 7(b). It is interesting to note that an abrupt drop in the frequency of these nanoscale regions occurs across the boundary from region I to C_0, Fig. 7(d).

Film T200S54 deposited with $t_1 = 200$ μs and $\langle S_d \rangle = 54$ Wcm^{-2} consists of a continuous interlayer with a thickness of ~10 nm and columnar structures with a width of ~46 nm. The nano-columnar structures were interlocked directly without formation of amorphous boundaries. Film T200S54 has a m-HfO_2 structure without any texture. Such a film microstructure possesses a $H = 17.6$ GPa, $E^* = 176.8$ GPa, low $k_{550} = 1.0 \times 10^{-3}$ and high $n_{550} = 2.11$ (Table 1).

Film T200S18 was produced by reducing $\langle S_d \rangle$ from 54 Wcm^{-2} to 18 Wcm^{-2} while keeping the same $t_1 = 200$ μs. This film possesses the same m-HfO_2 structure but a different film microstructure exhibiting: (i) a significant increase in the interlayer thickness from 10 nm to ~55 nm (average value); (ii) slight reduction of the nano-columnar structure width from ~46 to ~38 nm; and (iii) texture with the $(\bar{1}11)$ either parallel or perpendicular to the film surface, Figs. 3 and 5(e). The nano-columnar structures in film T200S18 were also interlocking directly without formation of amorphous boundaries. The T200S18 film has almost the same hardness and modulus as T200S54 but a lower $k_{550} = 0.3 \times 10^{-3}$ and $n_{550} = 2.07$ value (Table 1). Thus, reducing $\langle S_d \rangle$ at $t_1 = 200$ μs, refines the microstructure and develops texture.

3.3.2. Films T200S7 and T100S7

The microstructure of these films is presented by the plan-view TEM images shown in Fig. 8(a) and (b). The grains in these films are separated by distinct boundaries instead of atomically thin boundaries. After

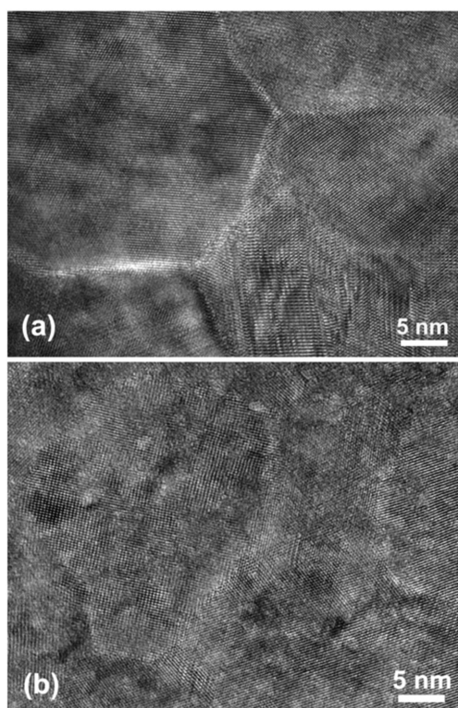

Fig. 6. (a), (b) Plan-view HRTEM image of T200S54 and T200S18 film, respectively.

examining a large number of grains, the average size for film T200S7 and T100S7 was ~24 nm and ~21 nm, respectively. More details of the grain structure is shown by the HRTEM images in Fig. 9. Well defined and low density boundaries with a thickness of ~1 nm are evident in the grain structure. SAED pattern analysis from the T200S7 film, revealed the same m-HfO_2 structure as in the films T200S54 and T200S18. Fig. 8(c) is a SAED pattern taken from a plan-view TEM foil of the T100S7 film. Some differences can be observed in this pattern compared to those shown in Fig. 4(c) and (d). The lattice spacing of the diffraction rings 1, 2, 3, 5, 6, 7 and 8 measured from Fig. 8(c) is 5.10 Å, 3.64 Å, 3.15 Å, 2.56 Å, 2.22 Å, 2.04 Å and 1.82 Å, respectively. The most intense diffraction ring 4 is actually composed of two sub-rings with a *d*-spacing of 2.96 Å (inner ring, 4a) and 2.83 Å (outer ring, 4b). The diffractions rings in Fig. 8(c) cannot be indexed by a single phase. Comprehensive studies of SAED patterns show that the T100S7 film possesses both monoclinic and orthorhombic HfO_2 phases. Fig. 8(d) depicts a comparison of the SAED patterns taken from the T200S7 (left) and T100S7 (right) film. A list of the *d*-spacing measured from the SAED patterns of the four films and the relevant data of the m-HfO_2 (PDF#: 01-075-6426) and o-HfO_2 (PDF#: 01-070-2832) is given in Table 2. All diffraction rings for the T200S7 film (left of Fig. 8(d)) can be indexed by m-HfO_2. Diffraction rings 1, 2, 3, 4b, 5, 7, 8 for the T100S7 film (right of Fig. 8(d)) can be indexed by m-HfO_2, while diffraction rings 1, 2, 4a, 5, 6, 7, 8 can be indexed by o-HfO_2. In other words, diffraction rings 1, 2, 5, 7, 8 are common for both m-HfO_2 and o-HfO_2, while rings 3 and 4b uniquely belong to m-HfO_2 phase, and rings 4a and 6 belong to o-HfO_2. The indices of the diffraction rings are listed in Table 2. The above analysis clarifies the nature of the broad XRD peaks observed for this film, Fig. 3.

Fig. 10(a) and (b) are cross-section TEM images showing the presence of a columnar structure in these films away from the Si substrate similar to the previous two films. Fig. 10(c) and (d) are SAED patterns taken from film T200S7 and T100S7, respectively, presenting strong inhomogeneous intensity distribution along the diffraction rings indicative of texture formation. The line profiles along the vertical direction passing through the center of the SAED (i.e. film growth direction) in Fig. 10(c) and (d) show diffractions similar to the XRD patterns of the T200S7 and T100S7 film, respectively. For example, the diffraction

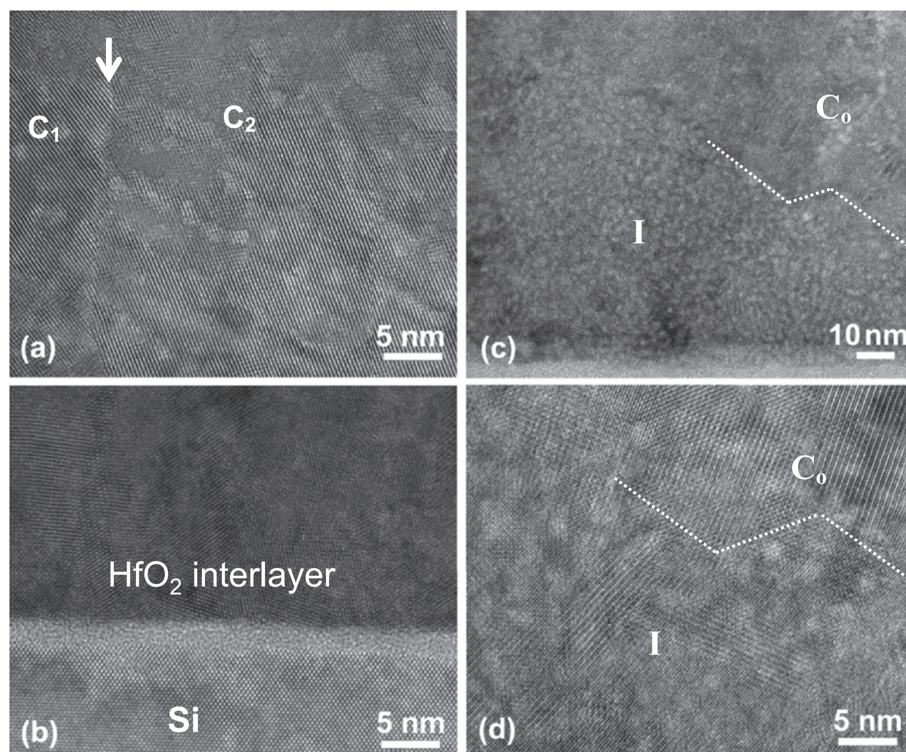

Fig. 7. (a), (b) Cross-section HRTEM image of the HfO_2 film and film/Si interface in T200S54, respectively. (c) Magnified cross-section TEM and (d) HRTEM image of the interface between the HfO_2 columnar structure and the interlayer in T200S18.

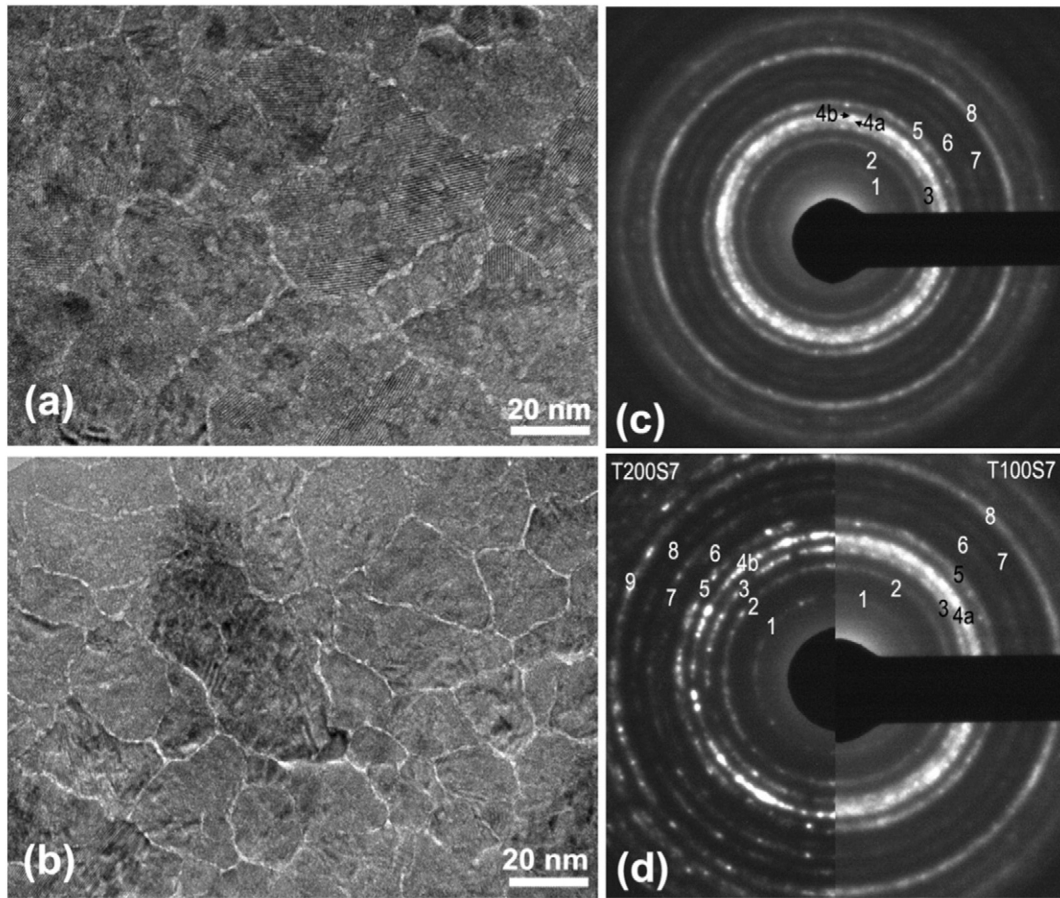

Fig. 8. (a), (b) Plan-view TEM image for T200S7 and (b) T100S7, respectively. (c) SAED pattern of the T100S7 film in a plan-view TEM foil. (d) Comparison of SAED pattern for the T200S7 and T100S7 film.

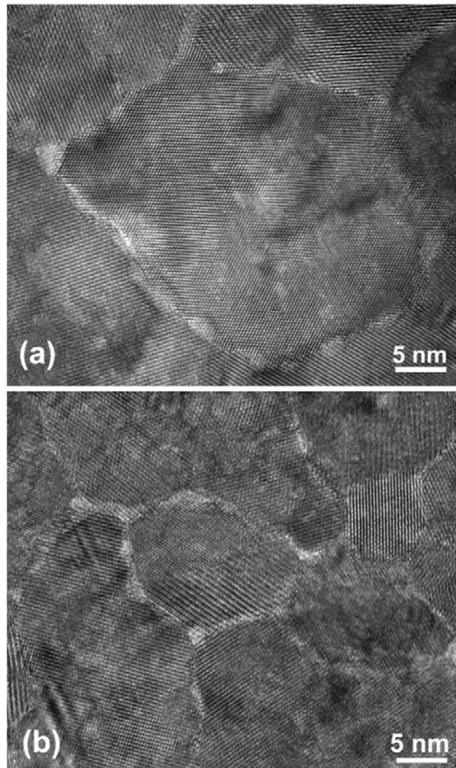

Fig. 9. Plan-view HRTEM image for (a) T200S7 and (b) T100S7 film.

rings ***a***, ***b***, ***c*** and ***d*** in Fig. 10(c) correspond to (110), ($\bar{1}$11), (111) and (002) of m-HfO_2. Diffraction rings ***b*** and ***d*** show much stronger intensity than ***a*** and ***c*** at the intersection with the vertical dash line, in a good agreement with the XRD of the T200S7 film. Similarly, the intersection of ring ***c*** with the vertical line in Fig. 10(d) depicts higher intensity than that of ***a*** and ***d***, but lower than that of ***b***, in a good agreement with the XRD of the T100S7 film. Fig. 10(e) and (f) show the interlayer structure between the Si substrate and the columnar structure in film T200S7 and T100S7, respectively. Both interlayers show a continuous homogenous structure and a hilly interface with respect to the

Table 2
List of the *d*-spacing of the m-HfO_2, o-HfO_2, and the measured values from the SAED patterns of the T200S54, T200S18, T200S7 and T100S7.

m-HfO_2		T200S54/T200S18		T200S7		T100S7		o-HfO_2	
h k l	*d* (Å)	Diff. ring	*d* (Å)	Diff. ring	*d* (Å)	Diff. ring	*d* (Å)	*d* (Å)	h k l
1 0 0	5.050	1	5.02	1	5.02	1	5.10	5.007	1 0 0
0 1 1	3.676	2	3.71						
1 1 0	3.612			2	3.62	2	3.64	3.616	1 1 0
$\bar{1}$ 1 1	3.146	3	3.15	3	3.10	3	3.15		
						4a	**2.96**	2.942	1 1 1
1 1 1	2.825	4	2.83	4	2.79	4b	2.83		
0 2 0	2.584	5	2.59	5	2.55	5	2.56	2.529	0 0 2
0 1 2	2.332	6	2.33	6	2.31				
						6	**2.22**	2.258	2 1 0/1 0 2
$\bar{1}$ 2 1	2.165	7	2.18	7	2.16				
1 2 1	2.052	8	2.03			7	2.04	2.062	2 1 1
1 1 2	2.012			8	2.01				
$\bar{1}$ 2 2	1.793			9	1.79	8	1.82	1.818	0 2 2

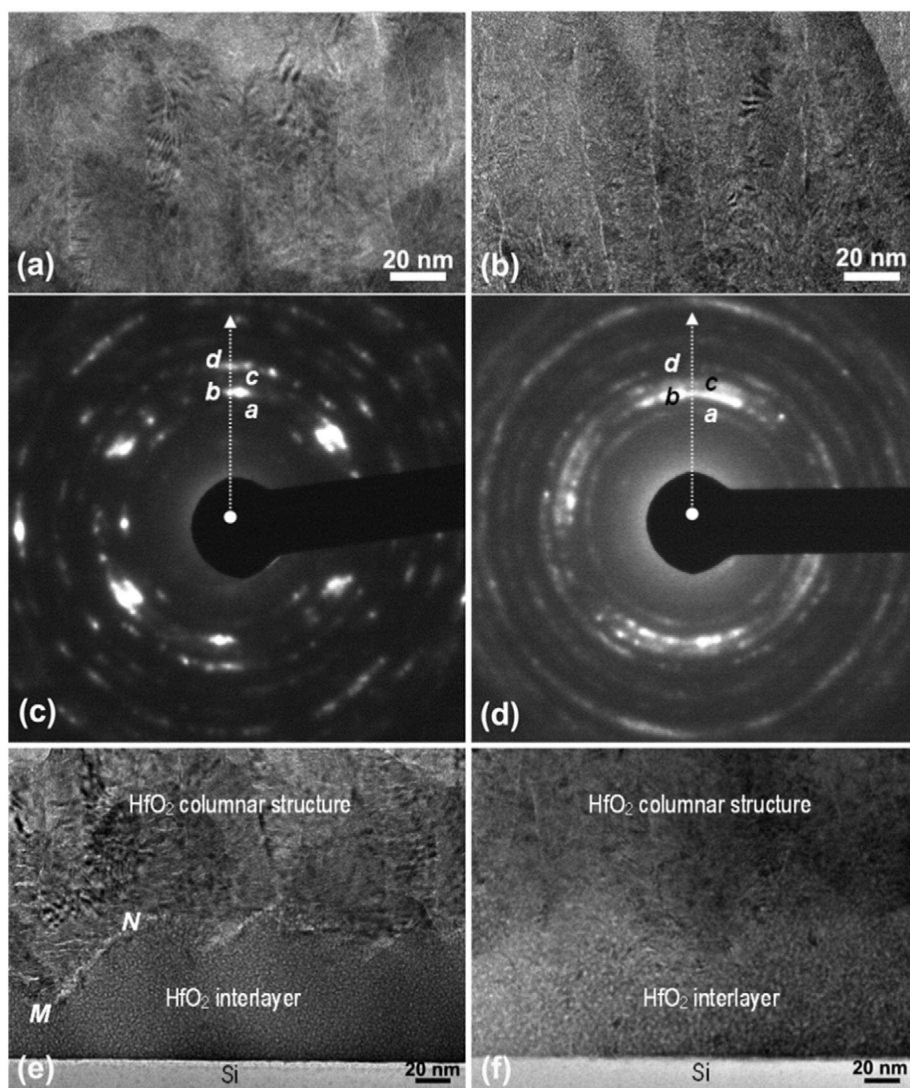

Fig. 10. (a, c) and (b, d) Cross-section TEM image and SAED pattern of the HfO_2 film from T200S7 and T100S7, respectively. (e) and (f) TEM image of the film/Si interface for T200S7 and T100S7, respectively.

columnar structure. Both interlayers possess a similar thickness with an average value of ~60 nm.

Fig. 11(a) is a cross-section HRTEM image of the T200S7 film presenting columnar structures and well defined boundaries. The lattices within or around the two regions marked by "*" are either highly distorted or disordered. The spots marked by "x" correspond to point defects that were likely produced by dislocations. Fig. 11(b) is a cross-section HRTEM image of the T200S7 film showing atomic structure near the interface (white dot line) between the HfO_2 interlayer and columnar structure layer. Similar to the previous films, a high population of lower density nanoscale regions were observed in the interlayer, while their number was drastically reduced in the columnar region. Fig. 11(c) is a HRTEM image of the interlayer/columnar structure boundary marked as ***M***–***N*** in Fig. 10(e). The interface appears brighter while the lattice fringes in the columnar structure extended to the interlayer region without interruption after crossing the interface. Such contrast difference between the interface and surrounding structures is due to the mass variation of the sample indicating the lower density present at the interface. Fig. 11(d) is a HRTEM image of the interface between the HfO_2 interlayer and Si substrate in T100S7 film. Similar to the previous films, the HfO_2 interlayer is composed of a distribution of lower density nanoscale regions with a size of several nm up to 10 nm.

It is noted that a further reduction of $<S_d>$ from 54 (T200S54) and 18 Wcm^{-2} (T200S18) to 7.3 Wcm^{-2} at the same $t_1 = 200$ μs still produces a m-HfO_2 structure in T200S7 film and a similar film microstructure to that in T200S18 film. The trend observed previously continues with (i) the average interlayer thickness increasing to ~60 nm, (ii) the microstructure refinement exhibiting a columnar width of ~24 nm, (iii) a m-HfO_2 preferred orientation with the ($\bar{1}$11) and (002) parallel to the film surface, Figs. 3 and 10(c), and (iv) lower $n_{550} = 2.02$ and slightly lower $k_{550} = 0.2 \times 10^{-3}$. However, the boundaries between the nano-columnar structures in T200S7 were relatively thick with an average size of ~1 nm. Additionally, the boundaries contained several lower density regions, Figs. 8(a) and 9(a). The T200S7 film has nearly the same H and E^* as film T200S18, Table 1.

Film T100S7 prepared with a similar $<S_d> = 7.2$ Wcm^{-2} but reduced $t_1 = 100$ μs possesses a monoclinic as well as orthorhombic HfO_2 structure. This film has an average interlayer thickness of ~60 nm. The nano-columnar structures have an average width of ~21 nm with thick boundaries similar to those in the T200S7 film and an average thickness of ~1 nm. The boundaries also contain lower density regions, Fig. 9(b). The m-HfO_2 crystals show a preferred orientation with the ($\bar{1}$11) parallel to the film surface, Figs. 3 and 10(d), where the orientation of the o-HfO_2 crystalline is random. The T100S7 film has

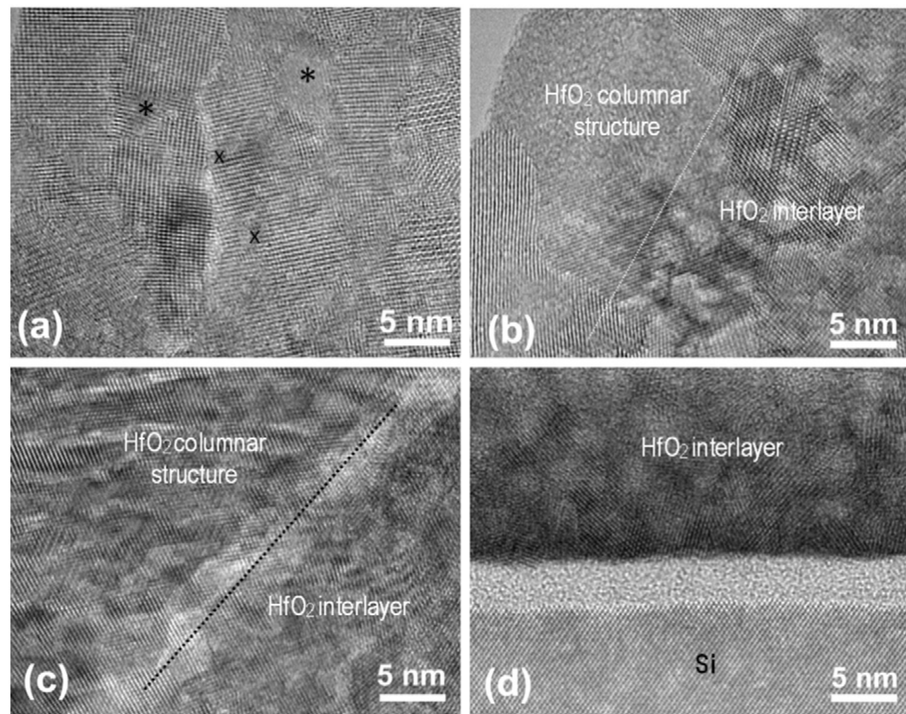

Fig. 11. (a) Cross-section HRTEM image of the HfO_2 film in T200S7. (b) and (c) HRTEM image of the interface between HfO_2 columnar structure and HfO_2 interlayer in T200S7. (d) HRTEM image of the interface between the HfO_2 interlayer and Si in T100S7.

nearly the same k_{550} and n_{550} as the T200S7 film but exhibits a reduction in $H = 13.4$ GPa and $E^* = 162.0$ GPa, Table 1. The aforementioned results suggest that a long t_1 promotes formation of m-HfO_2 while shorter t_1 promotes formation of o-HfO_2. This structural change from m-HfO_2 to o-HfO_2 is associated with the observed reduction in H and E^* in the films. Such effects are in agreement with previous observations [23,24].

3.4. Effect of deposition parameters on the HfO_2 film microstructure and properties

The observed microstructures in the four HfO_2 films prepared by varying t_1 from 100 μs to 200 μs and $<S_d>$ from 7.2 Wcm^{-2} to 54 Wcm^{-2} provide a valuable insight into understanding the relationship between the deposition parameters, microstructure and film properties. All four HfO_2 films have nearly the same thickness of ~1 μm and are composed of an interlayer right above the Si substrate followed by a nano-columnar structure layer. A distribution of lower density nanoscale regions was observed in all four films and their number was significantly higher in the interlayer than in the columnar structure.

The HfO_2 crystal structure and its grain orientation within the film, the size of the nano-columnar structure and the thickness of the interlayer were found to be strongly affected by the deposition parameters t_1 and $<S_d>$. The effects of the variation of deposition parameters t_1 and $<S_d>$ on the nano-columnar structure size are depicted in Fig. 12(a). As noted earlier, $<S_d>$ seems to play a predominant role. In particular, decreasing $<S_d>$ while t_1 remains constant (films T200S54, T200S18, T200S7), reduces the lateral size of the nano-columnar structures in the films, Fig. 12(a). Even though higher $<S_d>$ is not expected to lead to significantly higher energy delivered into the growing films per deposited particle (see the close relationship between $<S_d>$ and a_D in Table 1), it has two important effects. First, it leads to higher growth temperature (increasing during the deposition) up to 155, 130 and 80–90 °C for $<S_d> = 54$, 18 and 7 Wcm^{-2}, respectively. The consequently higher mobility of film atoms can naturally increase the column width (46, 38 and 21–24 nm for $<S_d> = 54$, 18 and 7 Wcm^{-2}, respectively). Second, it leads to higher energy of some of the particles bombarding the growing films (stronger high-energy tail [20]). The energetic bombardment may, for example, destroy (amorphize) some of the crystals soon after their nucleation (see e. g. [25]), opening a larger space for the growth of the remaining ones. In parallel, shorter t_1 leads to a "less effective" utilization of the same $<S_d>$ (e.g. the higher degree of ionization leads to a higher fraction of sputtered Hf atoms attracted back to the target [18], see also lower a_D in Table 1). The consequently lower energy delivered into growing films and lower growth temperature (up to 90 °C for T200S7 and up to 80 °C for T100S7) leads to a further slight but measurable reduction of column size (24 nm in T200S7 and 21 nm in T100S7). The combined effect is presented in Fig. 12(b) which shows an almost linear relationship between $(t_1<S_d>)^{1/2}$ and column width. In parallel to the aforementioned qualitative phenomena, the exponent is quantitatively consistent with the horizontal distance traveled (area affected) by arriving particles (particularly those from the $<S_d>$-dependent high-energy tail) during the pulse: the dependence on $t_1^{1/2}$ is the well-known relationship valid for a random walk, and the dependence on $<S_d>^{1/2}$ yields a linear dependence on what can be a measure of the particle velocity. The easier growth of wide columns at better kinetic conditions is also consistent with the fact that their growth starts sooner (not only in time units but also in terms of deposited monolayers), note the thinnest interlayer (10 nm) in the sample prepared with the highest $<S_d> = 54$ Wcm^{-2}.

Fig. 13 presents the variation of n_{550} vs the lateral size of the nano-columnar structure and interlayer thickness. A general trend is shown where the decrease of the lateral columnar size is accompanied by a somewhat lower n_{550}. This property relates to the film density and the observed trend is attributed to the increase of the volume fraction of low-density boundaries as the columnar size decreases. Films T200S7 and T100S7 exhibited thick, low density boundaries. On the contrary, films T200S54 and T200S18 exhibited higher density with atomically tight and interlocking boundaries resulting in high n_{550} values (2.11 and 2.07). Refractive indices reported for HfO_2 previously are either similar ($n_{550} \leq 2.09$ [26], $n_{1000} = 2.05$ [16], $n_{550} \leq 2.02$ and 2.1 [14]) or even significantly lower ($n_{550} \leq 1.94$ [6,27], $n_{550} = 1.90$ [8], $n_{550} \leq 1.89$ [28]). In parallel to the thickness-averaged refractive indices presented

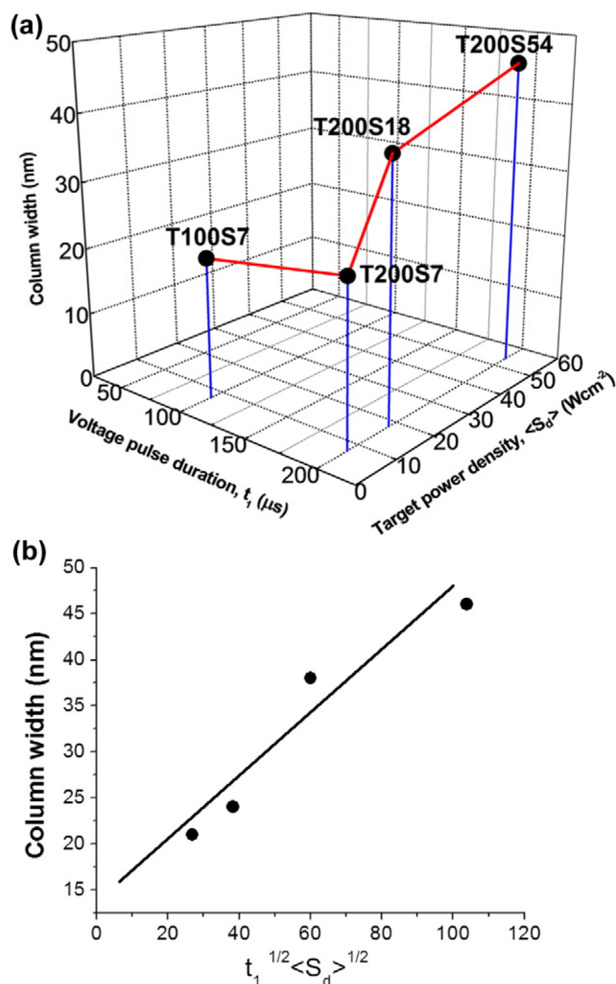

Fig. 12. (a) Variation of column width in the HfO_2 thin films as a function of voltage pulse duration, t_1, and target power density, $<S_d>$. (b) Variation of column width with $(t_1<S_d>)^{1/2}$.

above, the aforementioned higher concentration of low-density regions in the interlayers can be quantified by lower refractive indices of the interlayers (second of the two optical models presented in Section 2.2). The difference between the thickness-averaged n_{550} and the interlayer n_{550} is 2.02–1.94 = 0.08 for the film T100S7, 2.02–1.96 = 0.06 for the film T200S7, 2.07–2.02 = 0.05 for the film T200S18, and not measurable (see also the low interlayer thickness) for the film T200S54.

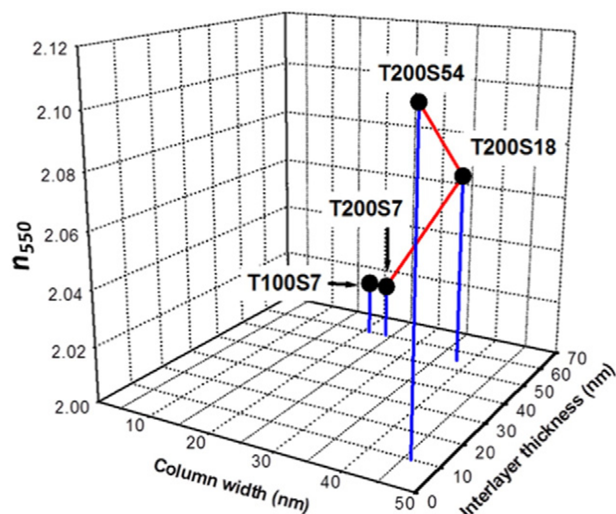

Fig. 13. Variation of n_{550} with column width and interlayer thickness.

The TEM figures show that (except the lower density of the interlayers) all presented films are vertically homogeneous. Note that in parallel to the TEM, this statement is also supported by the low $k_{550} \leq 10^{-3}$. Compositional inhomogeneities would lead to a mixture of stoichiometric HfO_2 with a low k_{550} and substoichiometric HfO_{2-x} with an enhanced k_{550}, and, consequently, the averaged extinction coefficient would be enhanced as well.

The high n_{550} up to 2.11 is important from two points of view: (i) in itself, for some of the applications mentioned in Section 1 (leading to a high optical contrast with the air or low-n materials such as SiO_2) and (ii) as a fingerprint of film densification (which in turn affects other functional properties such as the dielectric constant). Note that in parallel to the high refractive index, the densification of the films T200S54 and T200S18 (except the interlayers) is confirmed also by their mechanical properties. $E^* = 176.5$–176.8 GPa is consistent with e.g. 164.8 GPa (that of the films reported in Ref. [29] which has m-HfO_2 structure), 163–165 GPa (as-deposited films in Ref. [30]) or 177–197 GPa (films annealed up to 700–900 °C in Ref. [30]). In parallel, $H = 17.5$–17.6 GPa is even higher than 14.8 GPa (m-HfO_2 film in Ref. [29]), 8.3–9.7 GPa (as-deposited films in Ref. [30]) or 12.9–14.4 GPa (annealed films in Ref. [30]).

In addition, let us recall that all films showed very low values of $k_{550} \leq 1 \times 10^{-3}$ (property related to the film stoichiometry). Table 1 shows that the optical quality of the films is higher as $<S_d>$ decreases from 54 Wcm^{-2} to lower levels. It is interesting to note that the values of $k_{550} \leq 1 \times 10^{-3}$ obtained in this work for HfO_2 films are lower than those obtained ($k_{550} \leq 6 \times 10^{-3}$) for isostructural ZrO_2 prepared by the same technique [19]. The same trend has also been reported for k_{350} in Ref. [16].

4. Conclusions

Reactive high-power impulse magnetron sputtering with a pulsed reactive gas (oxygen) flow control was used to deposit HfO_2 films on Si substrates. The effect of the voltage pulse duration, t_1, and deposition-averaged target power density, $<S_d>$, on their microstructure was studied by high-resolution transmission electron microscopy. Four HfO_2 films were prepared with (1) T100S7: $t_1 = 100$ μs, $<S_d> = 7.2$ Wcm^{-2}; (2) T200S7: $t_1 = 200$ μs, $<S_d> = 7.3$ Wcm^{-2}; (3) T200S18: $t_1 = 200$ μs, $<S_d> = 18$ Wcm^{-2} and (4) T200S54: $t_1 = 200$ μs, $<S_d> = 54$ Wcm^{-2}. All films were composed of an interlayer with the Si substrate followed by a nano-columnar structure layer. Thus, the results show that the reactive gas flow control can be used to deposit vertically homogeneous films (without any multilayered structure which could hypothetically result from the O_2 flow pulsing). Decreasing $<S_d>$ and t_1, was found to reduce the width of the columns, increase the thickness of the grain boundaries and thickness of the interlayer. Films prepared with a large t_1 (T200S54, T200S18 and T200S7) exhibited a m-HfO_2 structure, while that with a smaller t_1 (T100S7) exhibited a mixture of m- and o-HfO_2 phases. The hardness of films was 13.4–17.6 GPa with those of a monoclinic structure possessing the highest hardness (17.0–17.6 GPa). The films exhibited a refractive index of 2.02–2.11 and an extinction coefficient between 0.1×10^{-3} and 1×10^{-3} (both at a wavelength of 550 nm). The highest refractive index was achieved for films T200S54 and T200S18 that exhibited denser microstructures with atomically sharp and tightly interlocking grain boundaries.

Acknowledgements

This work was supported by the U.S. National Science Foundation under Award NSF/CMMI DMREF-1335502 and by the Grant Agency of the Czech Republic under Project No. GA14-03875S.

References

[1] J. Wang, H.P. Li, R. Stevens, Hafnia and hafnia-toughened ceramics, J. Mater. Sci. 27 (1992) 5397–5430.
[2] K. Matsumoto, Y. Itoh, T. Kameda, EB-PVD process and thermal properties of hafnia-based thermal barrier coating, Sci. Technol. Adv. Mater. 4 (2003) 153–158.
[3] J. Singh, D.E. Wolfe, R.A. Miller, J.I. Eldridge, D.M. Zhu, Tailored microstructure of zirconia and hafnia-based thermal barrier coatings with low thermal conductivity and high hemispherical reflectance by EB-PVD, J. Mater. Sci. 39 (2004) 1975–1985.
[4] A.J. Waldorf, J.A. Dobrowolski, B.T. Sullivan, L.M. Plante, Optical coatings deposited by reactive ion plating, Appl. Opt. 32 (1993) 5583–5593.
[5] M. Fadel, O.A. Azim M., O.A. Omer, R.R. Basily, A study of some optical properties of hafnium dioxide (HfO_2) thin films and their applications, Appl. Phys. A Mater. Sci. Process. 66 (1998) 335–343.
[6] J. Ni, Y. Zhu, S. Wang, Z. Li, Z. Zhang, B. Wei, Nanostructuring HfO_2 thin films as antireflection coatings, J. Am. Ceram. Soc. 92 (2009) 3077–3080.
[7] P. Torchio, A. Gatto, M. Alvisi, G. Albrand, N. Kaiser, C. Amra, High-reflectivity HfO_2/SiO_2 ultraviolet mirrors, Appl. Opt. 41 (2002) 3256–3261.
[8] M.F. Al-Kuhaili, Optical properties of hafnium oxide thin films and their application in energy-efficient windows, Opt. Mater. 27 (2004) 383–387.
[9] V. Pervak, F. Krausz, A. Apolonski, Hafnium oxide thin films deposited by reactive middle-frequency dual-magnetron sputtering, Thin Solid Films 515 (2007) 7984–7989.
[10] J.H. Choi, Y. Mao, J.P. Chang, Development of hafnium based high-k materials - a review, Mater. Sci. Eng. R. Rep. 72 (2011) 97–136.
[11] R.K. Jain, Y.K. Gautam, V. Dave, A.K. Chawla, R. Chandra, A study on structural, optical and hydrophobic properties of oblique angle sputter deposited HfO_2 films, Appl. Surf. Sci. 283 (2013) 332–338.
[12] K. Sarakinos, D. Music, S. Mráz, M. To Baben, K. Jiang, F. Nahif, A. Braun, C. Zilkens, S. Konstantinidis, F. Renaux, D. Cossement, F. Munnik, J.M. Schneider, On the phase formation of sputtered hafnium oxide and oxynitride films, J. Appl. Phys. 108 (2010) 014904.
[13] G. Aygun, A. Cantas, Y. Simsek, R. Turan, Effects of physical growth conditions on the structural and optical properties of sputtered grown thin HfO_2 films, Thin Solid Films 519 (2011) 5820–5825.
[14] T.J. Bright, J.I. Watjen, Z.M. Zhang, C. Muratore, A.A. Voevodin, Optical properties of HfO_2 thin films deposited by magnetron sputtering: From the visible to the far-infrared, Thin Solid Films 520 (2012) 6793–6802.
[15] M. Szymanska, S. Gieraltowska, L. Wachnicki, M. Grobelny, K. Makowska, R. Mroczynski, Effect of reactive magnetron sputtering parameters on structural and electrical properties of hafnium oxide thin films, Appl. Surf. Sci. 301 (2014) 28–33.
[16] M. Audronis, A. Matthews, K. Juškevičius, R. Drazdys, Unlocking the potential of voltage control for high rate zirconium and hafnium oxide deposition by reactive magnetron sputtering, Vacuum 107 (2014) 159–163.
[17] R. Ganesan, B.J. Murdoch, B. Treverrow, A.E. Ross, I.S. Falconer, A. Kondyurin, D.G. Mc Culloch, J.G. Partridge, D.R. Mc Kenzie, M.M.M. Bilek, The role of pulse length in target poisoning during reactive HiPIMS: application to amorphous HfO_2, Plasma Sources Sci. Technol. 24 (2015) 035015.
[18] J. Vlček, A. Belosludtsev, J. Rezek, J. Houška, J. Čapek, R. Čerstvý, S. Haviar, High-rate reactive high-power impulse magnetron sputtering of hard and optically transparent HfO_2 films, Surf. Coat. Technol. 290 (2016) 58–64.
[19] J. Vlček, J. Rezek, J. Houška, R. Čerstvý, R. Bugyi, Process stabilization and a significant enhancement of the deposition rate in reactive high-power impulse magnetron sputtering of ZrO_2 and Ta_2O_5 films, Surf. Coat. Technol. 236 (2013) 550–556.
[20] J. Vlček, J. Rezek, J. Houška, T. Kozák, J. Kohout, Benefits of the controlled reactive high-power impulse magnetron sputtering of stoichiometric ZrO_2 films, Vacuum 114 (2015) 131–141.
[21] Powder Diffraction File™, ICDD, International Centre for Diffraction Data, Newton Square, PA, USA, 2009 (PDF-2, Release).
[22] J. Wang, H.P. Li, R. Stevens, Review: hafnia and hafnia-toughened ceramics, J. Mater. Sci. 27 (1992) 5397–5430.
[23] M.H. Zhang, J.C. Jiang, E.I. Meletis, P. Mares, J. Houska, J. Vlček, Effect of the Si content on the microstructure of hard, multifunctional Hf-B-Si-C films prepared by pulsed magnetron sputtering, Appl. Surf. Sci. 357 (2015) 1343–1354.
[24] M.H. Zhang, J.C. Jiang, J. Vlček, P. Steidl, J. Kohout, R. Cerstvy, E.I. Meletis, A study of the microstructure evolution of hard Zr–B–C–N films by high-resolution transmission electron microscopy, Acta Mater. 77 (2014) 212–222.
[25] J. Houska, Quantitative investigation of the role of high-energy particles in Al_2O_3 thin film growth: a molecular-dynamics study, Surf. Coat. Technol. 254 (2014) 131–137.
[26] M. Vargas, N.R. Murphy, C.V. Ramana, Structure and optical properties of nanocrystalline hafnium oxide thin films, Opt. Mater. 37 (2014) 621–628.
[27] V. Dave, H.O. Gupta, R. Chandra, Nanostructured hydrophobic DC sputtered inorganic oxide coating for outdoor glass insulators, Appl. Surf. Sci. 295 (2014) 231–239.
[28] J.M. Khoshman, M.E. Kordesch, Optical properties of a-HfO_2 thin films, Surf. Coat. Technol. 201 (2006) 3530–3535.
[29] A.L.M. Vargas, F. de Araújo Ribeiro, R. Hübler, Changes in the Young modulus of hafnium oxide thin films, Nucl. Instrum. Meth. B 365 (2016) 362–366.
[30] M. Berdova, X. Liu, C. Wiemer, A. Lamperti, G. Tallarida, E. Cianci, M. Fanciulli, S. Franssila, Hardness, elastic modulus, and wear resistance of hafnium oxide-based films grown by atomic layer deposition, J. Vac. Sci. Technol. A 34 (2016) 051510.

C. Thickness dependent wetting properties and surface free energy of HfO_2 thin films

S. Zenkin, A. Belosludtsev, Š. Kos, R. Čerstvý, S. Haviar, M. Netrvalová

Appl. Phys. Lett. 108 (2016) 231602

Thickness dependent wetting properties and surface free energy of HfO_2 thin films

Sergei Zenkin,[1,a)] Alexandr Belosludtsev,[1] Šimon Kos,[1] Radomír Čerstvý,[1] Stanislav Haviar,[1] and Marie Netrvalová[2]
[1]*Department of Physics and NTIS-European Centre of Excellence, Faculty of Applied Sciences, University of West Bohemia, Univerzitní 8, CZ-306 14 Plzeň, Czech Republic*
[2]*New Technologies-Research Centre, University of West Bohemia, Univerzitní 8, CZ-306 14 Plzeň, Czech Republic*

(Received 9 March 2016; accepted 24 May 2016; published online 6 June 2016)

We show here that intrinsic hydrophobicity of HfO_2 thin films can be easily tuned by the variation of film thickness. We used the reactive high-power impulse magnetron sputtering for preparation of high-quality HfO_2 films with smooth topography and well-controlled thickness. Results show a strong dependence of wetting properties on the thickness of the film in the range of 50–250 nm due to the dominance of the electrostatic Lifshitz-van der Waals component of the surface free energy. We have found the water droplet contact angle ranging from $\approx 120^{\circ}$ for the thickness of 50 nm to $\approx 100^{\circ}$ for the thickness of 2300 nm. At the same time the surface free energy grows from $\approx 25\,mJ/m^2$ for the thickness of 50 nm to $\approx 33\,mJ/m^2$ for the thickness of 2300 nm. We propose two explanations for the observed thickness dependence of the wetting properties: influence of the non-dominant texture and/or non-monotonic size dependence of the particle surface energy. *Published by AIP Publishing.*
[http://dx.doi.org/10.1063/1.4953262]

There has been a considerable effort to develop hydrophobic ceramics that would combine high hardness, excellent thermal stability, and wear resistance with values of water droplet contact angle (WDCA) close to those for organic and fluoro-polymers. This combination is desirable for robust hydrophobic surfaces in harsh-environment applications such as dropwise condensation heat transfer[1,2] or stable anti-ice protective coatings.[3] In these applications polymers do not have the required thermal properties and surface patterning giving rise to (super)hydrophobicity[4,5] would be destroyed mechanically, so hydrophobicity intrinsic to the ceramic is required. Recently, Azimi *et al.* reported their finding that lanthanide oxides are intrinsically hydrophobic ceramics.[6] The authors attribute the intrinsic hydrophobicity to the screening of the incompletely filled 4f shell characteristic for the lanthanides, which leads to a reduced interaction between water molecules and the oxide surface. However, in our subsequent work,[7] we suggested that the underlying principle at work here is the low electronegativity of the metal cation irrespective of whether it was achieved by the screening of 4f electrons or by some other mechanism. Indeed, we found there that other low-electronegativity metals such as magnesium from the main group and zirconium, yttrium, or hafnium from the d-block of the periodic table can form hard hydrophobic oxides and nitrides with WDCA comparable with those for lanthanide oxides. These findings were also confirmed by Refs. 8 and 9 for HfO_2 and Ref. 10 for Y_2O_3. Schematically, interactions of water with a high- (molybdenum) and a low- (hafnium) electronegativity metal oxide are shown in Fig. 1. An oxide of molybdenum forms a high number of strong co-ordinate bonds with water molecules in addition to hydrogen bonds between surface oxygen and water hydrogen and exhibits strong wetting by water (see Fig. 1(a)). Conversely, an oxide of hafnium forms only hydrogen bonds with water hydrogen without any strong bonds between surface hafnium and water oxygen giving rise to a reduced wetting by water (see Fig. 1(b)).

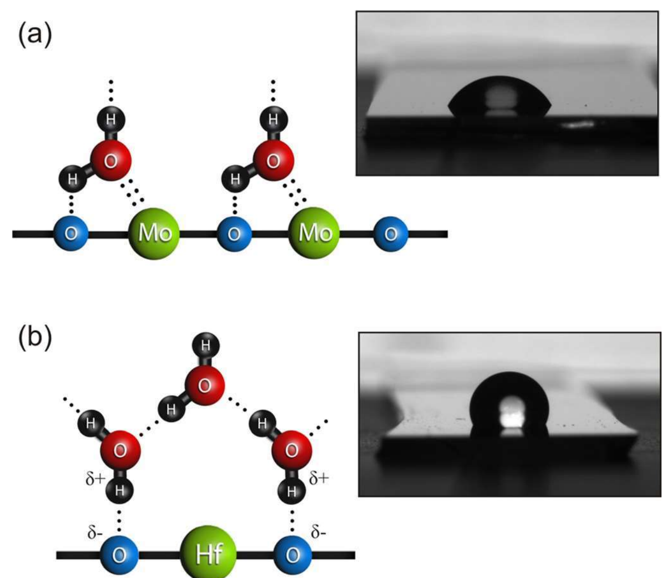

FIG. 1. Schematic illustration of water molecules on a hydrophilic and a hydrophobic surface: (a) a high-electronegativity metal oxide, for example, molybdenum oxide forms a high number of strong coordinate bonds with water oxygen in addition to hydrogen bonds between water hydrogen and surface oxygen and therefore shows a low value of the contact angle with water; (b) a low-electronegativity metal oxide, for example, hafnium dioxide forms only hydrogen bonds between surface oxygen and water hydrogen and exhibits a high value of contact angle with water.

[a)]Author to whom correspondence should be addressed. Electronic mail: zenkin@kfy.zcu.cz

Published by AIP Publishing.

Due to the fact that interactions of water with low-electronegativity metal oxide are ≈99% electrostatic in nature,[6,7] we expect a strong dependence of wetting properties on the thickness of the film. A similar effect has been observed for van der Waals solids such as graphene[11,12] and molybdenum disulfide.[13] Also, size-dependent surface free energy has been reported for TiO_2 nanoparticles.[14] It has the potential to increase WDCA above the intrinsic bulk value by reducing the film thickness. To confirm our prediction, we selected the already insinuated hafnium dioxide as a representative compound of a low-electronegativity metal, which previously was well studied due to its high dielectric constant, high melting point, and transparency.[15] To prepare dense homogeneous stoichiometric HfO_2 films with smooth surfaces and well controlled thickness down to the units of nm, we used the reactive high-power impulse magnetron sputtering (HiPIMS) with a pulsed reactive gas flow control (RGFC). In HiPIMS,[16–19] highly ionized fluxes of particles onto substrates with high fractions of metal ions and enhanced energies with which the ions bombard the substrate surface[20] allow the growth of dense homogeneous oxide films.[16] Specifically HfO_2 thin films have already been prepared by HiPIMS.[21–23] Our RGFC method is able to utilize the exclusive benefits[18] of the HiPIMS discharge to maintain a sputter deposition of stoichiometric robust films.

In the present paper, we report on thickness dependent wetting properties and surface free energy of thin films of HfO_2 as an example material chosen for such a study. Due to the experimental conditions used, we could neglect the effect of other factors that could potentially influence hydrophobic properties of metal ceramics such as surface metal/anion ratio[24] (films were stoichiometric), surface roughness,[4] amount of hydrocarbon impurities[25] (values of contact angles were the same within a few minutes after the deposition and several months later), number of adsorption centers on the surface[26] (Hf is a poor Lewis acid), and sort of the surface anion[7] (oxide only). These factors will be discussed further below.

The films were deposited using a strong unbalanced magnetron source with a directly water-cooled planar hafnium target (99.9% Hf purity, a diameter of 100 mm, and a thickness of 6 mm) in a standard stainless-steel vacuum chamber (a diameter of 507 mm and a length of 520 mm), which was evacuated by a diffusion pump backed up with a rotary pump. The base pressure before deposition was 10^{-3} Pa. The magnetron was driven by a high-power pulsed dc power supply (HMP 2/1, Hüttinger Elektronik). For all films in this work, the repetition frequency was 500 Hz and the voltage pulse duration 200 μs with the corresponding duty cycle 10% and the deposition-averaged target power density was 15 W cm^{-2}. A very high deposition rate of 90 nm/min and further experimental details are discussed in Ref. 21. Depositions were performed using the feed-back pulsed O_2 flow control.[18] The film thickness was controlled by the time of the deposition. The film thickness was measured at the film edge by profilometry (Dektak 8 Stylus Profiler, Veeco) using a 380 μm thick removable Si step, and at various places of the film by variable angle spectroscopic ellipsometry using a J.A. Woollam Co., Inc., instrument. The maximum measurement error of both of these techniques was well below 1%. The position of the film edge at the substrate holder was the same in all the depositions with the center of the film edge 10 mm from the axis. X-ray diffraction (XRD) measurements were carried out at room temperature on a PANalytical X'Per PRO diffractometer working in the Bragg–Brentano geometry using a CuKα (40 kV, 40 mA) radiation. To avoid a strong reflection from the Si (100) substrate, a slightly asymmetrical diffraction geometry with an ω-offset of 1.5° was used. Samples were scanned over the 2θ-range from 8° to 108°. Water spectra were determined by a FTIR Spectrometer NICOLET 380 in conjunction with an attenuated total reflection accessory (ATR). A thin film of water was added to the surface of each HfO_2 film and this combined water-HfO_2 layer was scanned with the depth of penetration 670 nm. The surface morphology of the films was determined by atomic force microscopy (AFM) using a SmartSPM Microscope (AIST-NT) with a silicon tip (nominal radius of 10 nm) in a non-contact mode and Hitachi SU-70 scanning electron microscope (SEM). WDCA, surface free energy of the films and their Lifshitz-van der Waals and acid-base components were measured by using the Drop Shape Analyzer DSA30, KRÜSS GmbH. The wetting properties of the sputtered HfO_2 films were measured by the sessile drop method with the volume of water droplet $V = 2\,\mu$l. For determination of the surface free energy components, we used three testing liquids: deionised water, glycerol, and 1-bromonaphtalene.

HfO_2 films were deposited with various thicknesses from 50 nm to 250 nm with the step of 50 nm. For comparison, a 2300 nm-thick film was deposited and regarded as bulk HfO_2. Fig. 2 shows main differences in XRD patterns, SEM images, and WDCA between 100 nm and 2300 nm-thick HfO_2 films. All films exhibited a nanocrystalline structure with a dominant monoclinic phase (m-HfO_2, Card No. 34–0104 in Ref. 27) with a preferred (−1 1 1) orientation at $2\theta = 27.90°$, with a non-dominant (0 0 2) orientation at $2\theta = 35.53°$ and with asymmetry of the m−HfO_2 (−1 1 1) diffraction peak, indicating a possible presence of a small amount of the tetragonal phase (t-HfO_2, Card No. 8–0342 in Ref. 27) in the films. The left panels of Fig. 2 show XRD patterns for 100 nm and 2300 nm thick HfO_2 films with these features. For both films, the crystal grain sizes were about 5–7 nm. The higher peak intensities in the lower panel are due to the higher film thickness. The SEM images for the same 100 nm and 2300 nm thick HfO_2 films are shown in the middle panels of Fig. 2. All films were smooth and with homogeneous surface topography. The values for the average roughness, measured by AFM, profilometer, and ellipsometry, were practically the same and less than 8 nm for all films. This small value of film roughness gives a negligible effect on the value of the contact angle.[4] For the films of our primary interest with the lowest thickness of 50 nm exhibiting the highest contact angle, the roughness of 5 nm combined with the particle size of 30 nm gives an increase in the true area compared to the apparent area by the factor r estimated by $\sqrt{(15^2+5^2)}/15 \approx 1.05$ giving rise, according to the Wenzel equation $\cos\theta^* = r\,\cos\theta$ with $\theta^* \approx 120°$, to the change of the water droplet contact angle from θ^* to θ of about 1° Also, films of thicknesses from 50 nm to 250 nm were densified as demonstrated by a high value of the refractive index (at the wavelength of 550 nm) of 2.04. In parallel, the very low value of the extinction coefficient (at the wavelength of 550 nm) of not more than $0\,7 \times 10^{-3}$ proved that

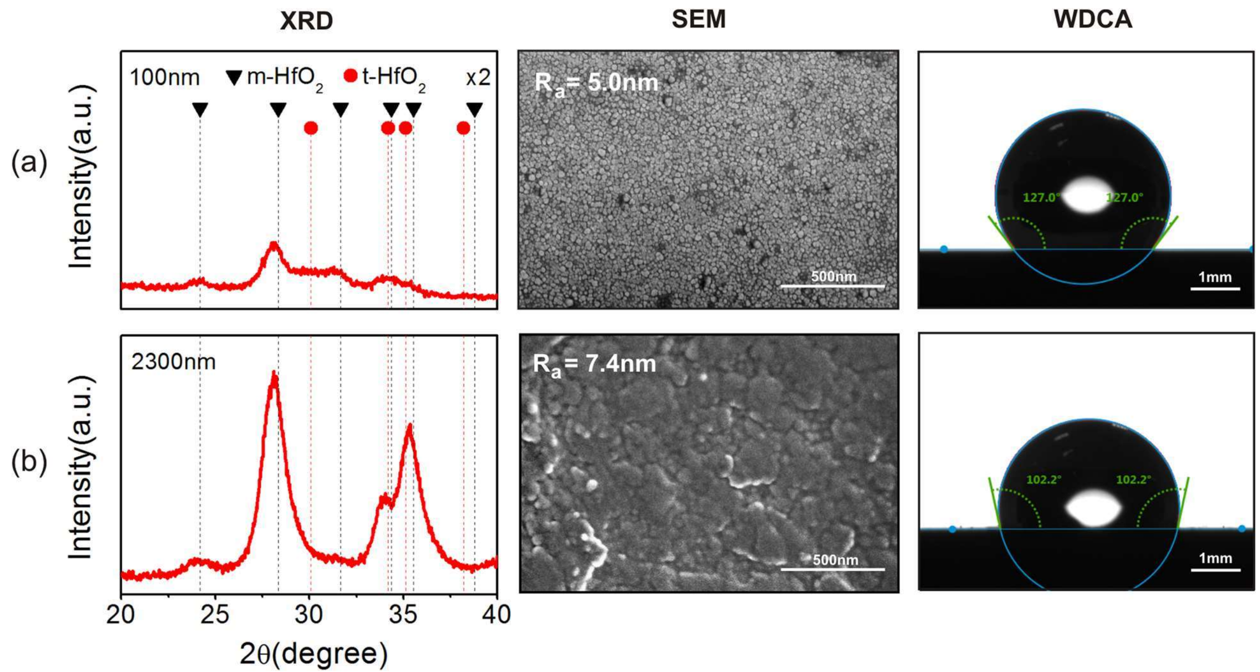

FIG. 2. XRD patterns, SEM images of the surface and images of water droplets with indicated values of WDCA for (a) 100 nm thick film and (b) 2300 nm thick film.

the films were stoichiometric. The values for the bulk material and a detailed review of optical constants for HfO_2 films can be found in Ref. 21. The right panels of Fig. 2 illustrate our main result: WDCA for the 2300 nm thick film $\theta_{2300} \approx 100^\circ$ is significantly lower than that for the 100 nm thick film $\theta_{100} \approx 120^\circ$.

For deeper understanding of the dependence of HfO_2 wetting properties on the thickness of the film, we use the van Oss-Good-Chaudhury equation[28]

$$\gamma_L(1+\cos\theta) = 2\left(\sqrt{\gamma_S^{LW}\gamma_L^{LW}} + \sqrt{\gamma_S^{+}\gamma_L^{-}} + \sqrt{\gamma_S^{-}\gamma_L^{+}}\right).$$

Here, θ is the contact angle with a droplet of liquid L, γ_S^{LW} is the electrostatic Lifshitz-van der Waals component of the surface free energy of the solid film, and γ_S^{+} and γ_S^{-} are, respectively, the polar Lewis acid and the polar Lewis base components giving the polar acid-base component γ_S^{AB} as

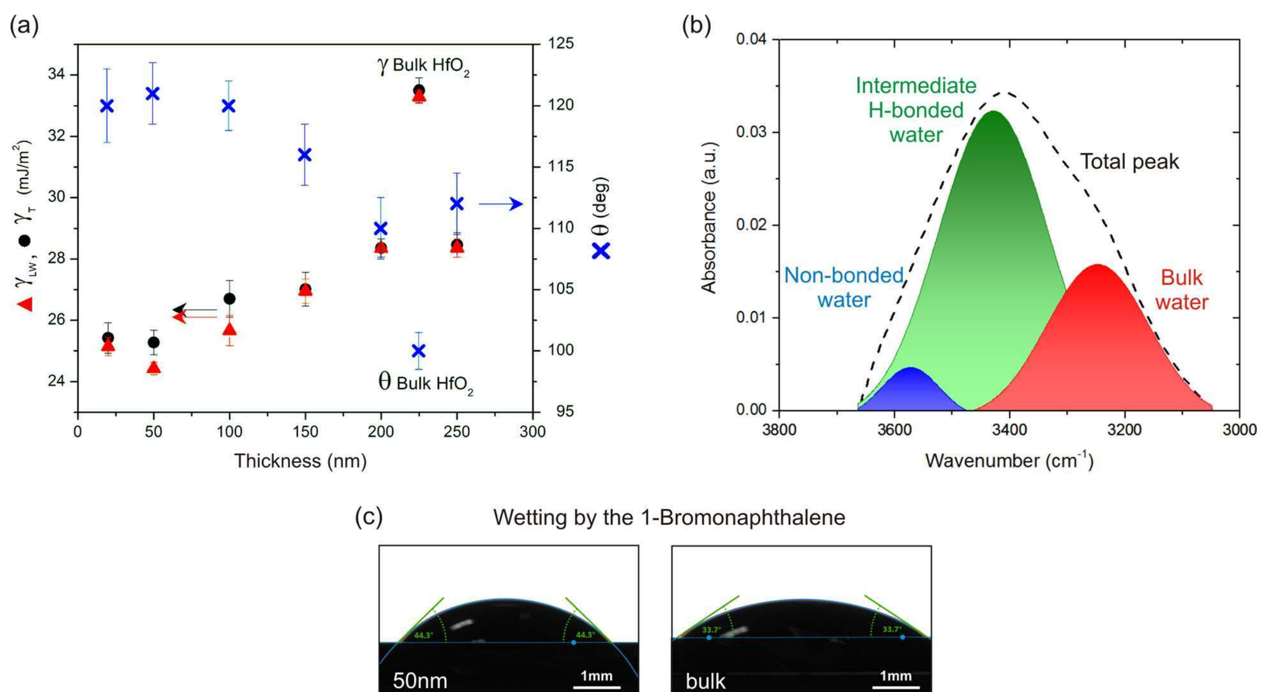

FIG. 3. (a) Dependence of WDCA θ, total surface free energy γ_T, and van der Waals component of surface free energy γ_{LW} on the thickness of the HfO_2 film. (b) FTIR spectrum and its decomposition for water placed on the surface of a 100 nm thick HfO_2 film. (c) Contact angles of 1-bromonaphthalene for a 50 nm-thick film and bulk HfO_2.

$$\gamma_S^{AB} = 2\sqrt{\gamma_S^+ \gamma_S^-}.$$

The total surface free energy of the solid film γ_S is then given as the sum of the electrostatic Lifshitz-van der Waals and the polar acid-base component

$$\gamma_S = \gamma_S^{LW} + \gamma_S^{AB}.$$

The corresponding components of the surface free energy of the droplet forming liquid are denoted with the subscript L. Fig. 3(a) shows that the surface free energy of HfO_2 films decreases with a decreasing thickness of the film. For all films, values of the electrostatic Lifshitz–van der Waals component are close to the values of the total surface free energy. As the total surface free energy decreases from $\gamma_{bulk} \approx 33$ mJ/m^2 for the bulk HfO_2 to $\gamma_{100} \approx 26$ mJ/m^2 for the 100 nm-thick film, WDCA increases correspondingly up to 120°. A decrease in the film thickness below 50 nm does not lead to a further increase in WDCA or to a further decrease in the surface free energy. Orientation of the water molecules on the surface was measured by the FTIR-ATR technique. The normalized FTIR spectrum for the 100 nm film is shown in Fig. 3(b). The total OH-stretching absorption peak of water (dashed line) was divided[6,29,30] into three peaks: the ~3200 cm^{-1} peak attributed to the strongly H-bonded or tetrahedrally coordinated bulk water (red), the ~3400 cm^{-1} peak attributed to an intermediate H-bonding or an incomplete tetrahedral coordination (green) and the ~3600 cm^{-1} peak attributed to non H-bonded or free OH stretching (blue). Both of the latter two peaks are attributed to water molecules close to a hydrophobic surface. The values of the absorbance ratio A_{3400}/A_{3200} (intensity of a surface water peak to intensity of the bulk water peak) for films with thicknesses in the range of 50–250 nm are within a few percent, in the range of 2.05–2.12. It means that wetting properties are qualitatively the same for all the HfO_2 films of different thicknesses with only quantitative differences given by the different values of the surface free energy. With a decreasing film thickness, the Raman signal (not shown) in the interval 2800–3000 cm^{-1} containing C-H modes[31] decreased showing that hydrocarbons are not responsible for the increasing hydrophobicity. The film thickness dependence of the wetting properties is also confirmed by the wetting of 1-bromonaphtalene (Fig. 3(c)). In that case, the increase in the total surface free energy from $\gamma_{50} \approx 25$ mJ/m^2 for the 50 nm thick film to $\gamma_{bulk} \approx 33$ mJ/m^2 for the bulk HfO_2 corresponds to the decrease in the droplet contact angle from $\theta_{50} \approx 43.5°$ to $\theta_{bulk} \approx 34°$.

Thickness dependent wetting behavior of thin films of van der Waals solids like graphene or molybdenum disulfide is observed on the scale of a few atomic layers since the van der Waals surface free energy is given by an integral divergent in its lower limit, and the value of the lower limit is set by the shortest distance between the liquid molecules and the surface comparable to the lattice constants.[12] Due to the fact that thicknesses of our HfO_2 films are on the order of hundreds of atomic layers, we suggest there is a different mechanism of surface energy dependence. Specifically, two possible explanations are:

(1) Influence of the non-dominant texture. An increase in the HfO_2 film thickness is accompanied by an increase in the intensity of the non-dominant (0 0 2) texture of the monoclinic phase. Previous results of calculations of optimized geometries for water molecules adsorbed on the Al-doped ZnO surfaces show different distances between water molecules and the solid with different crystal orientations.[32] Also, there is both experimental[33] and theoretical[34] evidence for the dependence of surface free energy on the crystal orientation in TiN. Therefore, growth of the fraction of the (0 0 2) texture intensity to the preferred orientation (−1 1 1) intensity might lead to increasing of the total surface free energy with an increasing film thickness.
(2) Changing of the particle size in the material. Surface stress and surface free energy have been reported as decreasing,[35,36] increasing,[37] or non-monotonically changing[14] with a decreasing particle size of the material. SEM images of our HfO_2 films show particle sizes in the range of 30–50 nm for the 50–250 nm thick films. In this range of particle sizes, the observed thickness dependence of the surface free energy might therefore indicate a decreasing surface free energy with a decreasing particle size. Yet it is possible that for particle size decreasing further below 30 nm, the surface free energy will start increasing again.

Both effects might be acting in parallel both decreasing the surface free energy and thus increasing the contact angle for a decreasing film thickness from 250 nm down to 50 nm. At a further decrease in the film thickness, the two effects might act against each other, so a surface free energy increase due to a decreasing particle size might be compensated by its decrease due to a smaller influence of the non-dominant texture leading to an approximately constant value of 25 mJ/m^2 and a consequent approximately constant value of WDCA around 120°.

In conclusion, thickness dependent wetting properties were measured for the intrinsically hydrophobic HfO_2 thin films prepared by reactive high power impulse magnetron sputtering. The van Oss-Good-Chaudhury approach used shows that surface free energy of HfO_2 is ≈99% electrostatic in nature for all thicknesses. This dominance of the electrostatic Lifshitz–van der Waals component of the surface energy allows to control the value of the contact angle with water in the range of 100°–120° by the variation of the film thickness in the range 50–250 nm. FTIR-ATR measurements show that the wetting properties are qualitatively the same for all HfO_2 films of different thicknesses. Combining these results with XRD and SEM measurements, we suggest two mechanisms of surface energy thickness dependence: influence of non-dominant texture and/or non-monotonic size dependence of the particle surface energy. Surfaces with controlled wettability might find various applications such as substrates for controlled morphology of spin-coated films.[38]

We thank Jiří Houška for ellipsometry and Raman measurements.

[1]D. J. Preston, D. L. Mafra, N. Miljkovic, J. Kong, and E. N. Wang, Nano Lett. **15**, 2902 (2015).
[2]C. Chen, Q. Cai, C. Tsai, C. Chen, G. Xiong, Y. Yu, and Z. Ren, Appl. Phys. Lett. **90**, 173108 (2007).

[3]P. Kim, T. Wong, J. Alvarenga, M. J. Kreder, W. E. Adorno-Martinez, and J. Aizenberg, ACS Nano **6**, 6569 (2012).
[4]D. Quéré, Annu. Rev. Mater. Res. **38**, 71 (2008).
[5]Y. Lu, S. Sathasivam, J. Song, C. R. Crick, C. J. Carmalt, and I. P. Parkin, Science **347**, 1132 (2015).
[6]G. Azimi, R. Dhiman, H. Kwon, A. T. Paxson, and K. K. Varanasi, Nat. Mater.**12**, 315 (2013).
[7]S. Zenkin, Š. Kos, and J. Musil, J. Am. Ceram. Soc. **97**, 2713 (2014).
[8]R. K. Jain, Y. K. Gautam, V. Dave, A. K. Chawla, and R. Chandra, App. Surf. Sci. **283**, 332 (2013).
[9]S. Lin and C. Liao, App. Surf. Sci. **380**, 229 (2016).
[10]I. Oh, K. Kim, Z. Lee, K. Y. Ko, C. Lee, S. J. Lee, J. M. Myung, L.-C. Matras, W. Noh, C. Dussarrat, H. Kim, and H. Lee, Chem. Mater. **27**, 148 (2015).
[11]J. Rafiee, X. Mi, H. Gullapalli, A. V. Thomas, F. Yavari, Y. Shi, P. M. Ajayan, and N. A. Koratkar, Nat. Mater. **11**, 217 (2012).
[12]C. Shih, Q. H. Wang, S. Lin, K. Park, Z. Jin, M. S. Strano, and D. Blankschtein, Phys. Rev. Lett. **109**, 176101 (2012).
[13]A. P. S. Gaur, S. Sahoo, M. Ahmadi, S. P. Dash, M. J.-F. Guinel, and R. S. Katiyar, Nano Lett. **14**, 4314 (2014).
[14]H. Zhang, B. Chen, and J. F. Banfield, Phys. Chem. Chem. Phys. **11**, 2553 (2009).
[15]J. Robertson, Rep. Prog. Phys. **69**, 327 (2006).
[16]J. T. Gudmundsson, N. Brenning, D. Lundin, and U. Helmersson, J. Vac. Sci. Technol., A **30**, 030801 (2012).
[17]K. Sarakinos, J. Alami, and S. Konstantinidis, Surf. Coat. Technol. **204**, 1661 (2010).
[18]J. Vlček, J. Rezek, J. Houška, T. Kozák, and J. Kohout, Vacuum **114**, 131 (2015).
[19]T. Kozák and J. Vlček, J. Phys. D: Appl. Phys. **49**, 055202 (2016).
[20]P. Kudláček, J. Vlček, K. Burcalová, and J. Lukáš, Plasma Sources Sci. Technol. **17**, 025010 (2008).
[21]J. Vlček, A. Belosludtsev, J. Rezek, J. Houška, J. Čapek, R. Čerstvý, and S. Haviar, Surf. Coat. Technol. **290**, 58 (2016).
[22]R. Ganesan, B. J. Murdoch, B. Treverrow, A. E. Ross, I. S. Falconer, A. Kondyurin, D. G. McCulloch, J. G. Partridge, D. R. McKenzie, and M. M. M. Bilek, Plasma Sources Sci. Technol. **24**, 035015 (2015).
[23]K. Sarakinos, D. Music, S. Mráz, M. To Baben, K. Jiang, F. Nahif, A. Braun, C. Zilkens, S. Konstantinidis, F. Renaux, D. Cossement, F. Munnik, and J. M. Schneider, J. Appl. Phys. **108**, 014904 (2010).
[24]S. Khan, G. Azimi, B. Yildiz, and K. K. Varanasi, Appl. Phys. Lett **106**, 061601 (2015).
[25]D. J. Preston, N. Miljkovic, J. Sack, R. Enright, J. Queeney, and E. N. Wang, Appl. Phys. Lett **105**, 011601 (2014).
[26]H. H. Kung, *Transition Metal Oxides: Surface Chemistry and Catalysis* (Elsevier, The Netherlands, 1989).
[27]International Centre for Diffraction Data, PDF-2 Database Sets 1–47, PA, USA, 1997.
[28]C. J. van Oss, R. J. Good, and M. K. Chaudhury, Langmuir **4**, 884 (1988).
[29]M. R. Yalamanchili, A. A. Atia, and J. D. Miller, Langmuir **12**, 4176 (1996).
[30]L. F. Scatena, M. G. Brown, and G. L. Richmond, Science **292**, 908 (2001).
[31]Z. Li, Y. Wang, A. Kozbial, G. Shenoy, F. Zhou, R. McGinley, P. Ireland, B. Morganstein, A. Kunkel, S. P. Surwade, L. Li, and H. Liu, Nat. Mater. **12**, 925 (2013).
[32]J. Wang, Y. Li, Y. Kong, J. Zhou, J. Wu, X. Wu, W. Qin, Z. Jiao, and L. Jiang, RSC Adv. **5**, 81024 (2015).
[33]U. C. Oh and J. H. Je, J. Appl. Phys. **74**(3), 1692 (1993).
[34]M. Marlo and V. Milman, Phys. Rev. B **62**(4), 2899 (2000).
[35]G. Ouyang, X. Tan, and G. Yang, Phys. Rev. B **74**, 195408 (2006).
[36]Q. Jiang, D. S. Zhao, and M. Zhao, Acta Mater. **49**, 3143 (2001).
[37]E. Muller, W. Vogelsberger, and H.-G. Fritsche, Cryst. Res. Technol. **23**, 1153 (1988).
[38]C. Bi, Q. Wang, Y. Shao, Y. Yuan, Z. Xiao, and J. Huang, Nat. Commun. **6**, 7747 (2015).

D. Structure and properties of Hf-O-N films prepared by high-rate reactive HiPIMS with smoothly controlled composition

A. Belosludtsev, J. Houška, J. Vlček, S. Haviar, R. Čerstvý, J. Rezek, M. Kettner

Ceram. Int. (submitted for publication)

Structure and properties of Hf-O-N films prepared by high-rate reactive HiPIMS with smoothly controlled composition

A. Belosludtsev[a], J. Houška[a]*, J. Vlček[a], S. Haviar[a], R. Čerstvý[a], J. Rezek[a], M. Kettner[b]

[a] *Department of Physics and NTIS - European Centre of Excellence, University of West Bohemia, Univerzitní 8, 306 14 Plzeň, Czech Republic*
[b] *Faculty of Mathematics and Physics, Department of Surface and Plasma Science, Charles University, V Holešovičkách 2, Praha 8, 180 00, Czech Republic*

**corresponding author: phone: +420 377632218, fax: +420 377632202, jhouska@kfy.zcu.cz*

Abstract

Hf-O-N films were prepared by high-power impulse magnetron sputtering of Hf in Ar+O_2+N_2 gas mixtures. Smooth composition control was achieved by maximizing the degree of dissociation in plasma. The application potential of the films was further enhanced by extremely high deposition rates (e.g. 230 nm/min for HfO_2; achieved by feedback pulsed reactive gas flow control), low deposition temperatures (<140 °C) and not using any substrate bias. We focus on the relationships between composition, structure, and optical, electrical, mechanical and hydrophobic properties of the materials. The evolution of smoothly controlled film properties along the transition from an oxide to a nitride includes e.g. extinction coefficient at 550 nm from 5×10^{-4} to 1.77, electrical resistivity from $>10^8$ to 3.2×10^{-6} Ωm, hardness from 18 to 25 GPa or water droplet contact angle from 101° to 107°. The results are important for designing oxynitride coatings, and pathways for their preparation, for various technological applications.

Keywords: Hafnium oxynitride; Reactive HiPIMS; Optical properties; Mechanical properties

1. Introduction

Hafnium dioxide (HfO_2) is an important material for a wide range of applications. Examples include electronics [1–3], nuclear industries [4], surfaces with controlled wettability [5], optical devices and other technologies (see e.g. Ref. [6] for a more detailed overview). Recently, it was reported that the addition of nitrogen into HfO_2 to form hafnium oxynitride (Hf-O-N) leads to an improvement of thermal stability [7], electrical [7,8], ferroelectric [9] and mechanical [10] properties. Moreover, the nitrogen incorporation can stabilize high-temperature (cubic or tetragonal) phases of HfO_2 [9,11]. Even a low nitrogen content (up to 5 at. %) in Hf-O-N results in an increase by about 300 °C in crystallization temperature, higher dielectric constant, lower leakage current at the same equivalent oxide thickness and higher dielectric strength compared to HfO_2 [12]. The elemental compositions reported in Ref. [12] were, however, prepared by a two-step process: HfN was deposited by magnetron sputtering, and then annealed at 650 °C in order to oxidize it. Another two-step method of Hf-O-N preparation is nitridation of HfO_2 by a post-deposition remote plasma treatment [13].

Reactive magnetron sputtering is a suitable method to prepare Hf-O-N films [8–11] in a

one-step process allowing a direct incorporation of nitrogen into the materials. Moreover, magnetron sputtering can be easily scaled up from small-sized laboratory deposition systems to large-scale industrial devices. However, the processes at both the target surface and the growing film surface are affected by a much higher affinity of Hf to oxygen than to nitrogen. Let us recall the standard molar enthalpy of formation of -1113.7 kJ/mol for HfO_2 [14] and -369.3 kJ/mol for HfN [14]. Thus, smooth control of the composition of Hf-O-N (as well as many other metal oxynitrides) constitutes a big challenge of a high current interest. Here, an (almost) linear relationship between the O_2+N_2 reactive gas (RG) mixture composition and the film composition (not achieved in the aforementioned Refs. [9–11]) can be considered as a criterion of success.

In our recent paper [6], we reported high-rate (200 nm/min) reactive sputtering of densified stoichiometric HfO_2 films using high-power impulse magnetron sputtering (HiPIMS) with a feedback pulsed reactive gas flow control (RGFC). The benefits of HiPIMS include (i) intense sputtering of atoms from the target resulting in a high deposition rate, (ii) a strong “sputtering wind” of the sputtered atoms resulting in a reduced flux of the RG particles onto the target and their enlarged flux onto the substrate, and (iii) highly ionized fluxes of film-forming particles (both RG particles and sputtered metal atoms) and enhanced energies of the ions bombarding the growing films, resulting in their structural changes and densification without a substrate bias. In parallel, RGFC [15,16] (Sec. 2.1) is able to maintain a sputter deposition of stoichiometric films in a transition zone close to the metallic mode, allowing for a high-rate deposition of densified stoichiometric oxides and oxynitrides. The fact that the high deposition rates achieved by HiPIMS with reactive gas pulsing are not achieved at the cost of multilayered structure was confirmed by high-resolution electron microscopy in Ref. [17].

Furthermore, we have shown that placing the reactive gas inlet into the most intense zone of a HiPIMS discharge leads to a high degree of dissociation of both O_2 and N_2, and consequently to a replacement of the aforementioned different reactivities of O_2 and N_2 by similar (high) reactivities of atomic O and N. In this way, we have recently prepared Ta-O-N films of smoothly controlled compositions with high deposition rates of 97-190 nm/min [18].

The present paper deals with the structure and properties of Hf-O-N films with smoothly controlled composition, prepared by high-rate reactive HiPIMS with RGFC. Special attention is paid to Hf-O-N films with a low N content (≤4 at.%). The films were prepared onto floating substrates at low substrate temperatures (<140 °C). We show the smoothly controlled composition also in terms of smoothly controlled materials properties, and discuss the relationships between the elemental composition, phase composition, and optical, electrical, mechanical and hydrophobic properties.

2. Experimental details

2.1. Hf-O-N preparation

The Hf-O-N materials were prepared in the form of thin films on Si (100) and glass substrates using a strongly unbalanced magnetron with a directly water-cooled planar Hf target (with a trace amount of Zr; diameter of 100 mm and thickness of 6 mm) in a cylindrical stainless-steel vacuum chamber (diameter of 507 mm and length of 520 mm). The target-to-

substrate distance was 100 mm. The base pressure before the depositions was 10^{-3} Pa. The magnetron was driven by a high-power pulsed dc power supply (HMP 2/1, Hüttinger Elektronik). The repetition frequency was 500 Hz, the voltage pulse duration was 200 µs and the deposition-averaged target power density was approximately 30 Wcm^{-2}, which is close to a target power density applicable in industrial HiPIMS systems. The substrate surface temperature reached during the depositions (without any external heating) was less than 140 °C. More details about the deposition setup and the choice of some of the process parameters (for N-free HfO_2) are given in Ref. [6].

The Ar flow rate was 30 sccm and the pumping speed of the diffusion pump was adjusted to attain the argon partial pressure at the same value of 2 Pa for all the depositions. The RG (O_2+N_2) inlet was placed into the most intense zone of the HIPIMS discharge (20 mm above the target) in order to maximize the RG dissociation, and oriented towards the substrate (following the discussion in Ref. [16]). Flow rates of RG were controlled by a feedback pulsed reactive gas controller [6] (that is, the duration of the RG pulses was not preset such as in e.g. Ref. [19]). The N_2 fraction in the average RG flow is denoted by [N_2] from now. In particular, we present seven films prepared at [N_2] = 0, 0.9, 2.6, 5, 25, 50 and 100%. The depositions of Hf-O(-N) films with a low [N_2] (0, 0.9, 2.6 and 5 %) were performed at an O_2 flow rate pulsing between 0 and 16 sccm, and a fixed N_2 flow rate (0, 0.1, 0.3 or 0.6 sccm, respectively). In this case, the process controller provided a control feedback signal to the O_2 mass flow controller in order to adjust the duration of the O_2 pulses. The depositions of Hf-(O)-N films with a high [N_2] (25, 50 and 100 %) were performed at a total O_2+N_2 flow rate pulsing between 0 and 16 sccm ([N_2] = 25%) or 14 sccm ([N_2] = 50 or 100%). In this case, the process controller provided a control feedback signal to both synchronized RG mass flow controllers, in order to adjust the duration of the simultaneous O_2 and N_2 pulses. In all depositions, we used the same control process parameter and its critical value: RG partial pressure (difference of the total and the fixed Ar pressure) of 0.10 Pa (value optimized for stoichiometric HfO_2 [6]). The total pressure was measured using a high-stability capacitance manometer (Baratron, type 627, MKS Instruments) with the accuracy of approximately 1%.

2.2. Hf-O-N characterization

The film thickness (between 1200 and 1500 nm) was measured at the film edge by profilometry (Dektak 8 Stylus Profiler, Veeco). The maximum measurement error of this technique was well below 1 %. The position of the film edge at the substrate holder was the same in all the depositions, with the center of the edge 10 mm from the axis. The deposition rate, a_D, was determined as the ratio of the film thickness to the deposition time. The same profilometer was used to measure the surface roughness (≤8 nm) and the bending of the Si substrates after the depositions. The residual macrostress, σ, was determined from the bending using the original Stoney's formula (see, for example, Ref. [20]).

The elemental composition of the films was investigated by wavelength dispersive spectroscopy (WDS) carried out in a scanning electron microscope (SU-70, Hitachi) equipped with WDS detector (Magnaray, Thermo Scientific) using a primary electron energy of 5 keV. The commercial standards (Astimex) for SiO_2 and metallic Hf were used for oxygen and hafnium evaluation. The Hf-O-N film prepared at [N_2] = 50% was used as a nitrogen standard

for calibration of WDS by X-ray photoelectron spectroscopy (XPS). The N content in this film was measured by the XPS using MgKα X-ray source and five-channel hemispherical analyzer (EA 125, Omicron) tuned to pass energy of 20 eV. In order to eliminate the influence of an oxidized surface layer, the films were treated by Ar^+ bombardment (25 min, 1.5 μA, 1 kV, 30°).

X-ray diffraction (XRD) measurements were carried out on the PANalytical X'Pert PRO diffractometer working in the Bragg–Brentano geometry using a CuKα (40 kV, 40 mA) radiation. To avoid a strong reflection from the Si (100) substrate, a slightly asymmetrical diffraction geometry with an ω-offset of 1.5° was used. Samples were scanned over the 2θ-range from 8° to 108°.

Phase structure of the films was also studied by Fourier transform infrared spectroscopy (FTIR) in transmission using the Vertex 80v (Bruker Optics) instrument. The measured film transmittance was converted to the absorption coefficient, α (i.e. a bulk quantity, not affected by the interference and reflectance), using the film thickness measured at the same location by ellipsometry and the same software which was used for ellipsometric measurements (described below). The light absorption was represented by a combination of Gaussian oscillators.

The refractive index, n, and extinction coefficient, k, were determined by variable angle spectroscopic ellipsometry using the J.A. Woollam Co. Inc. instrument. The measurements were performed using angles of incidence of 65°, 70° and 75° in reflection. The optical data were fitted in the wavelength (λ) range of 300-2000 nm using the WVASE software (below we also discuss n and k at λ = 550 nm, n_{550} and k_{550}). The optical model consisted of a c-Si substrate, a Hf-O-N layer and a surface roughness layer. The transparent (O-rich) Hf-O-N layers ($[N_2] \leq 25\%$) were described by the Cauchy dispersion formula with the Urbach absorption tail. The opaque (N-rich) Hf-O-N layers ($[N_2] \geq 50\%$) were described by a combination of Lorentz oscillators.

The room-temperature electrical resistivity, ρ, of the Hf-O-N films, deposited on non-conductive glass substrates, was measured by a standard four point technique with a 1-mm spacing between tips.

The coating hardness, H, elastic recovery, W_e, and the effective Young's modulus, $E^* = E/(1-\upsilon^2)$, where E and υ are the Young's modulus and the Poisson's ratio, respectively, were determined using an ultramicroindenter (Fischerscope H-100B) according to the ISO 14577-1:2002 E standard. The measurements were performed with a preset maximum load of 20 mN (leading to indentation depths below 10% of the aforementioned thickness values). The deviations determined from 25 measurements at different locations of 20 × 20 mm^2 samples were 6 %, 2 % and 4 % for H, W_e and E^*, respectively. The cracking resistance was confirmed by high-load indentation tests at a maximum load of 0.5 N.

The water droplet contact angle (WDCA) was determined by the Drop Shape Analyzer DSA30, KRUSS GmbH using the sessile drop method with the volume of a deionised water droplet of 2 μl. The maximum measurement error of this technique was about 1 %.

3. Results and discussion

This section is organized as follows. First, we show the elemental composition (Fig. 1) and high deposition rate (Fig. 2) of Hf-O-N films prepared by HiPIMS with RGFC. Next, we discuss the phase structure of the films (Figs. 3 and 4). Lastly, we present their optical (Fig. 5), electrical (Fig. 6), mechanical (Fig. 7) and hydrophobic (Fig. 8) properties.

3.1. Elemental composition and deposition rate

Figure 1 shows that the elemental composition (in at. %) of the films varied in a wide range, from $Hf_{32}O_{66}$ (less than 2 at. % of Ar and less than 1 at. % of Zr; referred to as HfO_2 below) to $Hf_{57}O_6N_{33}$ (less than 4 at. % of Ar and less than 1 at. % of Zr). At the first place, the figure shows that the system geometry and deposition technique described in Sec. 2.1 (let us recall the high degree of RG dissociation) facilitated the incorporation of low N contents of 0-4 at. % into the films at as low $[N_2]$ as 0-5 %. An increasing $[N_2]$ from 5 to 100 % resulted in a rising incorporation of N (from 4 to 33 at. %) into the films at a decreasing O content (from 59 to 6 at. %) and rising Hf content (from 35 to 57 at. %). The ability to smoothly control the film composition can be, for example, expressed in terms of comparable O and N contents in the film $Hf_{46}O_{29}N_{22}$ prepared at $[N_2]$ = 50%. The increasing incorporation of Hf with increasing $[N_2]$ can be explained not only (i) by different Hf contents in the corresponding stoichiometric binary phases (HfO_2 versus HfN), but also (ii) by the fact that the critical RG partial pressure used in all depositions was optimized for stoichiometric HfO_2 and (iii) by presumably even weaker target poisoning at higher $[N_2]$. The 6 at. % of O found in the film prepared at $[N_2]$ = 100 % is due to a release of the absorbed and subplanted oxygen from the chamber walls and the sputter target (similarly as e.g. in Refs. [18,21,22]).

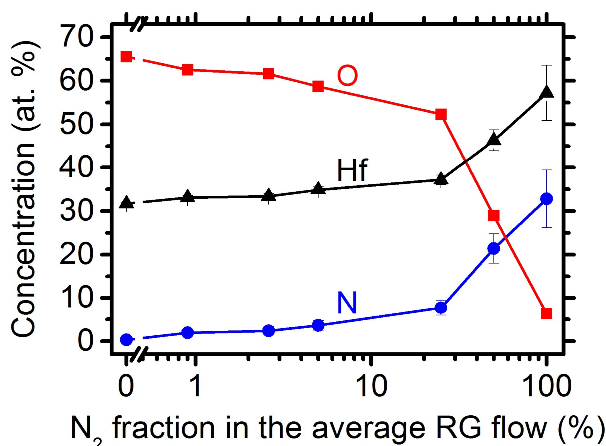

Figure 1. Elemental composition of Hf-O-N films prepared at various nitrogen fractions in the average flow rate of reactive gases. The compositions include $Hf_{32}O_{66}$, $Hf_{33}O_{63}N_2$, $Hf_{33}O_{62}N_3$, $Hf_{35}O_{59}N_4$, $Hf_{37}O_{52}N_8$, $Hf_{46}O_{29}N_{22}$, $Hf_{57}O_6N_{33}$ for $[N_2]$ = 0, 0.9, 2.6, 5, 25, 50 and 100%, respectively.

Figure 2 shows the deposition rate of the Hf-O-N films. Very high a_D = 230-240 nm/min was achieved for stoichiometric HfO_2 and HfO_2-like ($[N_2]$ = 0-5 %) films. For a detailed discussion on maximizing the deposition rate using RGFC, see Refs. [6,23]. The

slowly decreasing deposition rate for $[N_2] > 5$ % correlates with the aforementioned increasing Hf incorporation (decreasing RG incorporation), i.e. decreasing total number of film atoms per one deposited Hf atom. Similar correlation was found (at $[N_2]$ = 50-100%) for Ta-O-N films prepared by the same technique [18].

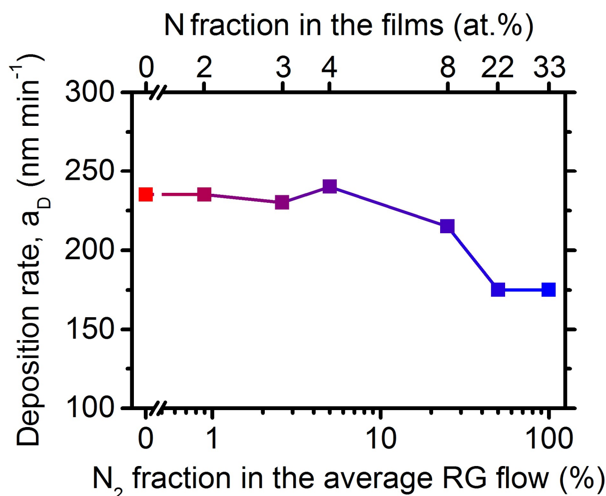

Figure 2. Deposition rates, *a*, of Hf-O-N films prepared at various nitrogen fractions in the average flow rate of reactive gases.

3.2 Hf-O-N structure

Figure 3 shows the film structure as studied by XRD. It indicates a nanocrystalline structure of all the films, with some of the diffraction peaks shifted to lower 2θ values due to a compressive stress σ = 0.1–1.6 GPa (Sec. 3.3). First, the pure oxide ($[N_2]$ = 0%) exhibits predominantly monoclinic HfO_2 phase (m-HfO_2), with a preferred orientation (−111) of planes parallel to the film surface. Second, the films prepared at $[N_2]$ = 0.9–2.6% ($Hf_{33}O_{63}N_2$ – $Hf_{33}O_{62}N_3$) also exhibit predominantly the m-HfO_2 phase, but with an enhanced amount of the tetragonal HfO_2 (t-HfO_2) or cubic HfO_2 (c-HfO_2) phase. This is consistent with the theoretical calculations [11] showing that the N incorporation increases the stability of the t- and c-HfO_2 phase with respect to the m-HfO_2 phase. The t-HfO_2 and c-HfO_2 phases are hard to distinguish experimentally [9,11]. The t- and/or c-HfO_2 phase with a preferred orientation (101) becomes dominant in the films prepared at $[N_2]$ = 5-25% ($Hf_{35}O_{59}N_4$ – $Hf_{37}O_{52}N_8$). Third, the film prepared at $[N_2]$ = 50% ($Hf_{46}O_{29}N_{22}$) exhibits the cubic $HfN_{0.6}O_{0.4}$ (c-$HfN_{0.6}O_{0.4}$) phase with a preferred orientation (111) at a presence of an amorphous phase (HfO_2 or O-rich Hf-O-N). Finally, the film prepared at $[N_2]$ = 100% ($Hf_{57}O_6N_{33}$) exhibits the cubic HfN (c-HfN) phase with a preferred orientation (200) at a small amount of ε-$HfN_{0.67}$ and a presence of an amorphous phase. Let us recall that the preparation of c-HfN is facilitated by the aforementioned high degree of RG dissociation, suppressing the role of contaminant O. For an example of conventional magnetron sputtering of Hf in N_2 which did not lead to c-HfN formation, see e.g. Ref. [10].

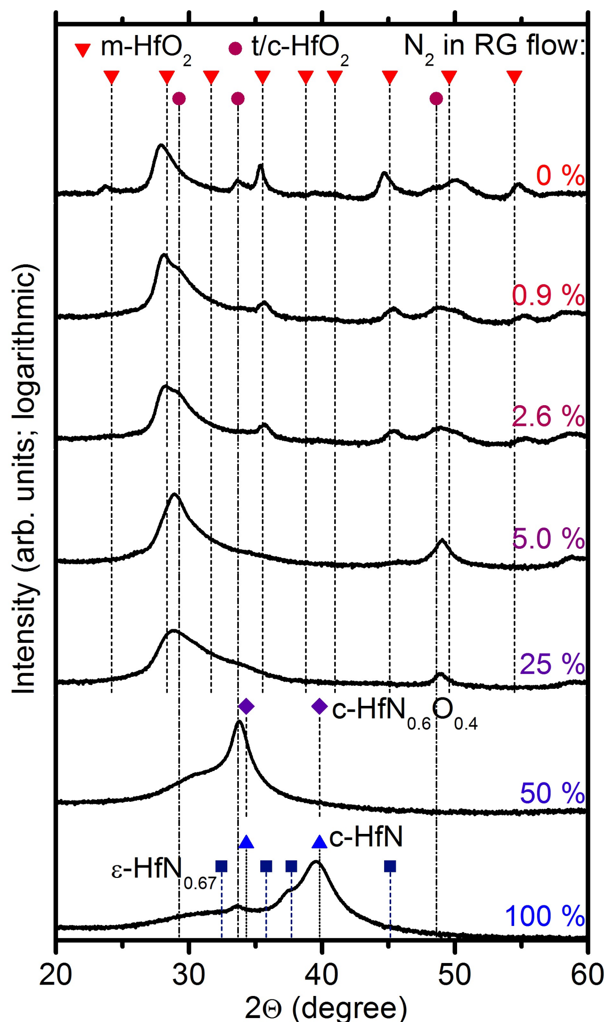

Figure 3. The logarithmic-scaled X-ray diffraction patterns taken from Hf-O-N films prepared at various nitrogen fractions in the average flow rate of reactive gases. The main diffraction peaks of m-HfO_2 (Card No. 00-034-0104), t-HfO_2 (Card No. 04-002-5353) or c-HfO_2 (Card No. 04-004-9003), c-$HfN_{0.6}O_{0.4}$ (Card No. 04-001-6517), ε-$HfN_{0.67}$ (Card No. 04-004-6450) and c-HfN (Card No. 00-033-0592) phases are marked. All cards were taken from Ref. [24].

Figure 4 (complementary to Fig. 3) shows the bonding and phase structure of the film bulk (let alone the surface bonds with H) in terms of the absorption coefficient (α = $4\pi k/\lambda$) obtained by FTIR. The pure oxide ([N_2] = 0%) exhibits three sharp peaks at 418, 524 and 743 cm^{-1}. The corresponding strongest oscillators (Sec. 2.2) are centered at 405, 510 and 737 cm^{-1}, respectively (the maxima of α are slightly shifted to higher wavenumbers due to its dependence on λ). There are two more (weaker) oscillators centered at 675 and 879 cm^{-1}. All these five oscillators have to be interpreted as vibrational modes in (predominantly monoclinic) HfO_2, see the composition (Fig. 1) and XRD (Fig. 3). The positions of the three strongest oscillators are consistent with HfO_2 vibrational frequencies reported in Refs. [3] (392-396 and 505-508 cm^{-1}), [25] (400, 515 and 748 cm^{-1}) and [26] (512 and 750 cm^{-1}). Increasing [N_2] leads to flatter peaks (higher broadening of the oscillators, particularly those centered around 405 and 510 cm^{-1}), indicating increasingly disordered structure.

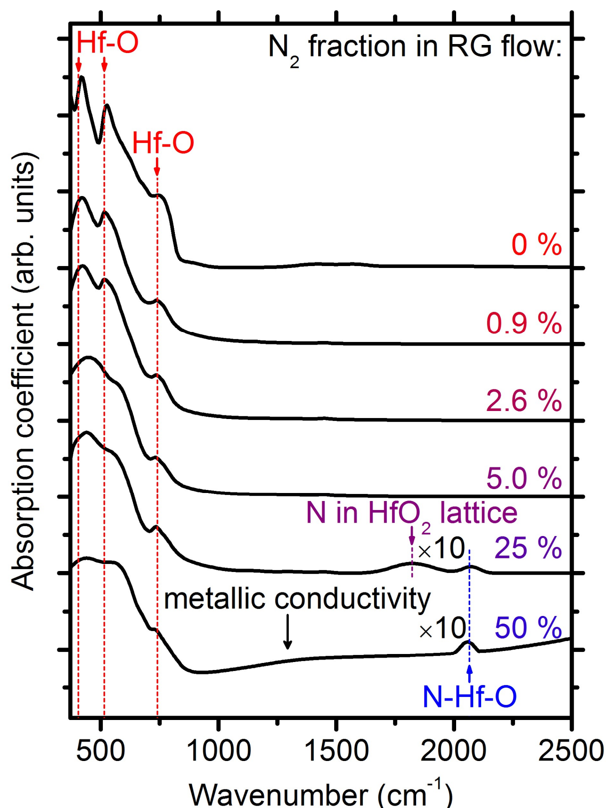

Figure 4. Absorption coefficient (obtained by FTIR) of Hf–O–N films prepared at various nitrogen fractions in the average flow rate of reactive gases. The three strongest peaks (vibrational modes) corresponding to HfO_2 are marked according to Refs. [3,25,26]. The weak peaks (10× enhanced) corresponding to the presence of N in HfO_2 and to N-Hf-O bonds in the oxynitride phase are marked according to our interpretation discussed in the text.

Furthermore, there are three features which appear in the spectra at enhanced [N_2]. First, there is a peak at 1823 cm^{-1} (oscillator centered at 1820 cm^{-1}) present only at [N_2] = 25%. Taking into account the film structure and elemental composition, this peak may correspond to some vibrational mode characteristic of a presence of N atoms in the HfO_2 lattice. This is consistent with the transition from m-HfO_2 to t/c-HfO_2 due to the N incorporation into the crystals as observed by XRD (Fig. 3). Second, there is a peak at 2071 cm^{-1} ([N_2] = 25%) - 2054 cm^{-1} ([N_2] = 50%) which probably represents one of vibrational modes characteristic of the N-Hf-O bonding in an oxynitride phase with high contents of both O and N. This is consistent with the observation of c-$HfN_{0.6}O_{0.4}$ by XRD (Fig. 3). See Ref. [18] for a similar interpretation of peaks present in FTIR spectra of Ta-O-N films prepared by the same technique at [N_2] = 25-30% (N in Ta_2O_5 lattice) and 25-60% (N-Ta-O bonding in an oxynitride). Third, the films prepared at [N_2] ≥ 50% were found to be metallic (in agreement with the values of their extinction coefficient and electrical resistivity, see Sec. 3.3). Thus, the light absorption by conduction electrons becomes the main absorption mechanism, and the absorption coefficient is consequently well above zero at all wavenumbers (shown for [N_2] = 50%, not shown for [N_2] = 100% where α was not quantified due to the zero transmittance).

3.3 Hf-O-N properties

Figures 5 and 6 show the characteristics of Hf-O-N films which are directly related to their electronic structure, namely n and k (Fig. 5) and ρ (Fig. 6a). First, the film prepared at $[N_2]$ = 0% exhibits high (for pure HfO_2) n_{550} = 2.12, and very low $k_{550} = 5\times10^{-4}$. The n_{550} value is at the upper bound of the range 2.07-2.12 (results in Ref. [6]) or 1.89-2.125 (literature overview in Ref. [6], even including the high-density cubic phase), and indicates that the film is fully densified. This confirms that the very high deposition rate (Fig. 2) was not achieved at the cost of porosity (which would lead to lower n) or understoichiometry (which would lead to enhanced k). The dispersions of n and k (Fig. 5) indeed correspond to a wide band gap HfO_2, and are therefore consistent with unmeasurable ρ (>10^8 Ωm; Fig. 6a).

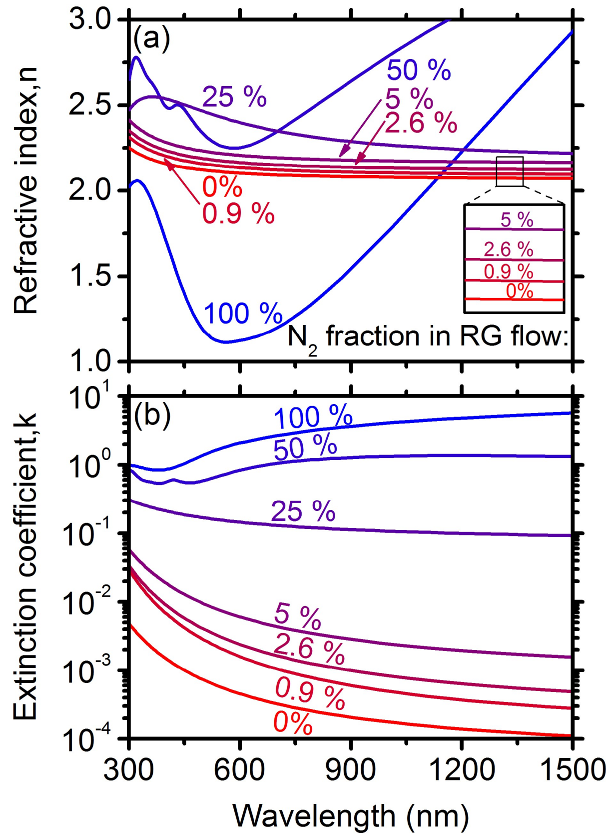

Figure 5. Dispersion of the refractive index (panel a) and extinction coefficient (panel b) of Hf–O–N films prepared at various nitrogen fractions in the average flow rate of reactive gases.

Second, the O-rich Hf-O-N films prepared at $[N_2]$ up to 5% exhibit a qualitatively similar dispersion of n and k as pure HfO_2 (in agreement with the qualitatively similar film structure, see Sec. 3.2). Quantitatively, Fig. 5 shows slowly increasing n_{550} from 2.12 at $[N_2]$ = 0% (HfO_2) to 2.22 at $[N_2]$ = 5% ($Hf_{35}O_{59}N_4$), and increasing k_{550} from 5×10^{-4} at $[N_2]$ = 0% to 7×10^{-3} at $[N_2]$ = 5%. The increasing k (stronger Urbach tails) can be explained by the presence of electronic states localized on nitrogen inside the original HfO_2 band gap, see the schematic drawing in Fig. 6b and the discussion in Ref. [27]. Such an evolution of the electronic structure is also in agreement with the evolution of ρ (Fig. 6a), which dropped from unmeasurable values at $[N_2]$ = 0% to 2×10^5 Ωm at $[N_2]$ = 5%.

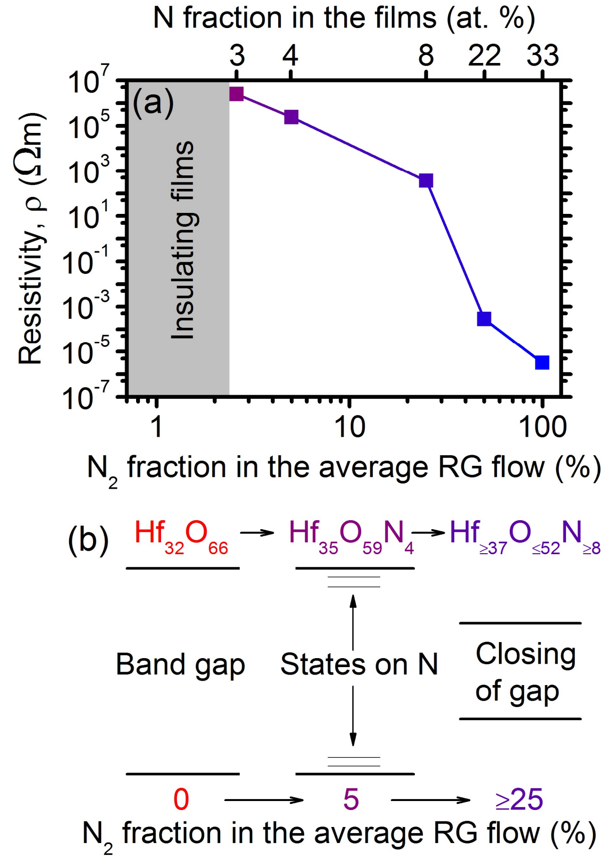

Figure 6. Electrical resistivity (panel a) and schematic drawing of the band gap (panel b) of Hf-O-N films prepared at various nitrogen fractions in the average flow rate of reactive gases.

Third, the film prepared at $[N_2]$ = 25% ($Hf_{37}O_{52}N_8$) can be considered as a transition case. It still retains some qualitative features of the materials prepared at $[N_2] \leq 5\%$ (monotonously decreasing $k(\lambda)$, almost monotonously decreasing $n(\lambda)$, no infrared absorption by free charge carriers shown in Fig. 4), but the quantitative values of its properties are already far from those obtained at $[N_2] \leq 5\%$: $n_{550} = 2.43$ (Fig. 5a), $k_{550} = 0.16$ (Fig. 5b) owing to a gradually closing band gap (schematic drawing in Fig. 6b) and $\rho = 360$ Ωm (Fig. 6a). This is consistent with the film structure which is also not completely HfO_2-like anymore, see e.g. the newly appeared FTIR peaks in Fig. 4.

Fourth, the films prepared at $[N_2]$ = 50% ($Hf_{46}O_{29}N_{22}$) - 100% ($Hf_{57}O_6N_{33}$) exhibit unambiguously metallic (HfN-like) behavior (see also the transition from HfO_2-like to HfN-like structure shown in Fig. 3, and the infrared absorption by free charge carriers shown at $[N_2]$ = 50% in Fig. 4). The band gap closed, the n dispersion (Fig. 5a) is far from monotonous, k_{550} (Fig. 5b) further increased to 0.71 ($[N_2]$ = 50%) - 1.77 ($[N_2]$ = 100%) and ρ (Fig. 6) further decreased to 2.8×10^{-4} Ωm ($[N_2]$ = 50%) – 3.2×10^{-6} Ωm ($[N_2]$ = 100%).

Figure 7 shows the mechanical properties of Hf-O-N films. The film hardness (Fig. 7a) increases with $[N_2]$, from H = 18 GPa at $[N_2]$ = 0% (HfO_2) to H = 25 GPa at $[N_2]$ = 100% ($Hf_{57}O_6N_{33}$). This increase is consistent with the relatively lower hardness of oxides compared to the corresponding nitrides reported for other transition metals, e.g. Ta [18], Zr [28], Y [28] or Ti [29]. The oxide hardness of 18 GPa is at the upper bound of the range 15-18 GPa (results in Ref. [6]), let alone 9-15 GPa (literature overview in Ref. [6]), and confirms (in

parallel to the refractive index discussed above) the film densification. All prepared Hf-O-N films exhibit low compressive macrostress σ = 0.1-1.6 GPa (Fig. 7a), E^* ≥ 172 GPa (not shown) and high values of the ratio H/E^* ≥ 0.1 (Fig. 7b) and W_e ≥ 60 % (Fig. 7b). Note that the aforementioned properties fulfill the requirements for material's resistance to cracking according to Refs. [22,30]: H/E^* (measure of the elastic strain to failure [31]) > 0.1, W_e > 60% and σ < 0. There is a typical result of a high-load (0.5 N) indentation test, performed for all Hf-O-N films, in the inset of Fig. 7b. The same load was used e.g. for evaluating the cracking resistance of ZrN in Ref. [22]. Indeed, the inset shows that there are no cracks around the dent.

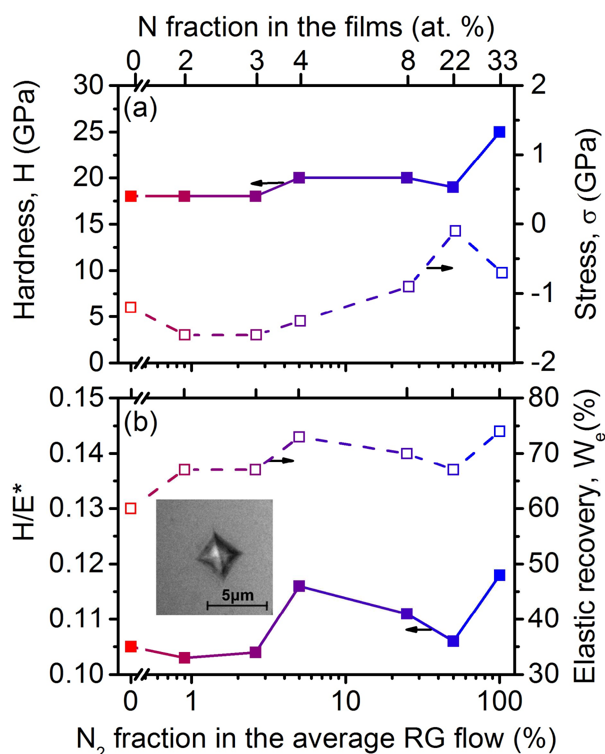

Figure 7. Hardness, *H*, residual macrostress, *σ*, (panel a) and hardness to effective Young's modulus ratio, H/E^*, elastic recovery, W_e, (panel b) of Hf–O–N films prepared at various nitrogen fractions in the average flow rate of reactive gases. The inset in panel b shows a typical optical microscope image of the dent (with no cracks around it) in the surface of the Hf-O-N films at a high load of 0.5 N.

Figure 8a shows the dependence of the water droplet contact angle of the Hf-O-N films on [N_2]. The figure shows that all films are hydrophobic and that WDCA increases (at the aforementioned low surface roughness) with increasing [N_2] from 101 to 107 °. This increase is consistent with the relatively lower WDCA of oxides compared to the corresponding nitrides reported for various metals (but not Hf) in Ref. [28].

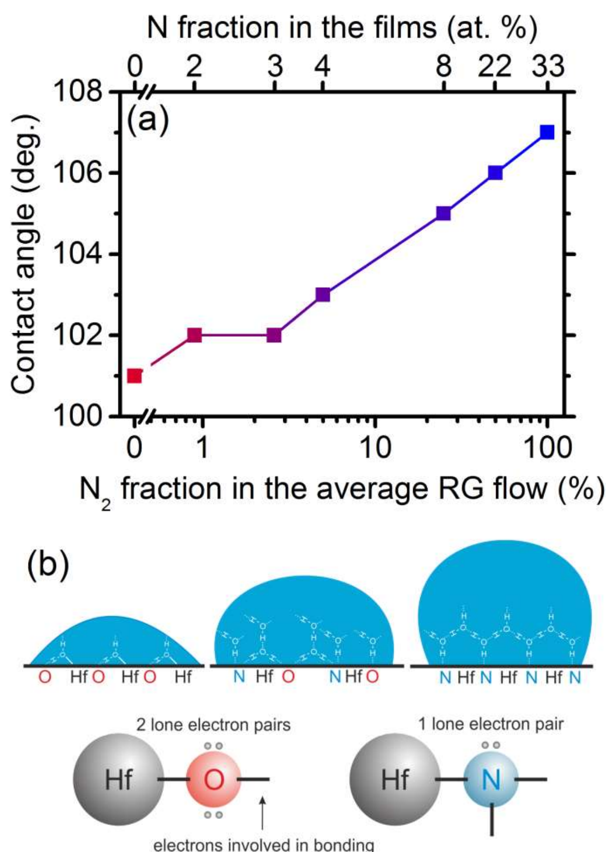

Figure 8. Water droplet contact angle (panel a) of Hf–O–N films prepared at various nitrogen fractions in the average flow rate of reactive gases. Schematic drawing of the hydrophobicity of the film surface and of the minimum number of valence electron lonepairs associated with O and N anions (panel b). The drawing for ternary Hf-O-N is analogous to that in Ref. [28] for binary metal oxides and metal nitrides.

The hydrophobicity in itself is supported by the low electronegativity of Hf, i.e. low ability of Hf to form coordinate covalent bonds with water oxygen which would support the water chemical adsorption. The higher WDCA at higher [N_2] can be explained by lower localization of the electronic charge on N, i.e. lower ability of N to form hydrogen bonds with water hydrogen which would, again, support the water chemical adsorption. Nitrogen is known to have only one lonepair of valence electrons, while oxygen is known to have at least two lonepairs (see also the schematics in Fig. 8b). This difference can be further emphasized by a stronger localization of all occupied valence electron states on O in ionically bonded HfO_2, contrary to the covalent and metallic bonding in HfN.

4. Conclusions

Hafnium oxynitride films were prepared in a one-step process by high-power impulse magnetron sputtering at a low deposition temperature (<140 °C) and without using substrate bias. Feedback pulsed reactive gas flow control made it possible to achieve very high deposition rates (up to 230 nm/min) and smoothly controlled composition from $Hf_{32}O_{66}$ to $Hf_{57}O_6N_{33}$. Special attention was paid to compositions with low N contents.

All films were nanocrystalline. Increasing the N content in the films allowed us to control the film structure, from m-HfO_2 through t/c-HfO_2 (dominant phase at 4-8 at.% N in the films) and c-$HfN_{0.6}O_{0.4}$ to c-HfN. The evolution of smoothly controlled films properties along the transition from HfO_2 to HfN includes, for example, extinction coefficient at 550 nm from 5×10^{-4} to 1.77, electrical resistivity from $>10^8$ Ωm to 3.2×10^{-6} Ωm, hardness from 18 GPa to 25 GPa or water droplet contact angle from 101° to 107°. The results are important for designing oxynitride coatings, and pathways for their preparation, for various technological applications.

Acknowledgment

This work was supported by the Grant Agency of the Czech Republic under Project No. GA14-03875S.

References

[1] J.H. Choi, Y. Mao, J.P. Chang, Development of hafnium based high-k materials - A review, Mater. Sci. Eng. R 72 (2011) 97–136.

[2] G. He, X. Chen, Z. Sun, Interface engineering and chemistry of Hf-based high-k dielectrics on III-V substrates, Surf. Sci. Rep. 68 (2013) 68–107.

[3] J.C. Hackley, T. Gougousi, Properties of atomic layer deposited HfO_2 thin films, Thin Solid Films 517 (2009) 6576–6583.

[4] J. Wang, H.P. Li, R. Stevens, Hafnia and hafnia-toughened ceramics, J. Mater. Sci. 27 (1992) 5397–5430.

[5] S. Zenkin, A. Belosludtsev, Š. Kos, R. Čerstvý, S. Haviar, M. Netrvalová, Thickness dependent wetting properties and surface free energy of HfO_2 thin films, Appl. Phys. Lett. 108 (2016) 231602.

[6] J. Vlček, A. Belosludtsev, J. Rezek, J. Houška, J. Čapek, R. Čerstvý, et al., High-rate reactive high-power impulse magnetron sputtering of hard and optically transparent HfO_2 films, Surf. Coat. Technol. 290 (2016) 58–64.

[7] Y. Wang, H. Wang, J. Zhang, H. Wang, C. Ye, Y. Jiang, et al., Improved thermal stability, interface, and electrical properties of HfO_2 films prepared by pulsed laser deposition using in situ ionized nitrogen, Appl. Phys. Lett. 95 (2009) 032905.

[8] B.J. Murdoch, R. Ganesan, D.R. McKenzie, M.M.M. Bilek, D.G. McCulloch, J.G. Partridge, Influence of nitrogen-related defects on optical and electrical behaviour in $HfO_{2-x}N_x$ deposited by high-power impulse magnetron sputtering, Appl. Phys. Lett. 107 (2015) 112903.

[9] L. Xu, T. Nishimura, S. Shibayama, T. Yajima, S. Migita, A. Toriumi, Ferroelectric phase stabilization of HfO_2 by nitrogen doping, Appl. Phys. Express. 9 (2016) 091501.

[10] P. Lei, S. Guo, J. Zhu, B. Dai, G. Liu, Y. Wang, et al., Enhanced mechanical properties of HfO_2 film by nitrogen doping, Surf. Eng. 32 (2016) 585–588.

[11] K. Sarakinos, D. Music, S. Mráz, M. to Baben, K. Jiang, F. Nahif, et al., On the phase formation of sputtered hafnium oxide and oxynitride films, J. Appl. Phys. 108 (2010) 014904.

[12] C.S. Kang, H.J. Cho, R. Choi, Y.H. Kim, C.Y. Kang, S.J. Rhee, et al., The electrical and material characterization of hafnium oxynitride gate dielectrics with TaN-gate electrode, IEEE Trans. Electron. Devices 51 (2004) 220–227.

[13] L.T. Huang, M.L. Chang, J.J. Huang, C.L. Kuo, H.C. Lin, M.H. Liao, et al., Effect of hydrogen participation on the improvement in electrical characteristics of HfO_2 gate dielectrics by post-deposition remote N_2, N_2/H_2, and NH_3 plasma treatments, J. Phys. D: Appl. Phys. 46 (2013) 1–6.

[14] W.F. Gale, T.C. Totemeier, Smithells metals reference book, eighth ed., Butterworth-Heinemann, Oxford, 2003.

[15] J. Vlček, J. Rezek, J. Houška, R. Čerstvý, R. Bugyi, Process stabilization and a significant enhancement of the deposition rate in reactive high-power impulse magnetron sputtering of ZrO_2 and Ta_2O_5 films, Surf. Coat. Technol. 236 (2013) 550–556.

[16] J. Vlček, J. Rezek, J. Houška, T. Kozák, J. Kohout, Benefits of the controlled reactive high-power impulse magnetron sputtering of stoichiometric ZrO_2 films, Vacuum 114 (2015) 131–141.

[17] N.W. Pi, M. Zhang, J. Jiang, A. Belosludtsev, J. Vlček, J. Houška, et al., Microstructure of hard and optically transparent HfO_2 films prepared by high-power impulse magnetron sputtering with a pulsed oxygen flow control, Thin Solid Films 619 (2016) 239–249.

[18] J. Rezek, J. Vlček, J. Houška, R. Čerstvý, High-rate reactive high-power impulse magnetron sputtering of Ta-O-N films with tunable composition and properties, Thin Solid Films 566 (2014) 70–77.

[19] N. Martin, J. Lintymer, J. Gavoille, J.M. Chappé, F. Sthal, J. Takadoum, et al., Reactive sputtering of TiO_xN_y coatings by the reactive gas pulsing process. Part I: Pattern and period of pulses, Surf. Coat. Technol. 201 (2007) 7720–7726.

[20] J. Gunnars, U. Wiklund, Determination of growth-induced strain and thermo-elastic properties of coatings by curvature measurements, Mater. Sci. Eng. A. 336 (2002) 7–21.

[21] L. García-González, L. Zamora-Peredo, N. Flores-Ramírez, M.G. Garnica-Romo, J. Hernández-Torres, Influence of Nitrogen Flow Rates on the Structure, Hardness, and Electrical Resistivity of HfN Coatings by DC Sputtering, J. Mater. Eng. Perform. 24 (2015) 1558–1564.

[22] J. Musil, S. Zenkin, Kos, R. Čerstvý, S. Haviar, Flexible hydrophobic ZrN nitride films, Vacuum 131 (2016) 34–38.

[23] T. Kozák, J. Vlček, A parametric model for reactive high-power impulse magnetron sputtering of films, J. Phys. D. Appl. Phys. 49 (2016) 55202.

[24] JCPDS-ICDD, PDF-4+ Database, International Centre for Diffraction Data, Newton Square, PA, USA, 2015.

[25] T.C. Chen, C.-Y. Peng, C.-H. Tseng, M.-H. Liao, M.-H. Chen, C.-I. Wu, et al., Characterization of the Ultrathin HfO_2 and Hf-Silicate Films Grown by Atomic Layer Deposition, IEEE Trans. Electron Devices. 54 (2007) 759–766.

[26] J. Ran, Z. Yan, Vacuum Field emission characteristics of HfO_xN_y films prepared by sputtering, http://www.paper.edu.cn/index.php/default/en_releasepaper/downPaper/200906-327, 2009 (accessed 14.11.2016).

[27] J. Choi, R. Puthenkovilakam, J.P. Chang, Effect of nitrogen on the electronic properties of hafnium oxynitrides, J. Appl. Phys. 99 (2006) 1–6.

[28] S. Zenkin, Š. Kos, J. Musil, Hydrophobicity of Thin Films of Compounds of Low-Electronegativity Metals, J. Am. Ceram. Soc. 97 (2014) 2713–2717.

[29] F. Vaz, P. Cerqueira, L. Rebouta, S.M. Nascimento, E. Alves, P. Goudeau, et al., Structural, optical and mechanical properties of coloured TiN_xO_y thin films, Thin Solid Films 447–448 (2004) 449–454.

[30] H. Kim, J. La, K. Kim, S. Lee, The effects of the H/E ratio of various Cr-N interlayers on the adhesion strength of CrZrN coatings on tungsten carbide substrates, Surf. Coat. Technol. 284 (2015) 230–234.

[31] A. Leyland, A. Matthews, On the significance of the H/E ratio in wear control: a nanocomposite coating approach to optimised tribological behaviour, Wear. 246 (2000) 1–11.

E. Reactive high-power impulse magnetron sputtering of ZrO_2 films with gradient ZrO_x interlayers on pretreated steel substrates

A. Belosludtsev, J. Vlček, J. Houška, R. Čerstvý

J. Vac. Sci. Technol. A (submitted for publication)

Reactive high-power impulse magnetron sputtering of ZrO_2 films with gradient ZrO_x interlayers on pretreated steel substrate

A. Belosludtsev, J. Vlček*, J. Houška, R. Čerstvý

Department of Physics and NTIS - European Centre of Excellence, University of West Bohemia, Univerzitní 8, 306 14 Plzeň, Czech Republic

*corresponding author: vlcek@kfy.zcu.cz

Abstract

High-power impulse magnetron sputtering with a pulsed O_2 flow control was used for reactive depositions of densified stoichiometric ZrO_2 films with gradient ZrO_x interlayers onto floating Si and steel substrates at low substrate temperatures (less than 150 °C). The depositions were performed using a strongly unbalanced magnetron with a planar Zr target of 100 mm diameter in Ar+O_2 gas mixtures at the total pressure close to 2 Pa. The repetition frequency was 500 Hz at the average target power density of about 37 Wcm^{-2} during a deposition of the ZrO_2 films and in the range from 30 Wcm^{-2} to 37 Wcm^{-2} during a deposition of the gradient ZrO_x interlayers with a controlled increase in x from $x \simeq 0$ to 2. The voltage pulse duration was 200 μs (duty cycle of 10 %). Two kinds of gradient ZrO_x interlayers with different depth profiles of x were deposited using the feed-back pulsed O_2 flow control. Prior to deposition, a modification of the substrate surfaces was performed by high-power impulse magnetron sputtering of the Zr target in Ar gas at the same pressure of 2 Pa, a voltage pulse duration of 50 μs, a peak target power density of 220 Wcm^{-2} in a pulse, a dc substrate bias from - 965 V to - 620 V in a target pulse and low substrate temperatures (less than 150 °C) for 10 min. It was shown that the pretreatment of the steel substrates is a necessary condition for adhesion of the zirconium oxide (both pure ZrO_2 and ZrO_2+ZrO_x interlayer) films and that the adhesion of the ZrO_2 films is substantially higher when the gradient ZrO_x interlayers are used. The densified stoichiometric ZrO_2 films (refractive index of 2.21 and extinction coefficient of 4×10^{-4} at the wavelength of 550 nm) deposited onto the gradient ZrO_x interlayers exhibited a high hardness (15-16 GPa) and an enhanced resistance to cracking.

Keywords: Controlled reactive HiPIMS; Pulsed reactive gas flow; Densified ZrO_2 films; Gradient ZrO_x interlayers; Pretreated steel substrates; Enhanced adhesion

1. Introduction

In recent years, high-power impulse magnetron sputtering (HiPIMS) systems have been used for deposition of films. The target power density in a pulse of these discharges with a peak value of up to several $kWcm^{-2}$ is orders of magnitude higher than a typical target power density (usually less than 20 Wcm^{-2}) applied in conventional dc magnetron sputtering. The high target power density leads to generation of very dense discharge plasmas with high degrees of ionization of sputtered atoms. Consequently, film deposition can be carried out at highly ionized fluxes of the target material atoms. This is of significant interest for deposition on complex-shaped substrates, for substrate-coating interface engineering, and ion-assisted growth of films.[1,2]

HiPIMS systems have been applied in the preparation of various optically transparent non-conductive and conductive oxides (see, for example, Refs. 1-4 and the works cited therein), and of thermochromic VO_2 films[5,6] and hydrophobic HfO_2 films.[7]

In our recent papers, we reported on high-rate reactive depositions of densified, highly optically transparent, stoichiometric ZrO_2,[4,8] Ta_2O_5[8] and HfO_2[9] films and Ta-O-N films with a tunable composition and properties[10] using HiPIMS with a pulsed reactive gas flow control (RGFC). This feed-back process control is able to maintain a sputter deposition of stoichiometric films in the region between a more and less metallic mode, and to utilize the following exclusive benefits of the HiPIMS discharges in preparation of films:[4] (i) intense sputtering of atoms from the target resulting in a substantially increased deposition rate, (ii) very high degrees of dissociation of RG molecules in the flux onto the substrate resulting in a higher incorporation of RG atoms into materials, (iii) a strong “sputtering wind” of the sputtered atoms resulting in a reduced flux of the RG particles onto the target and their enlarged flux onto the substrate, and (iv) highly ionized fluxes of particles with enlarged fractions of ionized sputtered metal atoms onto the substrate and enhanced energies of the ions bombarding the growing films resulting in their structural changes and densification without a substrate bias. The advantage of the proposed pulsed RGFC method is that it does not require any additional measurement or monitoring devices, such as a plasma emission monitoring system, mass spectrometer or Lambda sensor,[11,12] and that it is applicable to all magnetron sputtering discharges.

The present paper is focused on reactive sputter depositions of densified stoichiometric ZrO_2 films with gradient ZrO_x interlayers onto floating Si and steel substrates at low substrate temperatures (less than 150 °C) using HiPIMS with the pulsed RGFC. The main aim of the study is to investigate the effects of gradient ZrO_x interlayers on adhesion of the deposited ZrO_2-based coatings to the steel substrates pretreated using non- reactive HiPIMS. Motivation for this work is to develop a simple (no substrate bias voltage during reactive sputter depositions and no external heating during the whole process), industrially applicable technique for a fast deposition of densified stoichiometric oxide films with enhanced adhesion to industrially relevant metallic substrates.

ZrO_2 films were chosen in our investigations as an example of a technologically important material. It should be mentioned that ZrO_2 exhibits a high fraction toughness, high hardness and wear resistance, good frictional behavior, high temperature capability, low neutron absorption, low thermal conductivity and high biocompatibility. This combination of properties is attractive for a wide range of applications of ZrO_2-based coatings, such as cutting blades,[13] oxygen sensors,[14] dental[15-17] and orthopedic[17-19] implants, and a cladding material in nuclear industry.[20]

2. Experimental details

2.1. Coating preparation

Table I gives durations of the individual processes (substrate pretreatment, deposition of gradient ZrO_x interlayers and deposition of stoichiometric ZrO_2 films) and thicknesses of the corresponding gradient ZrO_x interlayers and stoichiometric ZrO_2 films for five different coatings deposited onto Si (100) and polished Cr-Mo-V steel (CSN 415330 standard) substrates at a floating potencial.

TABLE I. Durations of the individual processes and thicknesses of the corresponding gradient ZrO_x interlayers and stoichiometric ZrO_2 films, together with total thicknesses, for the coatings deposited onto Si and steel substrates.

Coating number	1	2	3	4	5
Substrate pretreatment	–	600 s	600 s	600 s	–
Gradient ZrO_x interlayer	–	–	$(\bar{I}_t)_{cr}$: linear 1000 s 1.8 μm	$(\bar{I}_t)_{cr}$: tanh 1000 s 1.8 μm	$(\bar{I}_t)_{cr}$: tanh 1000 s 1.8 μm
ZrO_2 film	1500 s 1.2 μm	1500 s 1.2 μm	500 s 0.4 μm	500 s 0.4 μm	–
Total thickness	1.2 μm	1.2 μm	2.2 μm	2.2 μm	1.8 μm

The substrate pretreatment and the depositions of the gradient ZrO_x interlayers and stoichiometric ZrO_2 films were carried out using a strongly unbalanced magnetron source with a directly water-cooled planar zirconium target (99.9 % Zr purity, diameter of 100 mm and thickness of 6 mm) in a standard stainless-steel vacuum chamber (diameter of 507 mm and length of 520 mm), which was evacuated by a diffusion pump (2 m^3s^{-1}) backed up with a rotary pump (30 m^3h^{-1}). The base pressure before deposition was 10^{-3} Pa. A detailed characterization of the magnetic field and the degree of its unbalance is given in Ref. 21. The Ar flow rate was set to 25 sccm and the pumping speed of the diffusion pump was adjusted to attain the argon partial pressure, p_{ar}, at the same value of 2 Pa for all the processes. The settings of the Ar flow rate and the pumping speed were not changed during the experiments. In all ZrO_x and ZrO_2 depositions, the total pressure of the argon–oxygen gas mixtures, measured with the accuracy of approximately 1 %, was close to 2 Pa. The target-to-substrate distance was 100 mm. The substrate temperature reached during the substrate pretreatment and the depositions of the gradient ZrO_x interlayers and stoichiometric ZrO_2 films without an external heater was less than 150 °C.

An additional grounded ring-shaped anode, which was periodically cleaned, was mounted into the system around the insulated substrate holder to suppress the "disappearing anode" effect.[12]

The magnetron was driven by a high-power pulsed dc power supply (HMP 2/1, Hüttinger Elektronik). In this work, the repetition frequency, f_r, was 500 Hz and the voltage pulse duration, t_{on}, was 50 μs during the substrate pretreatment and t_{on} = 200 μs during the ZrO_x and ZrO_2 depositions with the respective duty cycles t_{on}/T = 2.5 % and 10 %, where the pulse period $T = 1/f_r$. Prior to a substrate pretreatment, we set a negative dc substrate bias voltage at 965 V.

During the ZrO_x and ZrO_2 depositions, oxygen gas was admitted into the vacuum chamber from a source via mass-flow controllers and two corundum conduits (Fig. 1). Two O_2 inlets with a diameter of 1 mm were placed symmetrically above the target racetrack at the same distance of 20 mm from the target surface and oriented to the substrate. Such an inlet configuration is a result of optimization based on our extensive experiments.[4]

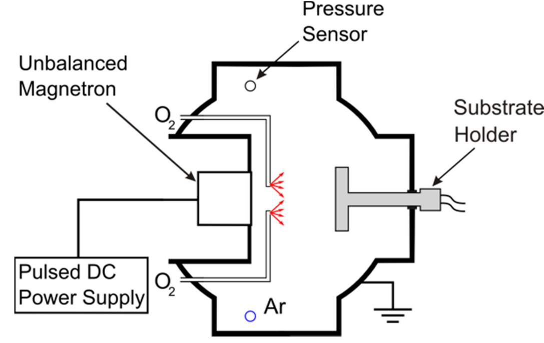

Figure 1. Schematic diagram of the deposition device with two O_2 inlets in front of the target (20 mm from the target surface). Positions of the pressure sensor and the Ar inlet in the back side of the vacuum chamber are also shown.

Waveforms of the magnetron target voltage, $U_t(t)$, the substrate voltage $U_s(t)$, the target current, $I_t(t)$, and the substrate current, $I_s(t)$, were monitored[4] and our own software evaluated the time-varying average target power density in a discharge pulse, S_{ta}, given by

$$S_{ta} = \frac{1}{t_{on}} \int_0^{t_{on}} U_t(t) J_t(t) dt. \tag{1}$$

Here, the target current density $J_t(t) = I_t(t) / A_t$, where A_t is the total area of the target (78.54 cm^2 in our case). The x-dependent (x is the stoichiometric coefficient) deposition-averaged target power density, $<S_t>$, was evaluated with the use of the formula

$$< S_t > = \frac{1}{t_e - t_s} \int_{t_s}^{t_e} U_t(t) J_t(t) dt, \tag{2}$$

where t_s and t_e are the start and end times of the deposition at a given value of x. The time-varying average target current in a period of the power supply, $\bar{I}_t$, was evaluated using the formula

$$\bar{I}_t = \frac{1}{T} \int_0^T I_t(t) dt. \tag{3}$$

A basic principle of the controlled reactive sputter depositions of the gradient ZrO_x interlayers and stoichiometric ZrO_2 films is illustrated in Figs. 2 and 3.

Prior to the deposition of a given coating, we set the nominal target voltage (essentially constant during discharge pulses), giving rise to different values of $<S_t>$ for different values of x. We also set the argon partial pressure (p_{ar} = 2 Pa in all experiments), a total oxygen flow rate, Φ_{ox}, in both conduits (Φ_{ox} = 12 sccm in all experiments), the O_2 inlet configuration (Fig. 1), and pre-selected critical values (Figs. 2 and 3) of the average discharge current in a period of the power supply, $(\bar{I}_t)_{cr}$, which was chosen to be the control process parameter in this work.[8] During the deposition, a process controller used then provides a control feed-back signal to the two O_2 mass-flow controllers to adjust the pulsed O_2 flow rate into the vacuum chamber by adjusting the duration of the O_2 flow rate pulses by means of the pre-selected values of $(\bar{I}_t)_{cr}$, which are monitored by the process controller. A detailed description of the control loop is given in Ref. 8.

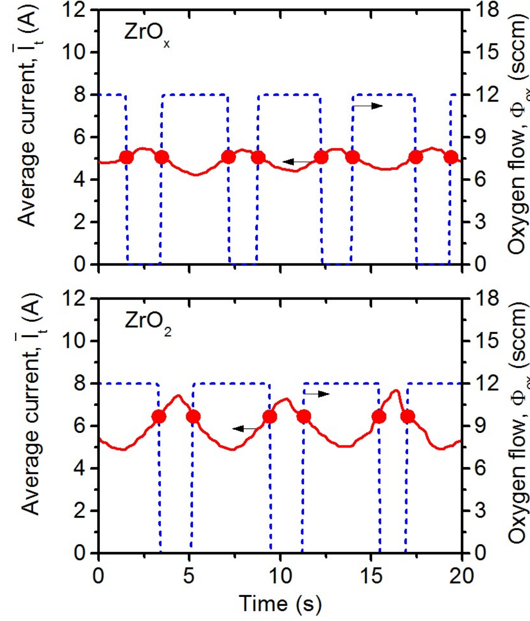

Figure 2. Time evolution of the average target current in a period of the power supply, $\bar{I}_t(t)$, and the corresponding oxygen flow rate pulses, Φ_{ox}, at the beginning of controlled reactive sputter depositions of the gradient ZrO_x interlayers, when x ≃ 0, with a deposition-averaged target power density $\langle S_t \rangle = 30$ Wcm^{-2} (upper panel) and during depositions of the stoichiometric ZrO_2 films with $\langle S_t \rangle = 37$ Wcm^{-2} (lower panel). Pre-selected critical values of $(\bar{I}_t)_{cr}$ determining the switching-on and switching-off of the oxygen flow rate $\Phi_{ox} = 12$ sccm are marked by dots.

In the present experiments, we used the preset deposition-averaged target power density $\langle S_t \rangle = 37$ Wcm^{-2} at a constant $(\bar{I}_t)_{cr} = 6.5$ A for depositions of the stoichiometric ZrO_2 films (Figs. 2 and 3). Under these conditions, the amount of oxygen injected into the discharge is sufficiently low to minimize arcing on the compound part of the metal target and to avoid a substantial reduction in the deposition rate of films, but it is sufficiently high to achieve a sufficient incorporation of the oxygen atoms into the films (stoichiometric ZrO_2 composition).

During depositions of the gradient ZrO_x interlayers, the pre-selected $(\bar{I}_t)_{cr}$ values have been increasing with time as a linear function or as a hyperbolic tangent from $(\bar{I}_t)_{cr} = 5.1$ A to 6.5 A at the corresponding $\langle S_t \rangle$ increasing from 30 Wcm^{-2} to 37 Wcm^{-2} (Figs. 2 and 3) to achieve a gradual rise in the stoichiometric coefficient x of the ZrO_x interlayers from x ≃ 0 to 2.

2.1. Coating characterization

The coating thickness (Table I) was measured at the coating edge by profilometry (Dektak 8 Stylus Profiler, Veeco) using a 380 μm thick removable Si step. The maximum measurement error of this technique was well below 1%. The position of the coating edge at the substrate holder was the same in all the depositions with the center of the coating edge 10 mm from the axis. The same profilometer was used to measure surface roughness, R_a, and bending of the Si (100) substrate after deposition of the coating, from which the residual macrostress was determined using the original Stoney's formula (see, for example, Ref. 22).

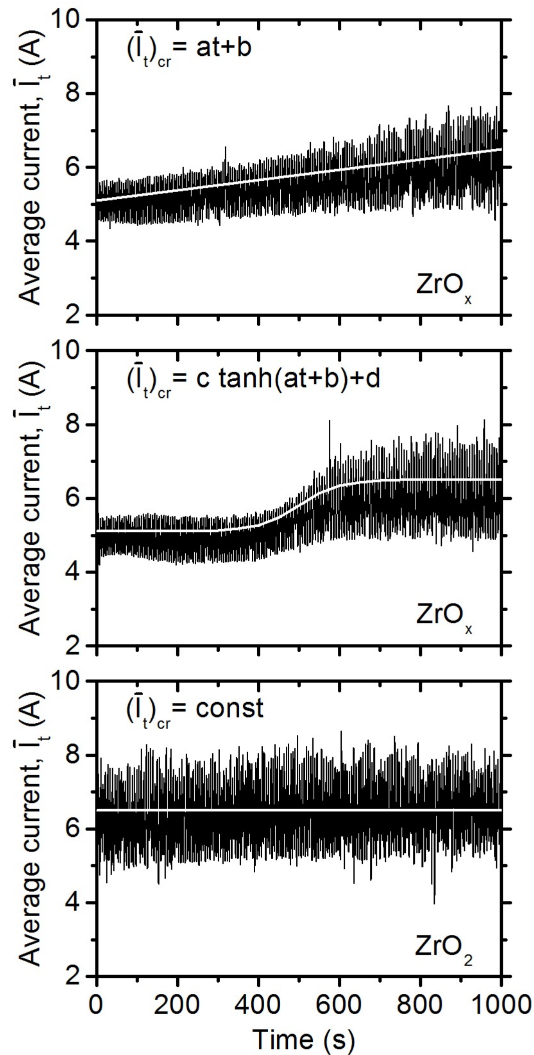

Figure 3. Time evolution of the average target current in a period of the power supply, $\bar{I}_t(t)$, during controlled reactive sputter depositions of the gradient ZrO_x interlayers with a gradually increasing deposition-averaged target power density $\langle S_t \rangle$ from 30 Wcm^{-2} to 37 Wcm^{-2} (top and middle panel), and during depositions of the stoichiometric ZrO_2 films with $\langle S_t \rangle = 37$ Wcm^{-2} (bottom panel). Pre-selected critical values of $(\bar{I}_t)_{cr}$ determining the switching-on and switching-off of the oxygen flow rate Φ_{ox} = 12 sccm are marked by white lines.

X-ray fluorescence (XRF) spectroscopy using a PANalytical XRF Spectrometer MagiX PRO was performed to identify Zr and Ar atoms implanted into a pretreated substrate and to confirm, with the use of a ZrO_2 standard, stoichiometry of the top ZrO_2 films in the coatings 1-4 (Table I).

X-ray diffraction (XRD) measurements were carried out at room temperature on a PANalytical X'Pert PRO diffractometer working in the Bragg–Brentano geometry using a CuKα (40 kV, 40 mA) radiation. To avoid a strong reflection from the Si (100) substrate, a slightly asymmetrical diffraction geometry with an ω-offset of 1.5° was used. Samples were scanned over the 2θ-range from 8° to 108°.

The depth profiles of optical constants (shown for the coatings 3 and 4) were determined by variable angle spectroscopic ellipsometry using the J.A. Woollam Co. Inc. instrument. The measurements were performed at wavelengths from 300 to 2000 nm using angles of incidence of 65°, 70° and 75° in reflection. The optical data were fitted using the WVASE software. The coatings 3 and 4 were described by an optical model including the Si substrate (formally included independently of the film transmittance), a gradient layer and a surface roughness layer. The gradient layer was represented by a Bruggemann mixture of metallic suboxide (described by a combination of Lorentz oscillators) and ZrO_2 (described by the Cauchy dispersion formula) with the ZrO_2 fraction monotonically increasing from 0% at the bottom to 100% at the top. The depth profile of the ZrO_2 fraction was fitted using 6 nodes with linear changes (5 slices) between neighboring nodes. In this model, the top part of the gradient layer represents the 400 nm thick top ZrO_2 film, the next part of the gradient layer represents the top (transparent) part of the ZrO_x gradient interlayer and the metallic suboxide represents the (almost opaque) bottom of the ZrO_x interlayer (the depth profile of optical constants inside the bottom part of the interlayer is not discussed because of its low transmittance). The optical constants (refractive index, n, and extinction coefficient, k) are shown and discussed at specific wavelengths given in the subscript (e.g. n_{550} and k_{550}, respectively, for 550 nm).

The coating hardness, *H*, and the effective Young's modulus, $E^* = E/\left(1-\upsilon^2\right)$, where *E* and υ are the Young's modulus and the Poisson's ratio, respectively, were determined using an ultramicroindenter (Fischerscope H-100B) according to the ISO 14577-1:2002 E standard. The measurements were performed with a preset maximum load of 20 mN. The relative measurement errors, determined from 25 measurements at different places of 20 × 20 mm^2 samples, are 6 % and 4 % for the *H* and E^* values, respectively.

The coating adhesion was evaluated using a scratch tester (CSEM Revetest) equipped with a 0.8 mm radius Rockwell diamond indenter. During a scratch test, the normal load was increasing from 0 to 100 N at a loading rate of 10 N/min and a constant indenter's sliding speed of 10 mm/min. In case of the static indentation test, the normal load was increasing from 0 to 100 N with a step of 20 N, and from 100 to 200 N with a step of 50 N. The images of the scratch tracks and indentations were digitized by an image processing system consisting of the Nikon Optiphot 100S optical microscope, an RGB camera, a frame grabber card in PC and the Image-Pro plus 1.3, Ip De luxe software. The morphology of the scratch track and indentations were accentuated by means of polarized light and the Normansky differential contrast.

2. Results and discussion

In the following, we present the results obtained for reactive depositions of densified stoichiometric ZrO_2 films with gradient ZrO_x interlayers onto floating (pretreated and non-pretreated) Si and steel substrates (Table I) at low substrate temperatures (less than 150 °C) using HiPIMS with a pulsed RGFC.

First, we show and explain the discharge characteristics during the pretreatment of the substrate surface (Fig. 4) and during the controlled reactive HiPIMS of ZrO_x interlayers and stoichiometric ZrO_2 films (Figs. 5 and 6). The effect of substrate surface modification is shown in Fig. 7. Then, we present the structure of all coatings (Fig. 8), depth profiles of the refractive index, n, and the extinction coefficient, k, (both at the wavelength of 550 nm) in the ZrO_2 films with two different gradient ZrO_x interlayers (Fig.9), and the mechanical properties

of the coatings (Table II). Lastly, we evaluate the adhesion of the coatings and their resistance to cracking (Figs. 10 and 11).

2.1. Discharge characteristics

Figure 4 shows the time evolution of the magnetron target voltage, $U_t(t)$, the substrate voltage, $U_s(t)$, the target current density, $J_t(t)$, and the substrate current density, $J_s(t) = I_s(t)/A_s$, where A_s is the area of the electrically conductive part of the substrate holder (80 cm^2 in our case), during a pretreatment of the substrate surface with a peak target power density of 220 Wcm^{-2} in a 50 μs pulse and a peak substrate power density of 6 Wcm^{-2} in a 2 ms period. As can be seen in Fig. 4, the absolute value of the negative substrate voltage U_s decreased from 965 V to 620 V in a target pulse due to a rapidly decreasing impedance of the discharge plasma.

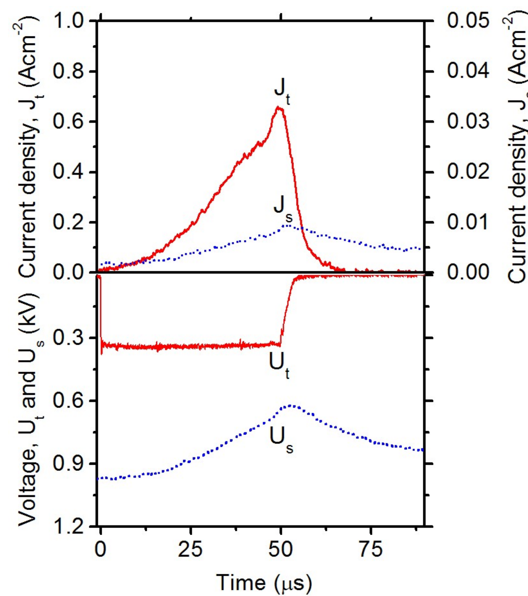

Figure 4. Waveforms of the magnetron target voltage, U_t, the substrate voltage, U_s, the target current density, J_t, and the substrate current density, J_s, during a pretreatment of the substrate surface with a peak target power density of 220 Wcm^{-2} in a pulse and a peak substrate power density of 6 Wcm^{-2} in a period.

The applied target power density is sufficiently high to enlarge substantially the fraction of Zr^+ ions and even Zr^{2+} ions in a high total ion flux (J_s up to 10 $mAcm^{-2}$) onto the highly negatively biased substrate.[23] The reason is that both first ionization energies of argon (15.76 and 15.94 eV) are greater than the very low first ionization energy of zirconium (6.63 eV) and even than the rather low second ionization energy of zirconium (13.13 eV). The zirconium ions are implanted into the substrate surface to enhance adhesion of the deposited ZrO_2-based coatings to the substrate.[24]

In contrast to a standard HiPIMS pretreatment at substrate temperatures of at least 400 °C for at least 25 min,[24,25] the substrate temperatures (less than 150 °C) are much lower and the duration of the substrate pretreatment (only 10 min) is much shorter in our case. The aim was to shorten the pretreatment process, to simplify its industrial application (no external heating) and to avoid its possible negative effects on temperature sensitive substrates.

Figures 5 and 6 show the time evolution of the magnetron target voltage, $U_t(t)$, and the target current density, $J_t(t)$, relating to the minimum (dashed lines) and maximum (solid lines) values of the $\bar{I}_t(t)$ at the beginning of the controlled reactive sputter depositions of the

gradient ZrO_x interlayers, when x ≃ 0, with $\langle S_t \rangle = 30$ Wcm^{-2} and $t_{on} = 200$ µs, and during the depositions of the stoichiometric ZrO_2 films with $\langle S_t \rangle = 37$ Wcm^{-2} and $t_{on} = 200$ µs, respectively.

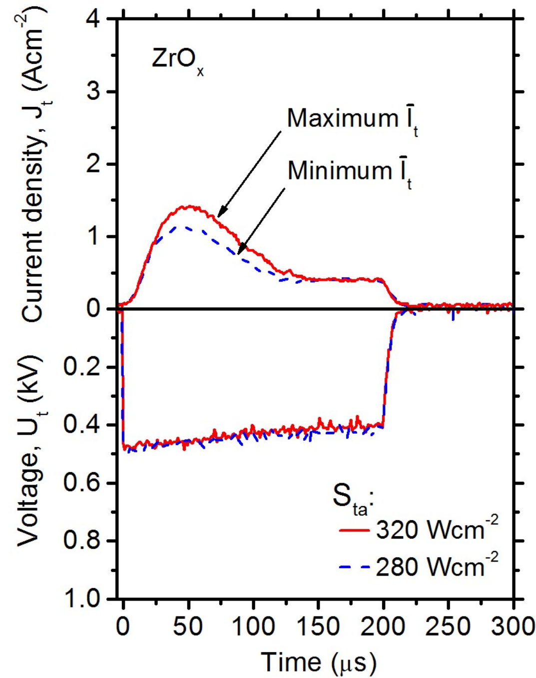

Figure 5. Waveforms of the magnetron target voltage, U_t, and the target current density, J_t, relating to the minimum (dashed lines) and maximum (solid lines) values of the average target current in a period of the power supply, $\bar{I}_t(t)$, at the beginning of controlled reactive sputter depositions of the gradient ZrO_x interlayers, when x ≃ 0, with a deposition-averaged target power density $\langle S_t \rangle = 30$ Wcm^{-2} (Figs. 2 and 3). The corresponding values of the average target power density in a pulse, S_{ta}, are also given.

As expected, smaller oscillations of $\bar{I}_t(t)$, corresponding to smaller oscillations of the oxygen density in front of the target, at the beginning of the controlled reactive sputter depositions of the gradient ZrO_x interlayers (Figs. 2 and 3) lead to a much narrower range of the average target power density in a discharge pulse, S_{ta}, being between 280 and 320 Wcm^{-2} during these depositions (Fig. 5). A higher difference in S_{ta}, from 270 to 445 Wcm^{-2} during the controlled depositions of the stoichiometric ZrO_2 films (Fig. 6) is a consequence of bigger oscillations of the oxygen density in front of the target. These are caused by the pulses of the RGFC ensuring a sufficiently high incorporation of the oxygen atoms into the films (stoichiometric ZrO_2 composition) at a minimized arcing on the compound part of the metal target and a maximized deposition rate of films (low compound fraction in the target surface layer). Let us note that a higher oxygen density in front of the target results in a higher target current density mainly due to an increasing secondary-electron emission coefficient of a Zr target partly covered by an oxide[26] (see the enlarged values of $J_t(t)$ at decreasing values of $U_t(t)$, caused by a consequent decrease of the plasma impedance, in Fig. 6).

As can be seen from Table I, the ZrO_2 films were deposited with a deposition rate of 48 nm/min at $\langle S_t \rangle = 37$ Wcm^{-2}. This relatively high deposition rate is a result of a low compound fraction in the target surface layer due to a strong sputtering of oxygen atoms from the target surface layer and a strong knock-on implantation of oxygen atoms from the target surface layer into the target bulk layer during the feed-back-controlled process.[27]

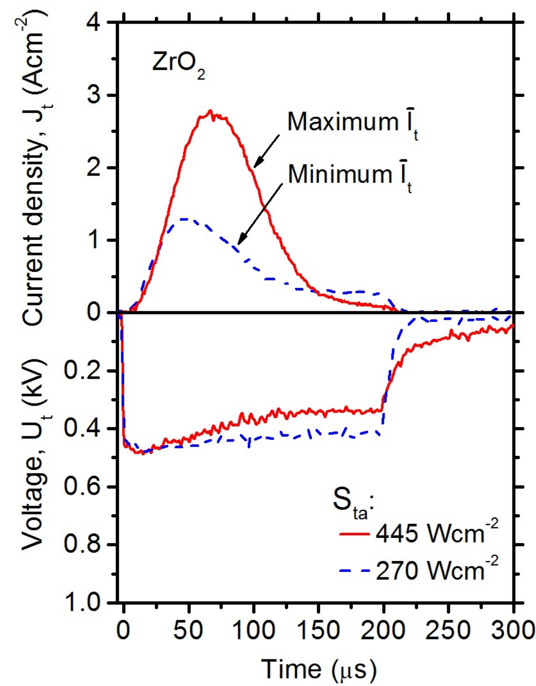

Figure 6. Waveforms of the magnetron target voltage, U_t, and the target current density, J_t, relating to the minimum (dashed lines) and maximum (solid lines) values of the average target current in a period of the power supply, $\bar{I}_t(t)$, during depositions of the stoichiometric ZrO_2 films with a deposition-averaged target power density $\langle S_t \rangle = 37$ Wcm^{-2} (Figs. 2 and 3). The corresponding values of the average target power density in a pulse, S_{ta}, are also given.

2.1. Coating structure and properties

Figure 7 shows that the relatively short (10 min) HiPIMS pretreatment of the Si (100) substrate, performed without an external heating of the substrate (the substrate temperature less than 150 °C) under the discharge conditions presented in Fig. 4, resulted in etching of the substrate surface (14 nm) and in implantation of zirconium ions into the substrate at an increased roughness of the substrate surface from $R_a = 0.2$ to 2 nm. No amount of argon was detected in the modified substrate surface.

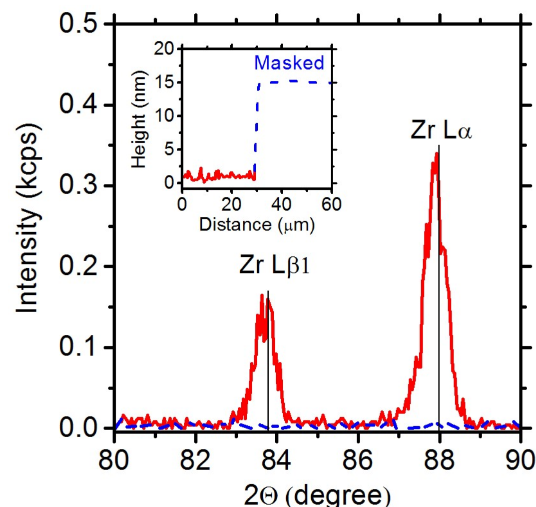

Figure 7. X-ray fluorescence patterns taken from a pretreated part (solid lines) and masked part (dashed line) of the Si substrate (Table I). The inset shows the etching depth of 14 nm.

Formation of a metal implantation zone without an incorporation of argon atoms at a coating-substrate interface is of key importance for adhesion of subsequently deposited coatings to the substrates, as discussed in detail for CrN/NbN coatings on steel substrates in Ref. 24. As shown in Table II, the pretreatment of the steel substrates was found to be a necessary condition for the adhesion of the zirconium oxide (both pure ZrO_2 and ZrO_2 + ZrO_x interlayer) films to these substrates in our case.

TABLE II. The hardness, *H*, the effective Young's modulus, *E**, and the residual macrostress, *σ*, for the coatings deposited onto Si and steel substrates.

Coating number	1	2	3	4	5
H, GPa (Si)	15	17	15	16	15
E*, GPa (Si)	160	165	160	170	165
H, GPa (Steel)	Delaminated	16	16	15	Delaminated
E*, GPa (Steel)	Delaminated	175	175	170	Delaminated
σ, GPa (Si)	- 1.3	- 1.7	- 0.8	- 0.8	- 0.8

X-ray diffraction patterns taken from the coatings deposited onto Si substrates (Tables I and II) are presented in Fig.8. They indicate a nanocrystalline structure of all the coatings. The coatings 1 and 2, formed only by the stoichiometric ZrO_2 films, are nanocrystalline with a predominant monoclinic phase (m-ZrO_2, Card No. 37-1484 in Ref. 28) and trace amount of the tetragonal (t-ZrO_2, Card No. 42-1164 in Ref. 28) or cubic (c-ZrO_2, Card No. 04-005-9865 in Ref. 28) phase, which are hard to distinguish. The amount of the tetragonal and/or cubic phase is much higher in the coatings 3 and 4 with the gradient ZrO_x interlayers, and particularly in the coating 5 formed only by a gradient ZrO_x layer.

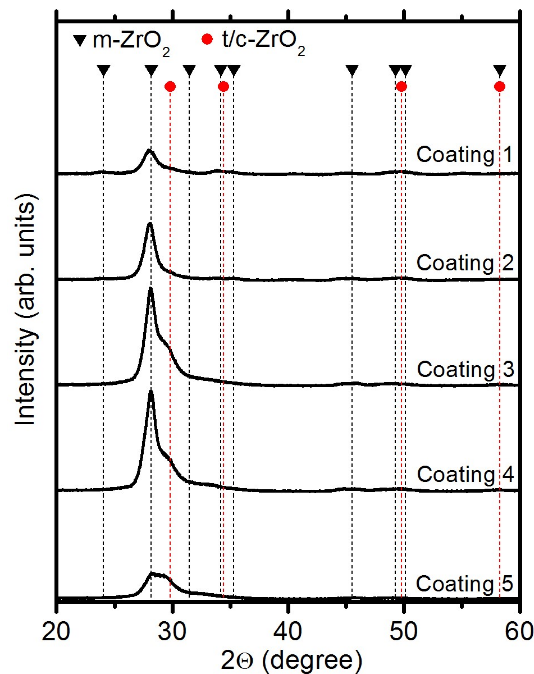

Figure 8. X-ray diffraction patterns taken from the coatings deposited onto Si substrates (Table I). The main diffraction peaks of monoclinic (m-ZrO_2, Card No. 00-037-1484 in Ref. 28) and tetragonal (t-ZrO_2, Card No. 00-042-1164 in Ref. 28) or cubic (c-ZrO_2, Card No. 04-005-9865 in Ref. 28) phase are marked. The m-ZrO_2 (-111) diffraction peak is at the position $2\Theta = 28.17°$.

Taking into account that the coatings 3-5 include the gradient ZrO_x interlayers with an increasing x from x ≃ 0 to 2 (see Fig. 9), our results are in agreement with Ref. 29, where the overlapping t-ZrO_2 and c-ZrO_2 diffraction peaks were identified as the peaks belonging to the c-ZrO_2 phase and the occurrence of this phase was correlated with O vacancies in the ZrO_2 lattice, i.e. with under-stoichiometry of the films.

Figure 9 shows the depth profiles of n_{550} and k_{550} in the coatings 3 and 4 (Table I), formed by a top ZrO_2 film (400 nm) and two different [$(\bar{I}_t)_{cr}$ increases with time linearly and as tanh, respectively - see Fig. 3] gradient ZrO_x interlayers (1800 nm), which were deposited onto pretreated Si substrates. The first thing to note is the densification of the coatings expressed in terms of n_{550} = 2.21 (n_{633} = 2.20, n_{650} = 2.19) of the top stoichiometric ZrO_2. The comparison with refractive indices reported in the literature ($n_{550} \leq 2.15$,[30] $n_{650} \leq 2.18$,[31] $n_{633} \leq 2.19$, being the limit of a dependence of the refractive index on packing density[32] or $n_{550} \leq 2.22$ in Ref. 33), let alone our own previous results ($n_{550} \leq 2.21$ in Ref. 4 and $n_{550} \leq 2.22$ in Ref. 8), confirms that the films are fully densified. In parallel, the low values of k_{550} (not measurable for the top of the coatings 3 and 4, but being 4×10^{-4} for the coating 1 which is homogeneous and allows for more precise measurements) prove that the films are stoichiometric (i.e. the high n values are indeed due to the densification). With an increasing distance from the coating surface, the figure shows monotonically decreasing n_{550} and increasing k_{550}, i.e. increasingly metallic character of the material. Note that this constitutes not only an information on the optical properties of these ZrO_2-based coatings, but consequently also on depth profiles of the stoichiometric coefficient x in them. While the changes are relatively slow in the top ≈1000 nm (400 nm of ZrO_2 + ≈600 nm of ZrO_x, the top third of the 1800 nm thick ZrO_x interlayer), they become particularly fast below ≈1000 nm from the surface (i.e. in the middle third of the ZrO_x interlayer). The gradient of the changes in the middle third of the ZrO_x interlayer is slightly higher for coating 4 in agreement with the shape of the tanh function (Fig. 3).

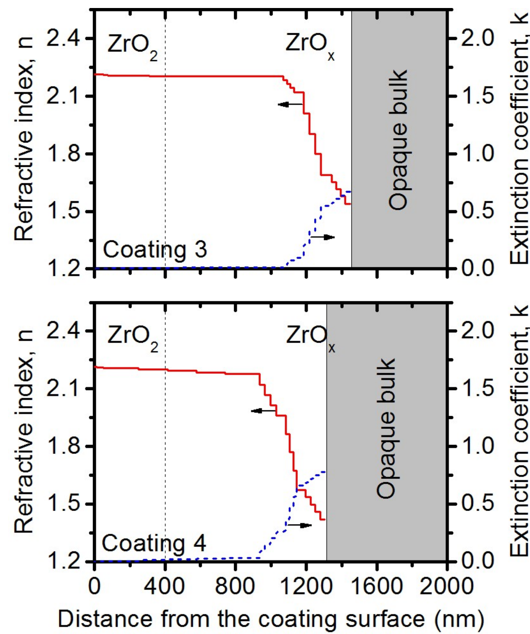

Figure 9. The refractive index, n, and the extinction coefficient, k, (both at the wavelength of 550 nm) as functions of the distance from the coating surface for the coatings 3 (upper panel) and 4 (lower panel) deposited onto pretreated Si substrates (Table I).

Mechanical properties of the coatings are presented in Table II. The coatings exhibited a high hardness H = 15-17 GPa at an effective Young's modulus E^* = 160-175 GPa, resulting in

a relatively high H/E^* ratio of 0.09-0.10 related to the material's elastic strain limit, which characterizes the ability of the material to deform elastically and recover without plastic deformation.[34] The relationship between the H/E^* ratio and the resistance to cracking was investigated, for example, in Refs. 35 and 36. The H values achieved by us are comparable even with values for Y-stabilized high-density phases of ZrO_2 ($H \leq 17$ GPa for the cubic phase in Ref. 37, $H \leq 14$ GPa for a not fully densified tetragonal phase in Ref. 38, and $H \leq 17$ GPa for the tetragonal phase densified by a slight Al doping in Ref. 38). This constitutes another confirmation that the top ZrO_2 films are densified.

As expected, coatings 3-5 with gradient ZrO_x interlayers exhibited a reduced compressive stress $\sigma = -0.8$ GPa (Table II). The complicated relationship between the residual stress of ceramic coatings on steel substrates, and their damage resistance and adhesion to the substrates was investigated, for example, in Ref. 39. Note that brittle failure and delamination of ceramic films are major problems that hinder their application as functional thin-film materials deposited onto substrates made from ductile materials.

Evaluations of the adhesion and resistance to cracking of the ZrO_2-based coatings 2-4 deposited on the pretreated steel substrates are shown in Figs. 10 and 11. Let us recall that the pretreatment of the steel substrates was a necessary condition for the adhesion of the coatings (Table II).

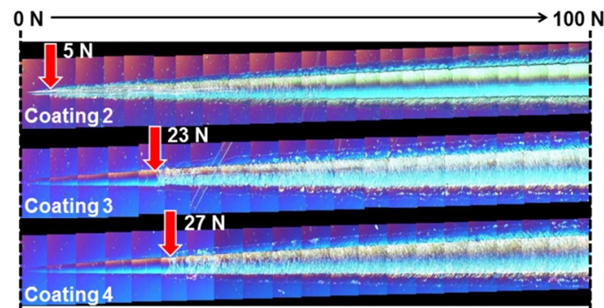

Figure 10. Optical micrographs of the scratch tracks in the coatings 2-4 deposited onto pretreated steel substrates (Table I). The values of the load when the first cracks on the coating surfaces occurred are marked by arrows.

As can be seen in Figs. 10 and 11, the adhesion of stoichiometric ZrO_2 films and their resistance to cracking are substantially higher when the gradient ZrO_x interlayers (coatings 3 and 4) are applied. In particular, the critical load corresponding to the first cracks during the scratch test (Fig. 10) increased from 5 N to 23-27 N, and the critical load corresponding to the first delaminations during the static indentation test (Fig. 11) increased from 80 N over the 200 N measurement limit. The better performance of the coating 4 compared to the coating 3 during the scratch test (critical load of 27 N compared to 23 N) is consistent with the slower compositional changes (slower increase in x) in the vicinity of the coating-substrate interface - see the shape of the tanh function in Fig. 3, and the thicker bottom opaque part of the interlayer in Fig. 9. Here, it should be recalled that the substrate temperatures (less than 150 °C) are very low and the duration of the substrate pretreatment (10 min) is very short in comparison with a standard HiPIMS pretreatment.[24,25]

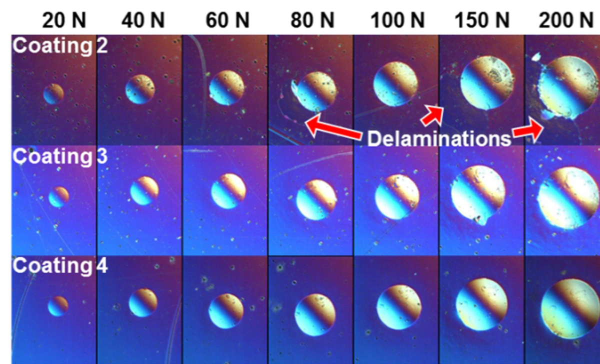

Figure 11. Optical micrographs of Rockwell indentations at an increasing load from 20 N to 200 N for the coatings 2-4 deposited onto pretreated steel substrates (Table I). Surface delaminations on the coating 2 are marked by arrows.

4. Conclusions

We present basic principles of a simple (no substrate bias voltage during reactive sputter depositions and no external heating during the whole process) three-step HiPIMS technique (substrate pretreatment, deposition of gradient ZrO_x interlayers and deposition of stoichiometric ZrO_2 films) for a fast deposition of densified stoichiometric ZrO_2 films with enhanced adhesion to steel substrates.

The first step of the technique is a short (10 min) HiPIMS pretreatment of the steel substrate at low substrate temperatures (less than 150 °C). Then, HiPIMS with the feed-back pulsed O_2 flow control[4,8] was used for depositions of the gradient ZrO_x interlayers with a controlled increase in x from $x \simeq 0$ to 2, and for depositions of the stoichiometric ZrO_2 films onto floating substrates at low substrate temperatures (less than 150 °C).

It was shown that the pretreatment of the steel substrates is a necessary condition for adhesion of the zirconium oxide (both pure ZrO_2 and ZrO_2 + ZrO_x interlayer) films and that the adhesion of the ZrO_2 films is substantially higher when the gradient ZrO_x interlayers are applied. The densified stoichiometric ZrO_2 films deposited onto the gradient ZrO_x interlayers exhibited a high hardness (15-16 GPa) and an enhanced resistance to cracking.

Acknowledgment

This work was supported by the Czech Science Foundation under Project No. GA14-03875S.

References

1 K. Sarakinos, J. Alami, and S. Konstantinidis, Surf. Coat. Technol. 204, 1661 (2010).
2 D. Lundin and K. Sarakinos, J. Mater. Res. 27, 780 (2012).
3 M. Hála, J. Čapek, O. Zabeida, J. E. Klemberg-Sapieha, and L. Martinu, J. Phys. D: Appl. Phys. 45, 055204 (2012).
4 J. Vlček, J. Rezek, J. Houška, T. Kozák, and J. Kohout, Vacuum 114, 131 (2015).
5 J. P. Fortier, B. Baloukas, O. Zabeida, J. E. Klemberg-Sapieha, and L. Martinu, Sol. Energy Mater. Sol. Cells. 125, 291 (2014).
6 A. Aijaz, Y. X. Ji, J. Montero, G. A. Niklasson, C. G. Granqvist, and T. Kubart, Sol. Energy Mater. Sol. Cells. 149, 137 (2016).
7 S. Zenkin, A. Belosludtsev, Š. Kos, R. Čerstvý, S. Haviar, and M. Netrvalová, Appl. Phys. Lett. 108, 231602 (2016).

[8] J. Vlček, J. Rezek, J. Houška, R. Čerstvý, and R. Bugyi, Surf. Coat. Technol. 236, 550 (2013).
[9] J. Vlček, A. Belosludtsev, J. Rezek, J. Houška, J. Čapek, R. Čerstvý, and S. Haviar, Surf. Coat. Technol. 290, 58 (2016).
[10] J. Rezek, J. Vlček, J. Houška, and R. Čerstvý, Thin Solid Films 566, 70 (2014).
[11] I. Safi, Surf. Coat. Technol. 127, 203 (2000).
[12] W. D. Sproul, D. J. Christie, and D. C. Carter, Thin Solid Films 491, 1 (2005).
[13] L. Xikun, L. Jing, Q. Like, C. Tong, Q. Guanming, and S. Yanbin, J. Rare Earths 25, 287 (2007).
[14] G. L. Tan and X. J. Wu, Thin Solid Films 330, 59 (1998).
[15] H. Hsu and S. Yen, Dent. Mater. 14, 339 (1998).
[16] G. Soon, B. Pingguan-Murphy, K. W. Lai, and S. A. Akbar, Ceram. Int. 42, 12543 (2016).
[17] P. Ducheyne, K. E. Healy, D.W. Hutmacher, D. W. Gradinger, and C. J. Kirkpatrick, Comprehensive Biomaterials (Elsevier, Netherlands, 2011), pp.117-136.
[18] S. Yen, M. Guo, and H. Zan, Biomaterials 22, 125 (2001).
[19] V. K. Balla, W. Xue, S. Bose, and A. Bandyopadhyay, Acta Biomater. 5, 2800 (2009).
[20] J. Wang, H. P. Li, and R. Stevens, J. Mater. Sci. 27, 5397 (1992).
[21] P. Kudláček, J. Vlček, K. Burcalová, and J. Lukáš, Plasma Sources Sci. Technol. 17, 025010 (2008).
[22] J. Gunnars and U. Wiklund, Mater. Sci. Eng. A, 336, 7 (2002).
[23] J. Lazar, J. Vlček, and J. Rezek, J. Appl. Phys. 108, 063307 (2010).
[24] A. P. Ehiasarian, J. G. Wen, and I. Petrov, J. Appl. Phys. 101, 054301 (2007).
[25] M. Lattemann, A. P. Ehiasarian, J. Bohlmark, P. Å. O. Persson, and U. Helmersson, Surf. Coat. Technol. 200, 6495 (2006).
[26] D. Depla, S. Heirwegh, S. Mahieu, J. Haemers, and R. De Gryse, J. Appl. Phys. 101, 013301 (2007).
[27] T. Kozák and J. Vlček, J. Phys. D: Appl. Phys. 49, 055202 (2016).
[28] JCPDS-ICDD, PDF-4+ Database, International Centre for Diffraction Data, Newton Square, PA, USA, 2015.
[29] M. Raza, D. Cornil, J. Cornil, S. Lucas, R. Snyders, and S. Konstantinidis, Scripta Mater. 124, 26 (2016).
[30] D. Franta, I. Ohlídal, P. Klapetek, P. Pokorný, and M. Ohlídal, Surf. Interface Anal. 32, 91 (2001).
[31] K. Juskevicius, M. Audronis, A. Subacius, R. Drazdys, R. Juskenas, A. Matthews, and A. Leyland, Appl. Phys. A 116, 1229 (2014).
[32] S. Ben Amor, B. Rogier, G. Baud, M. Jacquet, and M. Nardin, Mat. Sci. Eng. B 57, 28 (1998).
[33] H. H. Zhang, C. Y. Ma, and Q. Y. Zhang, Vacuum 83, 1311 (2009).
[34] A. Leyland and A. Matthews, Wear 246, 1 (2000).
[35] J. Musil, J. Sklenka, and R. Čerstvý, Surf. Coat. Technol. 206, 2105 (2012).
[36] H. K. Kim, J. H. La, K. S. Kim, and S. Y. Lee, Surf. Coat. Technol. 284, 230 (2015).
[37] P. Yashar, J. Rechner, M. S. Wong, W. D. Sproul, and S. A. Barnett, Surf. Coat. Technol. 94, 333 (1997).
[38] O. Vasylkiv, Y. Sakka, and V. V. Skorokhod, Mater. Trans. JIM 44, 2235 (2003).
[39] M. S. Ahmed, Z. F. Zhou, P. Munroe, L. K. Y. Li, and Z. Xie, Thin Solid Films, 519, 5007 (2011).

IV. Conclusions of the thesis

The present Ph.D. thesis reports on the results obtained in the laboratory of the Department of Physics at the University of West Bohemia in the years 2013-2016. The results presented in chapter III fulfil all the aims formulated.

A. High-power impulse magnetron sputtering (HiPIMS) with a pulsed reactive gas (oxygen) flow control was used for high-rate reactive depositions of densified, highly optically transparent, stoichiometric HfO_2 films onto floating substrates at the distance of 100 mm from the target. It was shown that the HfO_2 films can be prepared with very high deposition rates (up to 200 nm/min) at a deposition-averaged target power density of approximately 30 Wcm^{-2}, which is relatively close to a target power density applicable in industrial HiPIMS systems. The films were nanocrystalline with a dominant monoclinic phase. They exhibited a hardness of 15-18 GPa, a refractive index of 2.07-2.12 and an extinction coefficient between $\leq 0.1\times10^{-3}$ and 0.6×10^{-3} (both quantities at the wavelength of 550 nm). At 300 nm, the extinction coefficient was between 1.5×10^{-3} and 7.0×10^{-3}. A simplified relation for the deposition rate of films prepared by a reactive HiPIMS was presented and used to qualitatively explain the dependences and very high values measured for the deposition rate of the HfO_2 films..

B. Reactive high-power impulse magnetron sputtering with a pulsed reactive gas (oxygen) flow control was used to deposit HfO_2 films on Si substrates. The effect of the voltage pulse duration, t_1, and deposition-averaged target power density, $<S_d>$, on their microstructure was studied by high-resolution transmission electron microscopy. Four HfO_2 films were prepared with (1) T100S7: $t_1 = 100$ µs, $<S_d> = 7.2$ Wcm^{-2}; (2) T200S7: $t_1 = 200$ µs, $<S_d> = 7.3$ Wcm^{-2}; (3) T200S18: $t_1 = 200$ µs, $<S_d> = 18$ Wcm^{-2} and (4) T200S54: $t_1 = 200$ µs, $<S_d> = 54$ Wcm^{-2}. All films were composed of an interlayer with the Si substrate followed by a nano-columnar structure layer. Thus, the results show that the reactive gas flow control can be used to deposit vertically homogeneous films (without any multilayered structure which could hypothetically result from the O_2 flow pulsing). Decreasing $<S_d>$ and t_1, was found to reduce the width of the columns, increase the thickness of the grain boundaries and thickness of the interlayer. Films prepared with a large t_1 (T200S54, T200S18 and T200S7) exhibited a m-HfO_2 structure, while that with a smaller t_1 (T100S7) exhibited a mixture of m- and o-HfO_2 phases. The hardness of films was 13-18 GPa with those of a monoclinic structure possessing the highest hardness (17-18 GPa). The films exhibited a refractive index of 2.02-2.11 and an extinction coefficient between $0.1\text{x}10^{-3}$ and $1\text{x}10^{-3}$ (both at a wavelength of 550 nm). The highest refractive index was achieved for films T200S54 and T200S18 that exhibited denser microstructures with atomically sharp and tightly interlocking grain boundaries.

C. Thickness dependent wetting properties were measured for the intrinsically hydrophobic HfO_2 thin films prepared by reactive high-power impulse magnetron sputtering. The van Oss-Good-Chaudhury approach used shows that surface free energy

of HfO_2 is ≈ 99% electrostatic in nature for all thicknesses. This dominance of the electrostatic Lifshitz-van der Waals component of the surface energy allows to control the value of the contact angle with water in the range 100º-120º by the variation of the film thickness in the range 50-250nm. FTIR-ATR measurements show that the wetting properties are qualitatively the same for all HfO_2 films of different thicknesses. Combining these results with XRD and SEM measurements were suggested two mechanisms of surface energy thickness dependence: influence of non-dominant texture and/or non-monotonic size dependence of the particle surface energy. Surfaces with controlled wettability might find various applications such as substrates for controlled morphology of spin-coated films.

D. Hafnium oxynitride films were prepared in a one-step process by high-power impulse magnetron sputtering at a low deposition temperature (<140 °C) and without using substrate bias. Feedback pulsed reactive gas flow control made it possible to achieve very high deposition rates (up to 230 nm/min) and smoothly controlled composition from $Hf_{32}O_{66}$ to $Hf_{57}O_6N_{33}$. Special attention was paid to compositions with low N contents. All films were nanocrystalline. Increasing the N content in the films allowed us to control the film structure, from m-HfO_2 through t/c-HfO_2 (dominant phase at 4-8 at.% N in the films) and c-$HfN_{0.6}O_{0.4}$ to c-HfN. The evolution of smoothly controlled films properties along the transition from HfO_2 to HfN includes, for example, extinction coefficient at 550 nm from 5×10^{-4} to 1.77, electrical resistivity from $>10^8$ Ωm to 3.2×10^{-6} Ωm, hardness from 18 GPa to 25 GPa or water droplet contact angle from 101° to 107°. The results are important for designing oxynitride coatings, and pathways for their preparation, for various technological applications.

E. Basic principles of a simple (no substrate bias voltage during reactive sputter depositions and no external heating during the whole process) three-step HiPIMS technique (substrate pretreatment, deposition of gradient ZrO_x interlayers and deposition of stoichiometric ZrO_2 films) for a fast deposition of densified stoichiometric ZrO_2 films with enhanced adhesion to steel substrates were presented. The first step of the technique is a short (10 min) HiPIMS pretreatment of the steel substrate at low substrate temperatures (less than 150 °C). Then, HiPIMS with the feed-back pulsed O_2 flow control was used for depositions of the gradient ZrO_x interlayers with a controlled increase in x from x ≃ 0 to 2, and for depositions of the stoichiometric ZrO_2 films onto floating substrates at low substrate temperatures (less than 150 °C). It was shown that the pretreatment of the steel substrates is a necessary condition for adhesion of the zirconium oxide (both pure ZrO_2 and ZrO_2 + ZrO_x interlayer) films and that the adhesion of the ZrO_2 films is substantially higher when the gradient ZrO_x interlayers are applied. The densified stoichiometric ZrO_2 films deposited onto the gradient ZrO_x interlayers exhibited a high hardness (15-16 GPa) and an enhanced resistance to cracking.

V. Further publications of the candidate

1. Papers in international journals

[1] N. Britun, **A. Belosludtsev**, T. Silva, R. Snyders
"*Ground state atomic oxygen in high-power impulse magnetron sputtering: a quantitative study*"
J. Phys. D: Appl. Phys. (2017) (accepted).

[2] N. Britun, S. Konstantinidis, **A. Belosludtsev**, T. Silva, R. Snyders
"*Quantitative study of reactive HIPIMS discharge: the dynamics of the O ground state atoms*"
J. Appl. Phys. (2017) (accepted).

2. Oral and poster presentations at international conferences

[1] J. Rezek, J. Vlček, **A. Belosludtsev** "*Different process parameters controlling reactive high-power impulse magnetron sputtering of dielectric oxide films*" International Conference on Power Electronics for Plasma Engineering, 20.- 22. 05. 2014, Warsaw/Zielonka, Poland (co-author of the oral presentation).

[2] J. Rezek, J. Vlček, **A. Belosludtsev** "*Different process parameters controlling reactive high-power impulse magnetron sputtering of dielectric oxide films*" 5th International Conference on Fundamentals and Industrial Applications of HiPIMS 30. 6. - 3. 7. 2014, Sheffield, UK (co-author of the oral presentation).

[3] **A. Belosludtsev**, J. Rezek, J. Vlček, J. Houška, R. Čerstvý "*High-rate reactive high-power impulse magnetron sputtering of hafnium dioxide films*" 14th International Conference on Plasma Surface Engineering, 15.- 19. 09. 2014, Garmisch-Partenkirchen, Germany (author of the poster).

[4] J. Rezek, J. Vlček, **A. Belosludtsev** "*Different process parameters controlling reactive high-power impulse magnetron sputtering of dielectric oxide films*" 14th International Conference on Plasma Surface Engineering, 15.- 19. 09. 2014, Garmisch-Partenkirchen, Germany (co-author of the poster).

[5] **A. Belosludtsev**, J. Rezek, J. Vlček, J. Houška, R. Čerstvý "*High-rate reactive high-power impulse magnetron sputtering of hafnium dioxide films*" 13th International Conference on Reactive Sputter Deposition, 11.- 12. 12. 2014, Ghent, Belgium (author of the poster).

[6] J. Rezek, J. Vlček, **A. Belosludtsev** "*Controlled reactive high-power impulse magnetron sputtering of dielectric oxide films*" 13th International Conference on Reactive Sputter Deposition, 11.- 12. 12. 2014, Ghent, Belgium (co-author of the poster).

[7] J. Rezek, J. Vlček, **A. Belosludtsev** "*Controlled Reactive High-Power Impulse Magnetron Sputtering of Dielectric Oxide Films*" 58th Annual Society of Vacuum Coaters Technical Conference, 25.- 30. 4. 2015, Santa Clara, USA (co-author of the oral presentation).

[8] J. Vlček, J. Rezek, **A. Belosludtsev** "*Pulsed reactive gas flow control for high-power impulse magnetron sputtering of oxide and oxynitride films*" International Conference on Power Electronics for Plasma Engineering, 20.- 22. 05. 2015, Ditzingen, Germany (co-author of the invited oral presentation).

[9] **A. Belosludtsev**, J. Vlček, J. Houška, S. Haviar, R. Čerstvý, J. Rezek "*Reactive high-power impulse magnetron sputtering of ZrO_2 films with gradient ZrO_x interlayers on pretreated steel substrates*" Ion processing and Arc Technologies European Conference, 14th International Symposium on Reactive Sputter Deposition, 8.- 11. 12. 2015, Paris, France (author of the oral presentation).

[10] J. Vlček, J. Rezek, **A. Belosludtsev**, T. Kozak "*High-rate reactive high-power impulse magnetron sputtering of oxide films*" 4th Magnetron, Ion processing and Arc Technologies European Conference, 14th International Symposium on Reactive Sputter Deposition, 8.- 11. 12. 2015, France (co-author of the oral presentation).

[11] **A. Belosludtsev**, J. Vlček, J. Houška, S. Haviar, R. Čerstvý, J. Rezek "*Reactive High-power Impulse Magnetron Sputtering of ZrO_2 Films with Gradient ZrO_x Interlayers on Pretreated Steel Substrates*" 43nd International Conference on Metallurgical Coatings and Thin Films 25.- 29. 4. 2016, San Diego, USA (author of the oral presentation).

[12] S. Zenkin, **A. Belosludtsev**, Š. Kos, R. Čerstvý, S. Haviar, M. Netrvalová "*Thickness dependent wetting properties of thin films of ceramics based on low-electronegativity metals*" European Materials Research Society 2.- 6. 5. 2016, Lille, France (co-author of the oral presentation).

[13] J. Vlček, J. Rezek, **A. Belosludtsev**, T. Kozák "*High-Rate Reactive High-Power Impulse Magnetron Sputter Deposition: Principles and Applications*" 59th Annual Society of Vacuum Coaters Technical Conference 9.- 13. 5. 2016, Indianapolis, USA (co-author of the oral presentation).

[14] J. Vlček, J. Rezek, **A. Belosludtsev**, T. Kozák "*High-Rate Reactive High-Power Impulse Magnetron Sputter Deposition: Principles and Applications*" 59th Annual Society of Vacuum Coaters Technical Conference Proceedings, Indianapolis, USA, doi: http://dx.doi.org/10.14332/svc16.proc.0006 (co-author of the conference proceedings).

[15] **A. Belosludtsev**, S. Zenkin, Š. Kos, "*Thickness dependent wetting properties of thin stoichiometric hafnium oxide films*" Student scientific conference of Faculty of Applied Science 19. 5. 2016, Plzeň, Czech Republic (author of the oral presentation).

[16] **A. Belosludtsev**, J. Vlček, J. Houška, S. Haviar, R. Čerstvý, J. Rezek "*Reactive high-power impulse magnetron sputtering of ZrO_2 films with gradient ZrO_x interlayers on pretreated steel substrates*" 4th International Workshop and the 3rd International Mini Workshop on Solution Plasma and Molecular Technology 7.- 11. 6. 2016, Plzeň, Czech Republic (author of the oral presentation).

[17] S. Zenkin, Š. Kos, J. Musil, **A. Belosludtsev**, R. Čerstvý, S. Haviar, M. Netrvalová "*Low-electronegativity metal-based hydrophobic hard ceramics*" 4th International Workshop and the 3rd International Mini Workshop on Solution Plasma and Molecular Technology 7.- 11. 6. 2016, Plzeň, Czech Republic (co-author of the oral presentation).

[18] **A. Belosludtsev**, J. Vlček, S. Haviar, J. Houška, R. Čerstvý, J. Rezek "*Reactive high-power impulse magnetron sputtering of Hf-O-N films with tunable composition and properties*" Symposium on Plasma Physics and Technology 20.- 23. 06. 2016, Prague, Czech Republic (author of the oral presentation).

[19] **A. Belosludtsev**, J. Vlček, S. Haviar, J. Houška, R. Čerstvý, J. Rezek "*High-rate reactive high-power impulse magnetron sputtering of Hf-O-N films with tunable composition and properties*" 7th International Conference on Fundamentals and Industrial Applications of HiPIMS 27.- 30. 06. 2016 Sheffield, UK (author of the oral presentation).

[20] S. Zenkin, **A. Belosludtsev**, Š. Kos, R. Čerstvý, S. Haviar, M. Netrvalová "*Thickness dependent wetting properties of thin films of ceramics based on low-electronegativity metals*" 15th International Conference on Plasma Surface Engineering 12.- 16. 09. 2016, Garmisch-Partenkirchen, Germany (co-author of the poster).

[21] **A. Belosludtsev**, J. Vlček, S. Haviar, J. Houška, R. Čerstvý, J. Rezek "*High-rate reactive high-power impulse magnetron sputtering of Hf-O-N films with tunable composition and properties*" 15th International Conference on Plasma Surface Engineering 12.- 16. 09. 2016, Garmisch-Partenkirchen, Germany (author of the oral presentation).

[22] N. Britun, S. Konstantinidis, **A. Belosludtsev**, T. Silva, R. Snyders *"Quantitative study of reactive HIPIMS discharge: the dynamics of the O ground state atoms"* 15th International Conference on Reactive Sputter Deposition, 1.- 2. 12. 2016, Ghent, Belgium (co-author of the oral presentation).

[23] **A. Belosludtsev**, J. Vlček, J. Houška, R. Čerstvý, J. *"Reactive high-power magnetron sputtering of Al-O-N films with tunable composition and properties"* 15th International Conference on Reactive Sputter Deposition, 1.- 2. 12. 2016, Ghent, Belgium (author of the oral presentation).

[24] J. Vlček, **A. Belosludtsev,** S. Haviar, J. Houška, R. Čerstvý, J. Rezek, "*High-rate Reactive High-power Impulse Magnetron Sputtering of Hf-O-N Films with Tunable Composition and Properties*" 44th International Conference on Metallurgical Coatings and Thin Films 24.- 28. 4. 2017, San Diego, USA (co-author of the oral presentation).

[25] N. Britun, **A. Belosludtsev**, S. Konstantinidis, A. Hecimovic, R. Snyders, "*In-situ diagnostics of high-power impulse magnetron sputtering: from non-reactive sputtering and spokes to reactive sputtering*" 14th International Symposium on Sputtering and Plasma Processes 5.- 7. 7. 2017, Kanazawa, Japan (co-author of the oral presentation).

Abstract

Transition metal oxides and oxynitrides are a class of materials with yet unexplored physical, chemical and functional properties, and a great potential for industrial applications. This Ph.D. thesis deals with preparation and characterization of multifunctional oxide and oxynitride films. They were prepared using high-power impulse magnetron sputtering with a feedback pulsed reactive gas flow control. The thesis is divided into six chapters.

Chapter I is devoted to a short general introduction into problematics. In Chapter II, the aims are defined. Chapter III is the most extensive and is devoted to the results achieved in this thesis. This chapter is divided in five parts presented in a form of scientific papers published (A-C) or submitted for publication (D-E) in prestigious international journals.

In Part A, the deposition of densified, hard (15-18 GPa), highly optically transparent (refractive index of 2.07-2.12 and extinction coefficient between $\leq 0.1\times10^{-3}$ and 0.6×10^{-3}; both quantities at the wavelength of 550 nm), stoichiometric HfO_2 films onto floating silicon substrates is reported. Influence of the deposition conditions (pulse duration of 50-200 μs and deposition-averaged target power density of 29-54 Wcm^{-2}) on deposition rates (up to 345 and 460 nm/min for HfO_2 and pure Hf, respectively) and on film properties was discussed. A simplified relation for the deposition rate was presented.

In Part B, microstructure of densified, hard (17-18 GPa), highly optically transparent (refractive index of 2.02-2.11 and extinction coefficient between 0.1×10^{-3} and 1×10^{-3}; both quantities at the wavelength of 550 nm), smooth (maximum average mean roughness of about 1 nm) HfO_2 films onto floating silicon substrates was presented. The effect of the voltage pulse duration (50-200 μs) and the deposition-averaged target power density (7.3-54 Wcm^{-2}) on their microstructure was investigated. All films were found to be composed of an interlayer next to the substrate interface followed by a nano-columnar structure layer. In one film, high temperature orthorhombic HfO_2 phase was found.

In Part C, the dependence of wetting properties and surface free energy of HfO_2 films on their thickness is investigated. In the range of 50–250 nm, the strongest dependence (increase of the water droplet contact angle up to 120°) due to the dominance of the electrostatic Lifshitz-van der Waals component of the surface free energy was found. At the same time, the surface free energy grows from about 25 mJ/m^2 for the thickness of 50 nm to about 33 mJ/m^2 for the thickness of 2300 nm. It was proposed two explanations for the observed thickness dependence of the wetting properties: influence of the non-dominant texture and/or non-monotonic size dependence of the particle surface energy.

In Part D, the relationships between elemental composition, phase structure, and optical, electrical, mechanical and hydrophobic properties of the Hf-O-N films are shown. The films were prepared at nitrogen fractions in the average reactive gas flow of 0, 0.9, 2.6, 5, 25, 50 and 100%. The smoothly controlled composition is shown in terms of smoothly controlled material properties along the transition from an oxide to a nitride including, for example, extinction coefficient at 550 nm from 5×10^{-4} to 1.77, electrical resistivity from $>10^8$ Ωm to 3.2×10^{-6} Ωm, hardness from 18 GPa to 25 GPa or water droplet contact angle from 101° to 107°.

In Part E, the basic principles of a simple (no substrate bias voltage during reactive sputter depositions and no external heating during the whole process) three-step HiPIMS technique (substrate pretreatment, deposition of gradient ZrO_x interlayers and deposition of stoichiometric ZrO_2 films) for a fast deposition of densified stoichiometric ZrO_2 films with enhanced adhesion to steel substrates are presented and discussed.

Chapter IV is devoted to the conclusions of the Ph.D. thesis. In Chapter V, further publications of the candidate are given.

Resumé česky

Oxidy a oxynitridy přechodových kovů jsou třídou materiálů s ještě neprozkoumanými fyzikálními, chemickými a funkčními vlastnostmi a s velkým potenciálem pro průmyslové aplikace. Tato disertační práce se zabývá přípravou a charakterizací multifunkčních oxidových a oxynitridových vrstev. Pro přípravu vrstev bylo použito vysokovýkonové pulzní reaktivní magnetronové naprašování se zpětnovazebním pulzním řízením průtoku reaktivního plynu. Práce je rozdělena do šesti kapitol.

Kapitola I je věnována stručnému všeobecnému úvodu do problematiky. V kapitole II jsou definovány cíle disertační práce. Kapitola III je nejrozsáhlejší a je věnována výsledkům dosaženým v této práci. Tato kapitola je rozdělena do pěti částí prezentovaných v podobě vědeckých prací publikovaných (A–C) nebo předložených k publikaci (D–E) v prestižních mezinárodních časopisech.

V části A je prezentována depozice hustých, tvrdých (15–18 GPa), vysoce opticky transparentních (index lomu 2,07–2,12 a extinkční koeficient mezi $0{,}1\times10^{-3}$ a $0{,}6\times10^{-3}$; obě veličiny při vlnové délce 550 nm), stechiometrických vrstv HfO_2 na křemíkové substráty na plovoucím potenciálu. Je diskutován vliv depozičních podmínek (délka pulzu 50–200 μs a průměrná hustota výkonu na terč 29–54 Wcm^{-2}) na depoziční rychlost (až 345 a 460 nm/min pro HfO_2 a Hf v uvedeném pořadí) a na vlastnosti vrstev. Je představen zjednodušený vztah pro depoziční rychlost.

V části B je diskutována mikrostruktura hustých, tvrdých (17–18 GPa), vysoce opticky transparentních (index lomu 2,02–2,11 a extinkční koeficient mezi $0{,}1\times10^{-3}$ a 1×10^{-3}; obě veličiny při vlnové délce 550 nm), hladkých (maximální průměrná střední drsnost asi 1 nm) HfO_2 vrstev, připravených na křemíkových substrátech na plovoucím potenciálu. Byl zkoumán vliv délky pulzu (50–200 μs) a průměrné hustoty výkonu na terč (7,3–54 Wcm^{-2}) na jejich mikrostrukturu. Bylo zjištěno, že všechny vrstvy se skládají z přechodové mezivrstvy na substrátu následované vrstvou vykazující nanosloupcovou strukturu. V jedné vrstvě byla zjištěna vysokoteplotní ortorombická fáze HfO_2.

V části C je zkoumána závislost smáčivosti a volné povrchové energie HfO_2 vrstev na jejich tloušťce. V rozmezí 50–250 nm je pozorována nejsilnější závislost (zvýšení kontaktního úhlu kapky vody až na 120°) díky dominanci elektrostatické Lifshitzovy – van der Waalsovy složky povrchové volné energie. Zároveň povrchová volná energie roste od přibližně 25 mJ/m^2 při tloušťce 50 nm do přibližně 33 mJ/m^2 při tloušťce 2300 nm. Byla navržena dvě vysvětlení pro závislost smáčivosti na tloušťce vrstev: vliv nedominantní textury a/nebo nemonotónní závislost povrchové energie na velikosti zrn.

V části D jsou ukázány vztahy mezi prvkovým složením, fázovou strukturou a optickými, elektrickými, mechanickými a hydrofobními vlastnostmi Hf-O-N vrstev.

Vrstvy byly připraveny při podílu dusíku v průměrném průtoku reaktivního plynu: 0, 0,9, 2,6, 5, 25, 50 a 100 %. Je ukázána plynule řízená příprava vrstev z hlediska plynule laditelných vlastností materiálu při přechodu z oxidu do nitridu. Jedná se například o změnu extinkčního koeficientu při vlnové délce 550 nm z 5×10^{-4} na 1,77, elektrického odporu z $>10^{8}$ Ωm na $3{,}2\times10^{-6}$ Ωm, tvrdosti z 18 GPa na 25 GPa nebo kontaktního úhlu kapky vody ze 101° na 107°.

V části E jsou uvedeny a diskutovány základní principy jednoduché (bez použití předpětí a externího ohřevu substrátu během celého procesu reaktivní depozice) třístupňové (předčištění substrátu, depozice gradientních mezivrstev ZrO_x a depozice stechiometrických vrstev ZrO_2) HiPIMS techniky pro rychlou depozici stechiometrických hustých vrstev ZrO_2 se zvýšenou adhezí k povrchu ocelových substrátů.

Kapitola IV je věnována závěrům disertační práce. V kapitole V jsou uvedeny další publikace kandidáta

Аннотация

Оксиды и оксинитриды переходных металлов это класс материалов с еще неизученными физическими, химическими и функциональными свойствами. Такие материалы могут найти широкое применение в промышленности. Эта диссертация на соискание ученой степени «Ph.D.» посвящена синтезу и характеризации многофункциональных оксидых и оксинитридных тонких плёнок. Они были получены методом магнетронного распыления импульсами высокой мощности с импульсным регулятором потока реактивного газа с обратной связью. Диссертация состоит из шести глав.

Глава I посвящена короткому общему введению в проблематику. В главе II сформулированы цели диссертации. Глава III самая объёмная и посвящена результатам, достигнутым в данной работе. Эта глава разделена на пять частей, представленных в виде научных статей, опубликованных (A-C) или отправленных для публикации (D-E) в престижных международных журналах.

В части A обсуждается нанесение плотных, твёрдых (15-18 ГПа), имеющих высокую оптическую прозрачность (коэффициент преломления 2.07-2.12 и коэффициентов поглощения между $\leq 0.1\times10^{-3}$ и 0.6×10^{-3}, обе величины измерены при длине волны 550 нм) стехиометрических плёнок HfO_2, полученных при плавающем потенциале на кремниевых подложках. Влияние условий осаждения (длительности импульса 50-200 мкс и средненней за время эксперимента плотности мощности на мишень 29-54 Вт/см^2) на скорость осаждения (до 345 и 460 нм/мин для HfO_2 и чистого гафния, соответственно) и на свойства плёнок. Было представлено упрощенное уравнение для описания скорости осаждения плёнок.

Часть B посвящена исследованию микроструктуры плотных, твёрдых (17-18 ГПа), имеющих высокую оптическую прозрачность (коэффициент преломления 2,02-2,11 и коэффициент поглощения между $0{,}1\times10^{-3}$ и 1×10^{-3}; обе величины измерены при длине волны 550 нм), гладких (максимальная средняя шероховатость около 1 нм) плёнок HfO_2, полученных при плавающем потенциале на кремниевых подложках. Было исследовано влияние длительности импульса напряжения (50-200 мкс) и среднней за время эксперимента плотности мощности на мишень (7,3-54 Вт/см^2) на их микроструктуру. Было обнаружено, что все плёнки состоят из прослойки, образующейся на поверхности подложки, за которой следует слой с нано-столбчатой структурой. В одной плёнке была обнаружена высокотемпературая орторомбической фаза HfO_2.

В части C исследована зависимость смачиваемости и свободной поверхностной энергии плёнок HfO_2 от их толщины. В диапазоне 50-250 нм наблюдалась самая сильная зависимость (увеличение краевого угла смачивания до 120°) в связи с преобладанием электростатической составляющей свободной поверхностной

энергии. В то же время, свободная поверхностная энергия возрастает от примерно 25 мДж/м^2 для толщины 50 нм до приблизительно 33 мДж/м^2 для толщины 2300 нм. Было предложено два объяснения наблюдаемой зависимости смачиваемости от толщины плёнки: влияние дополнительной текстуры и / или немонотонная зависимость поверхностной энергии частиц от их размера.

В части D показаны соотношения между химическим составом, фазовой структурой и оптическими, электрическими, механическими и гидрофобными свойствами плёнок Hf-O-N. Плёнки были получены при концентрации азота в усредненом потоке реактивного газа 0, 0,9, 2,6, 5, 25, 50 и 100 %. Плавно регулируемый состав был показан на примере плавно контролируемых свойств материала при переходе от оксида к нитриду, например, изменение коэффициента поглощения при 550 нм от 5×10^{-4} до 1,77, электрического сопротивления от $>10^8$ Ом до $3,2\times10^{-6}$ Ом, твердости от 18 ГПа до 25 ГПа или краевого угла смачивания от 101° до 107°.

В части E обсуждаются основные принципы простой (без использования напряжения смещения подложки во время реактивного распыления и при отсутствии внешнего нагрева в течение всего процесса) трехступенчатой HiPIMS техники (предварительная обработка подложек, осаждение градиентной прослойки ZrO_x и осаждение стехиометрических плёнок ZrO_2) для быстрого осаждениея плотных стехиометрических плёнок ZrO_2 с повышенной адгезией к стальной поверхности.

Глава IV посвящена выводам диссертации. В главе V приведены дальнейшие публикации кандидата.